MICRO-SYSTEM BASED MULTIMODALITY BIOMEDICL IMAGING AND SENSING SYSTEM

By

Bo Li

A DISSERTATION

Submitted to
Michigan State University
in partial fulfillment of the requirements
for the degree of

Electrical Engineering - Doctor of Philosophy

2022

ABSTRACT

Micro-system-based multimodality biomedical imaging and sensing system has been studied by many researchers in the recent decades. Compared to the traditional biomedical system, by using the nano and micro fabrication devices the system size can be dramatically reduced which can be easily used for insertable, implantable and endomicroscope systems. With the emergence of the metalens and microoptoelectromechanical system (MOEMS), the current biomedical and sensing systems can be integrated into a compact size for disease early detection, image-guided surgery and therapy treatment. In this dissertation, we first demonstrate the technique of metalens and metalens based imaging system for *ex vivo* and *in vivo* tissue study. And for the second, we demonstrate the MOEMS based miniaturized NIR handheld probe and micro-ring sensor based handheld photoacoustic microscope probe.

Metasurfaces have been studied and widely applied to optical systems. A metasurface-based flat lens (metalens) holds promise in wave-front engineering for multiple applications. The metalens has become a breakthrough technology for miniaturized optical system development, due to its outstanding characteristics, such as ultrathinness and cost-effectiveness. Compared to conventional macro- or meso-scale optics manufacturing methods, the micro-machining process for metalens is relatively straightforward and more suitable for mass production. Due to their remarkable abilities and superior optical performance, metalens in refractive or diffractive mode could potentially replace traditional optics.

To use the advantages of the metalens, our work aims to develop a metalens based light-sheet fluorescence microscope (MLSFM) for *ex vivo* and *in vivo* biomedical imaging applications with high resolution, fast scanning speed and volumetric 3D imaging reconstruction. Chapter 1 introduces and research background and motivation of this study. In Chapter 2, it shows the design

and principle of the metalens technology. Software metalens structure simulation, nano-fabrication process and device characterization. In Chapter 3, it demonstrates the metalens based light-sheet fluorescence microscope system introduction, design, biomedical tissue imaging protocol and *ex vivo* and *in vivo* imaging result. In Chapter 4, it shows two different imaging system designed for NIR wavelength. And compared the difference between the visible and NIR wavelength imaging effects In Chapter 5, introduces MOEMS based miniaturized NIR confocal handheld system which includes the MEMS device characterization, miniaturized system assembly and phantom imaging. In Chapter 6, the MOEMS and micro-ring sensor based miniaturized optical-resolution photoacoustic microscope system. In Chapter 7, presents a novel line focused metalens based photoacoustic microscope system. In the last chapter, the future work and the ideal for integrated metalens based miniaturized imaging and sensing applications for biomedical study.

ACKNOWLEDGEMENTS

For this dissertation, I would like to thank all collaborators for their selfless supporting, without their great supports it would be impossible to accomplish my PhD research study.

For the first and foremost, I would like to acknowledge my advisor Dr. Zhen Qiu for his great support and guidance during my doctoral study. His ideal and knowledge inspired me during the 4 years study. Without his guidance, I would not sharpen my skill and fulfill my professional knowledge background. For me, he is both a respectful advisor and a good friend, his patience and kindness guide me through my journey at Michigan State University. I believe after many years; I will be still encouraged by his words not only in scientific studies but also for my future career.

Secondly, I would like to acknowledge my guidance committee members, Dr. Tim Hogan, Dr. Wen Li and Dr. Ming Han for their advice. They provide my countless suggestions and feedback for my PhD projects. Without that valuable guidance, I would never improve my system designs.

Additionally, I would also like to thank our senior researchers, Dr. Michael Mandella and Frank Schonig, who trained me for optics system and mechanical system design. By having them on my side, I grow myself from a blank paper to a professional engineer.

Moreover, I would like to give my sincere gratitude to my colleagues in the group, Cheng-You Yao, Aniwat Juhong and Yifan Liu. We have spent days and nights in the lab to discuss and learn together. We have been worked through the most difficult time of the pandemic and support each other to overcome any difficulties during the study. Meanwhile, I like to thank all the graduate students and postdoctoral: Dr. Haogang Cai, Dr. Lin Huang, Dr. Wen Qi, Dr. Weiyang Yang, Dr. Kunli Liu, Yan Gong, Xiang Liu, Chia-Wei Yang, A.K.M. Atique Ullah for their collaborations.

Also, I would like to appreciate Dr. Hirosh Toshiyoshi, Dr. Wibool Piyattanametha, Dr. Aaron Miller, and Dr. Tim Rambo for providing me the guidance and advanced devices.

Last but not least, I would like to thank my family for their unconditional support during my study. The great encouragement helped me to overcome all the difficulties during my doctoral study.

TABLE OF CONTENTS

LIST OF ABBREVIATIONS	vii
CHAPTER 1: INTRODUCTION	1
CHAPTER 2: METALENS PRINPICLE AND DESIGN	5
CHAPTER 3: METALENS LIGHT-SHEET FLUORESCENCE MICROSCOPE	25
CHAPTER 4: NIR II WAVELENGTH FLUORESCENCE IMAGING SYSTEM	48
CHAPTER 5: MOEMS BASED NIR CONFOCAL MICROSCOPE	66
CHAPTER 6: MOEMS AND MIRCO-RING BASED ORPAM	82
CHAPTER 7: METALENS BASED ORPAM	95
CHAPTER 8: FUTURE WORK	100
BIBLIOGRAPHY	107

LIST OF ABBREVIATIONS

QD Quantum Dots

NIR Near Infrared

NIR II NIR Infrared Second Window

FDA Food and Drug Administration

ICG Indocyanine Green

InGaAs Indium Gallium Arsenide

MFD Mode Field Diameter

NA Numerical Aperture

WD Working Distance

SLM Spatial Light Modulator

FOV Field of View

CCD Charge-Coupled Device

MBBs Metasurface Building Blocks

LSFM Light-sheet Fluorescence Microscopy

FDTD Finite-difference Time Domain

H&E Hematoxylin and Eosin

MEMS Micro-Electro-Mechanical Systems

TiO₂ Titanium Dioxide

SiO₂ Silicon Dioxide

EBL E-beam Lithography

CVD Chemical Vapor Deposition

PLD Pulsed Laser Deposition

RIE Reactive Ion Etching

DRIE Deep Reactive Ion Etching

PMT Photomultiplier Tube

MRRs Mirco-rings

DAQ Data Acquisition

FPS Frames per Second

TTL Transistor-Transistor Logic

CMOS Complementary Metal-Oxide Semiconductor

PZT Lead-Zirconate-Titanate Oxide (PbZrTiO3)

SNSPD Superconducting Nanowire Single-Photon Detector

QE Quantum Efficiency

FPGA Field-Programmable Gate Array

SMF Single-Mode fiber

MMF Multi-Mode Fiber

FS Femtosecond Laser

EDF Erbium Doped Fiber

CHAPTER 1: INTRODUCTION

1.1 Research Background

Miniaturized optical systems, for both imaging and sensing, have recently become very attractive for many biomedical applications, such as wearable and endoscopic medical devices. Novel optical lenses with ultrathin structure and light weight have played an important role in the miniaturization of state-of-the-art bio-optical systems. Traditional planar optical lenses (such as micro-gratings and Fresnel micro-lenses) and thin-film micro-optics have been studied in the last few decades. Although the device's footprint has been slightly reduced by using these lenses, conventional lenses have already been shown to have many disadvantages, including limited optical quality for imaging, integration difficulties, and high cost. Metasurface-based flat optical lenses (so-called metalenses) [1-7] show great potential and could overcome most of the challenges. The meta building blocks (MBBs) work as subwavelength-spaced scatterers. Many basic properties of light [8-10](such as phase, polarization, and focal points) can be controlled in highresolution imaging and sensing, through tuning the MBBs' shapes, size, and positions. Conventional lenses, such as refractive lenses (objectives and telescope), are usually bulky and expensive, although they are still dominant in optical systems. Unfortunately, their fabrication processes (such as molding, polishing, and diamond-turning) are commonly sophisticated. In addition, the phase profiles are quite limited, while the structure of the lenses is small. On the contrary, metalens overcome those limitations and provide great advantages compared to traditional optical elements. Especially by using accurate numerical methods, the phase profiles of metalens can be well designed with MBBs. With advanced micro-machining processes, metalens can be mass-produced with high yield. In this dissertation, we mainly focused on two designed metalens with different diameter for different biomedical imaging system. To design and simulate

the metalens, we are using the conventional lenses as our reference benchmark. Ideally the performance the designed metalens should have a similar result with a smaller mechanical size.

1.2 Outline of Dissertation

As demonstrated in the last section, the advantages of the metalens have overcome a lot of challenges during the optics design. In this dissertation, I will break down all metalens related applications into small parts and introduce the key point in optics design and imaging system assembling.

Chapter 2 presents a novel metalens optical simulation and nano-fabrication method. Compare to other groups works, we are focusing on the dielectric meta material TiO_2 as our meta building blocks (MBBs) to manipulate the light path and phase shift. Also in this chapter, we introduce all fabrication detail for the clean room metalens design. After the devices have been fabricated, we run several experiments to characterize the designed device. The testing result shows a great performance compared to the theoretical calculations.

Chapter 3 demonstrates a metalens based light-sheet microscope system. The light-sheet fluorescence microscope (LSFM) has been widely applied on biomedical tissue study. Not only the LSFM provide a high-resolution images and fast scanning but also generate the 3D reconstructed images. In this chapter, we introduce our fabricated metalens into a customized light-sheet fluorescence microscope for *in vivo* and *ex vivo* tissue study.

Chapter 4 compares fluorescence imaging results by using different wavelengths excitation. It has been widely discussed that for optical bio-tissue imaging, the light penetration and scattering effects are mostly limited the imaging resolution. In this chapter, it shows several imaging systems with different laser excitation wavelengths to study the depth of tissue imaging for both *in vivo* and *ex vivo*.

Chapter 5 shows the MOEMS based miniaturized NIR confocal microscope handheld system. The designed system is integrated with the thin-file PTZ MEMS scanner to achieve 2D scanning for NIR wavelength imaging. Due to the unique scanning pattern, Lissajous Scanning, it can achieve real time fast imaging for both *ex vivo* and *in vivo* tissue study. Compares to the traditional confocal fluorescence microscope, the designed system has dramatically reduced the size but also provided high resolution images.

Chapter 6 discuss the MOEMS and micro-ring based miniaturized OR-PAM handheld system for biomedical imaging and sensing. Unlike the traditional OR-PAM system, we replace the bulky transducer with a mm size micro-rings (MRRs) optical sensor for ultrasound signal detection. Firstly, due to the properties of the nano structure inside the sensor, the Q factor which is the sensitivity of the sensor is largely increased for low ultrasound signal detection. Secondly, the physical properties of the MRRs allow a high transmission for optical light which also call transparent ultrasound sensor. This great advantage allows us to reduce the mechanical size of the system and provide high resolution photoacoustic images.

Chapter 7 we demonstrate a metalens based OR-PAM system. To our acknowledgement this is the first metalens based OR-PAM system. In this chapter, we first prove the basic principle of the optical design. And then we tested the system performance by using different phantom targets. At the end, we achieve the photoacoustic imaging by using the line-focused metalens.

Chapter 8 we discuss the future work for more miniaturized imaging and sensing system for biomedical applications. In here, we purpose the idea of metalens integrated dual axis confocal handheld probe and metalens based MRRs OR-PAM handheld probe.

1.3 Motivation and Research Contribution

In this work, multimodality biomedical imaging has become a popular topic for many

researchers in recent decades. Like confocal microscope, light-sheet microscope and photoacoustic microscope not only provide the high-resolution optical resolution for disease early detection and imaging-guide surgery but also allow the people to have the non-invasive diagnosis method to access the biomedical tissues. To improve the instrument performances and easily handle for clinical treatment. The miniaturized handheld systems are urgently needed to be developed for both fluorescence imaging and sensing. To achieve this goal, we designed several optical imaging and sensing systems to fulfill the needs in this field.

CHAPTER 2: METALENS PRINPICLE AND DESIGN

2.1 Metalens Based Miniaturized Optical System

2.1.1 Metalens Review and Background

Miniaturized optical systems, for both imaging and sensing, have recently become very attractive for many biomedical applications, such as wearable and endoscopic medical devices. Novel optical lenses with ultrathin form factor and light weight have played important role in the miniaturization of the state-of-the-art bio-optical system. Traditional planar optical lenses (such as micro-gratings, Fresnel micro-lenses) and thin-film micro-optics have been studied for the last decades. Although the device's footprint has been slightly reduced using these lenses, the conventional lenses have already shown many disadvantages, including limited optical quality for imaging, integration difficulties, expensive cost. Metasurface-based flat optical lenses (so-called metalens) [4, 7, 11-15] show great potentials and could overcome most of the challenges. The meta building blocks (MBBs) work as a subwavelength-spaced scatterers. Many basic properties of light [16-18] (such as phase, polarization, focal points) can be controlled aimed for high resolution imaging and sensing, through tuning the MBBs' shapes, size and positions. Conventional lenses, such as refractive lenses (objectives and telescope), are usually bulky, large size and expensive, although they are still dominant in optical system. Unfortunately, their fabrication processes (such as molding, polishing, diamond-turning) are commonly sophisticated. In addition, the phase profiles are quite limited while the form factor of the lenses become small. On the contrary, metalens overcomes those limitations and provides great advantages, compared to traditional optical elements. Especially, by using the accurate numerical methods, the phase profiles of metalenses can be well-designed with the MBBs. With advanced micro-machining process, metalenses can be mass-produced with high yielding.

2.1.2 Phase Profile, Plasmonic Metasurface and All Dielectric Metalens

The refractive lenses are widely used in various optical systems, such as telescopes and microscope. Although they have very good properties in phase control and polarization, traditional refractive lenses with high numerical aperture (NA) are often bulky and expensive. Additionally, the complex macro- or meso- scale fabrication process is still relying on the conventional optics manufacturing methods, which have been developed over hundred years. To meet optical requirements, the refractive lenses are usually designed with different shapes. However, metalens provides new opportunities to overcome these limitations. For instance, the phase profile can be modified by changing the MBBs [19]. The required phase profile [2], which achieves diffraction limited focusing for collimated incident light, is expressed as below:

$$\varphi(r) = -\frac{2\pi}{\lambda}(\sqrt{r^2+f^2}-f)$$

Equation 1 Metalens phase equation

Where f: focal length; r: radial position. The designed metasurface should create a phase profile to modulate incident planar wavefront into spherical ones at focal length f from the lenses.

Usually, metasurface-based lenses use MBBs to modify the optical characteristics. One of the most representative techniques is to create the plasmonic effects on the surface. The plasmonic antenna [20] can be easily micro-machined using advanced electron beam lithography (EBL) and relatively simple lift-off process. The concentrated incident light can be transformed into a smaller region which matches its own wavelength and causes oscillations. By having the plasmonic effect on its metasurface, metalens has attracted great interests in the optics field. For example, experimental results reported by Yin *et al* [21] have indicated that the micro-structures generated the plasmonic effect on the Ag film surface and successfully formed focal spot at the focusing

plane. Another study, proposed by Zhang *et al* [22], has shown that the focusing could be achieved and also be tuned using different nano-antenna shapes such as elliptical and circular blocks.

While dielectric phase shifters are utilized in the MBBs, the energy absorption loss of the incident could potentially be reduced significantly. Researchers have taken advantage of this and include dielectric phase shifters in many new optics designs. For example, Vo *et al.* [18] has proposed the polarization independent lenses with the dielectric building blocks (circular silicon arrays). High transmission efficiency (70%) has been achieved with the incident light at wavelength of 850 nm. Faraon group from Caltech [23] has demonstrated that single dielectric nano-antenna could be designed as efficient building block which might provide full phase coverage. Based on optimized nanostructures, the spatial image resolution remains excellent qualities with relatively high transmission efficiency. Capasso group in Harvard University [24] has demonstrated that the dielectric metalens also has superior performance in the spectral application in the visible range. The polarization independent metalens has been micro-fabricated by titanium dioxide (TiO₂) nanopillars. The metalens could achieve relatively high N.A. = 0.85 with efficiency more than 60% for incident wavelength of 532 nm and 660 nm.

2.1.3 Advanced Techniques for Metalens

In the miniaturized optical system, field of view (FOV) is one of the key factors for evaluating the overall qualities of the imaging and sensing system [25]. Unfortunately, due to the technical limits, most metalenses suffer from serious off-axis aberration, leading to a limited FOV. Pursuing increased FOV is a common goal for many scientific studies. For example, in traditional optical lens based imaging system, bulky and expensive objective lenses with aberration-corrected are frequently utilized to achieve a relatively large FOV.

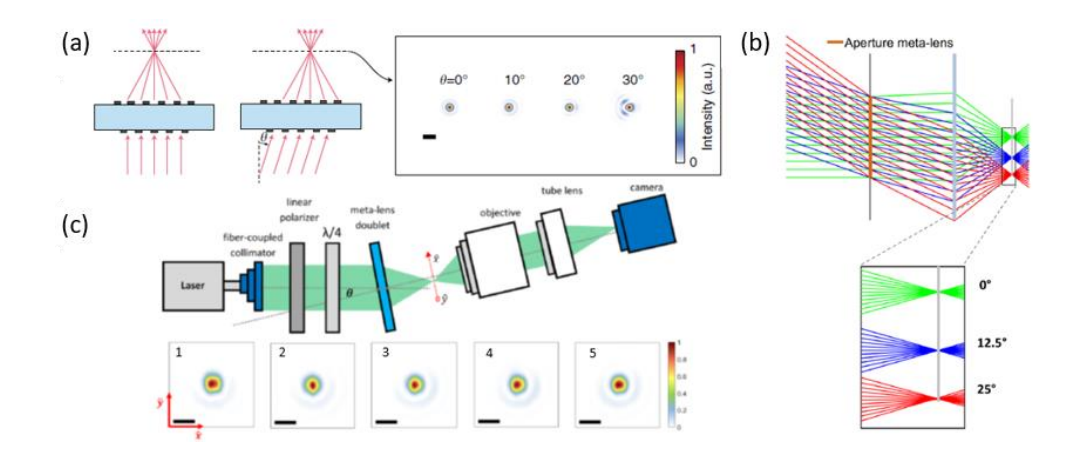
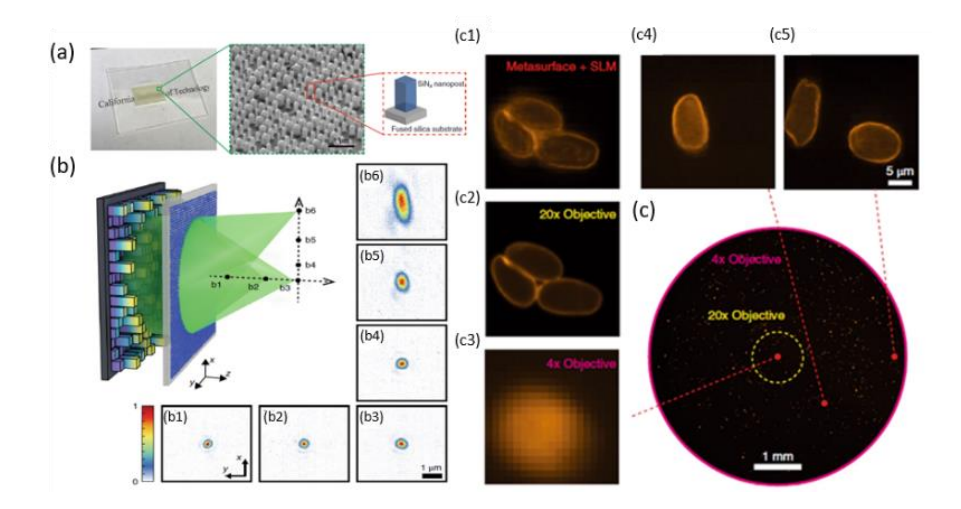


Figure 1 Focal spot characterization for different angles of incidence source. (a) (left) Schematic illustration of focusing of on-axis and off-axis light by a metasurface doublet lens. (right) Simulated focal plane intensity for different incident angles. (Reproduced from [32] with permission). (b) The Ray diagram obtained by adding the aperture meta-lens resulting in diffraction-limited focusing along the focal plane. (c) Focal spot measurement setup. (1-5) Focal spot intensity profile at $(1) 0^{\circ}$, $(2) 6^{\circ}$, $(3) 12^{\circ}$, $(4) 18^{\circ}$, $(5) 25^{\circ}$ incidence angle. (Reproduced from [33] with permission).

Theoretically, the single-layer metasurface-based flat lenses suffer from the off-axis aberration [26, 27], along with wide-angle absorption [28-31] and other problems. To broaden the FOV, multiple-layers metalens structures have been successfully demonstrated. For example, Faraon group [32] has shown a doublet lens formed by cascading two metasurfaces, Figure 1(a), which could achieve the diffraction limited focusing up to \pm 30° with near-infrared (NIR) incident light of 850nm. For a shorter wavelength (532nm) in the visible range, Capasso group [33] reported a metalens doublet design. For the aperture metalens, shown in Figure 1(b), with the positive and negative angle incident light, the spherical aberration can be corrected and all the focusing points can be eventually allocated on the same focal plane. Based on the principle of the Chevalier lens [34], the metalens shown in Figure 1(c) has provided a relatively larger FOV result with incident light angle up to \pm 25°.

Most recently, single-layer metalens with disorder-engineered design [35], Figure 2(a), has been demonstrated by Yang and Faraon's groups in Caltech [35] with improved resolution and

FOV. This disorder-engineered metalens has individual input-output responses which is different from the multiple-lens based system. The new metalens has a high numerical aperture (NA \sim 0.5) focusing to 2.2 x 10⁸ points in an ultra-large FOV with an outer diameter of 8 mm.



<u>Figure 2 Disorder-engineered metasurfaces.</u> (a) Photograph and SEM image of a fabricated disorder-engineered metasurface. (b) Schematic of optical focusing assisted by the disordered metasurface. The incident light is polarized along the x direction (b1-b6). (c) Low-resolution bright-field image captured by a conventional fluorescence microscope with a $4 \times$ objective lens (NA = 0.1). (Reproduced from [35]with permission).

To increase the FOV, another approach has been proposed by Guo *et al.* [36]. The key to construct a metalens with larger FOV is to realize a perfect conversion from the rotational symmetry to translational symmetry in light field [36]. The wavenumber in free space and incident angles should satisfy the following relation, shown in equation 2.

$$k_0 sin\theta_x x + k_0 sin\theta_y y + \emptyset_m(x, y) = \emptyset_m(x + \Delta_x, y + \Delta_y)$$

Equation 2 Metalens incident angle in free space

Where the k_0 is the wavenumber in free space, $\emptyset_m(x,y)$ is the phase shift profile carried by the flat lens, Δ_x and Δ_y correspond to the translational shift of $\emptyset_m(x,y)$ at incidence angles of θ_x and θ_y [36]. To verify this method, a new metalens with diameter of 350 mm and focal length f = 87.5 mm (NA ~ 0.89) was simulated, shown in Figure 3(a). As a proof of concept, the

measurement of far-field power patterns is demonstrated with a circularly polarized horn through the metalens for wide FOV. The result shows that $a \pm 60^{\circ}$ beam steering can be realized by the transversely changing the location of the antenna within an area from -75.8 mm to 75.8 mm.

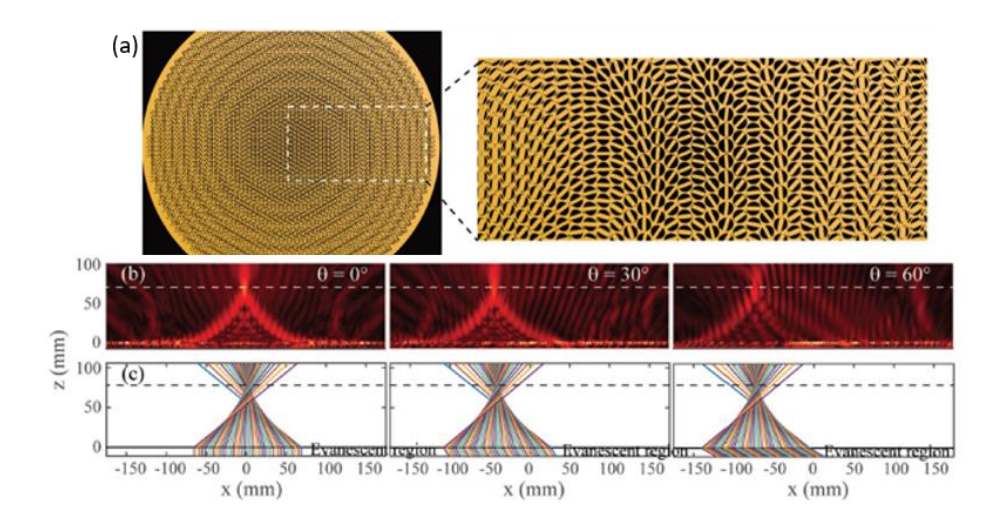


Figure 3 Performance of the wide-angle flat lens. (a) Perspective and zoom view of the wide-angle flat lens. (b) Simulated light intensity distributed on the xoz plane at 19 GHz electric field distributions. (c) Ray trajectories of 19 GHz before and after propagating through the flat lens. Left, middle, and right panels of (b) and (c). respectively, represent the case of for $\emptyset = 0^{\circ}$, 30° , 60° . (Reproduced from [28] with permission).

To achieve broader FOV and preserve high resolution imaging performance, Yang and Faraon's groups [37] have demonstrated a new phase-array based method, Figure 4, without requiring a large scale-up in the number of controllable elements [37]. It uses disorder-engineered design, as the key factor is similar to that of previous work [35].

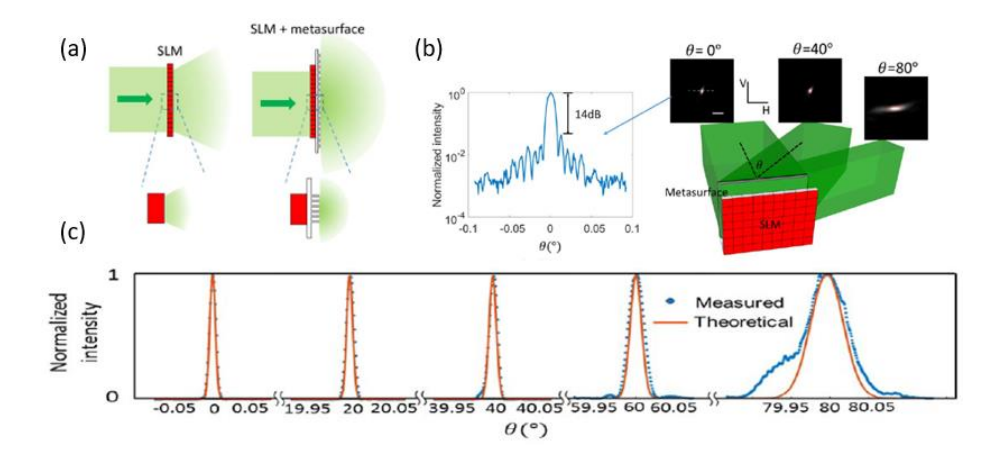


Figure 4 Wide-angular and high-resolution beam steering by a metasurface array. (a) The comparison of steering range of a single SLM structure and a metasurface-coupled SLM structure. (left) without the metasurface, the SLM can provide only a small diffraction envelope. (right) With the metasurface-coupled SLM structure, since each scatterer is subwavelength, the steerable range can span from -90° to +90°. (b) Illustration of the steering scheme (c) 1D far-field beam shapes at other steering angles. Red lines denote the theoretical shapes of the beams. Blue dots denote the measured data. (Reproduced from [29] with permission).

Table 1 Comparison between fabricated metasurface-based lens in wide angular FOV design.

Ref (Year)	Efficiency	Material	NA	Wavelength	FOV
Arbabi et al (2016) [24]	70%	a-Si:H	N/A	850nm	±30°
Groever et al (2017) [25]	N/A	TiO_2	0.44	532nm	±25°
Jang et al (2018) [27]	N/A	SiN_x	>0.5	532nm	8mm
Guo et al (2018) [28]	93%	Simulation	0.89	Far-field power	±60°
Xu et al(2018) [29]	95%	SiN_x	N/A	532nm	±80°

The 2D array subwavelength scatters (SiN_x with height 630 nm) were deposited on the silica substrate arranged in a square lattice with a pitch size of 350 nm. Also, when the designed lens combined with a spatial light modulator (SLM), the output light of the system would have a larger cover angle range than what is possible with a SLM alone. As a result, the disorder-engineered metasurface with SLM was able to scatter light uniformly within the range of \pm 90° [Figure.4(a)] due to the subwavelength size and random distribution of the nanofins.

2.2 Light-sheet Metalens for Visible Wavelength

2.2.1 Huygens Metalens design

More studies of the metal/dielectric-based metalens have been demonstrated in recent years

for amplitude, phase and polarization manipulation [5-9]. To be different from the conventional optical lenses, metalenses rely on the nanostructures to gradually shift the phase during the light propagation to various light shapes. However the light phase can be changed by the metallic metalens through the localized plasmonic resonances, the phase can be only covered from 0 to π [10]. In addition, transmission efficiency is limited by material properties which is due to the Ohmic losses in metal plasmonic metasurface structure[11]. On the other hand, the dielectric metasurface (GaP, SiN, TiO₂) can provide a 2π phase coverage from visible wavelength up to infrared wavelength by using the non-interacting nanoparticles[12-14]. Each of these nanoparticles works as an individual phase shifter which guides the incident light into the designed wavefront at the focal plane[15-18].

Huygens metasurface has been demonstrated with metallic nanostructure[7] at microwave frequency and Si at near-IR wavelength[19-21]. In this paper, we demonstrate a Huygens metasurface-based ultra-thin (thickness<<wavelength) light-sheet metalens using titanium dioxide ($\text{Ti}\,O_2$) as nano-discs (NDs) dielectric material due to its high-refractive index and lower attenuation coefficient in visible range [22-27]. To demonstrate the potential applications of the designed metalens, we customize the light-sheet fluorescence microscopy system for biomedical study which can be used in the development of fluorescent images and cell activity manipulation [28-33]. The concept of light-sheet imaging has been re-introduced in a biomedical research study [28]. The light-sheet fluorescence microscopy (LSFM) is commonly used in clinical diseases diagnoses and prognoses [28, 34-37]. The study of light-sheet microscopy can be tracked back more than a century [38]. The LSFM or selective plane illumination microscopy (SPIM) [29, 39-41] will not only provide high-resolution images in biological in *vivo* study but also generate a rapid volumetric microscopy method which is urgently needed in biomedical studies [28, 30, 42,

43]. For the standard Gaussian beam, the scanning depth of focus and resolution is strictly limited by the law of diffraction. However, the low-numerical aperture (NA) Gaussian illumination may have an impressive scanning depth within a decent thick illumination beam waist (about 7μm for our designed metalens, NA 0.03). Design, numerical simulation, and nanofabrication of the light-sheet metalens.

2.2.2 Fabricated Light-sheet Metalens Concept and Desgin

For designed metalens, the required phase profile $\varphi(r)$ [2], which achieves diffraction-limited focusing for collimated incident light, is expressed as below:

$$\varphi(r) = -\frac{2\pi}{\lambda}(\sqrt{r^2 + f^2} - f)$$

Equation 3 Metalens phase mapping

Where λ is the wavelength of the incident light in free space, f is the focal length and r is the radial position. By having the goal to design a planar Huygens-based light-sheet metalens, we first studied both transmission and phase shift properties of the dielectric material TiO_2 . To achieve a high-efficiency transmission metalens in the visible spectrum is challenging because for most the dielectric materials for example silicon has better application in the near-infrared wavelength than visible. Here, we select TiO_2 as our nano-resonator material due to its higher refractive index (1.4) and lower attenuation coefficient in visible (providing maximal transmission amplitude).

Similar to the traditional lenses, passing the light through a certain volumetric propagation is used to achieve the phase shift. In the metalens design, however, the required phase shift is commonly accomplished via waveguiding effects [44] and effective medium designs by the nanoresonator [45]. The key factor in metalens design is the optimization of the nanoresonator's geometric parameters such as radius, thickness and the gap distance between them which will

achieve the 0 to 2π phase coverage and stay in higher transmission efficiency.

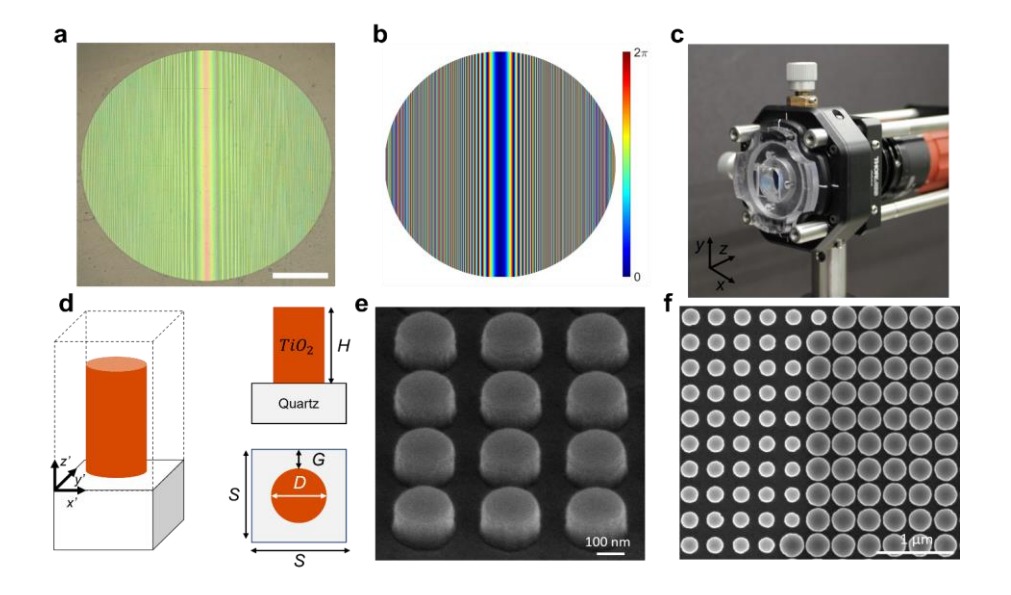


Figure 5 Light-sheet metalens design and fabrication. **a**, A commercial microscope image of the 6mm metalens. Scale bar: 2mm. **b**, The phase map for the designed light-sheet metalens. **c**, Photographic image of metalens mounted on an optical cage system. **d**, Schematic of an individual metalens building block consisting of a TiO_2 nanopillar on a quartz substrate. The nanopillars have height H = 155nm and arranged on the unit square substrate with size (S). Phase imparted by single nanopillar is manipulated by its diameter (D) and the gap distance between the nanopillar edge and the unit substrate (G). **e** and **f**, Scanning electron micrograph images of the fabricated metalens from 45-degree angle and top view.

A commercial microscope (VHX Digital Microscope, Keyence, Osaka, Japan) image of the designed light-sheet metalens is depicted in Figure.5. The total diameter of the designed lens is 6 mm and the focal distance is about 100 mm. Figure.1b shows a photographic image of the fabricated light-sheet metalens mounted on the Thorlabs optical cage system. The fabricated TiO_2 nano-resonators were deposited in the center of a 1x1 cm² quartz substrate. A custom-built 3D printed VeroClear holder was used to hold the metalens and assembled with the 30mm cage XY translator (CXY1, Thorlabs, NJ, USA) for imaging. The translator can slightly adjust the metalens position to make sure the metalens is co-axis with the collimated beam.

The metalens building blocks, a TiO_2 nano-resonator, have a height of 155nm and varying

diameters with varying gap distances between each other to locally impart the required phase shift. The schematic of TiO_2 nano-resonators is shown in Figure 5 (d). Due to its high refractive index and low absorption in visible light region, TiO_2 is an ideal material candidate for nano-resonator to design high-efficiency metalens in this wavelength. The overall power transmittance of the designed metalens is above 76% and the total phase shift achieves $0\sim2\pi$ coverage. Figure 5 (e) and 5 (f) show the scanning electron microscope images of a metalens using the traditional top-down approach [46]

2.2.3 Metalens MBBs Simulation and Nano-fabrication Process

By using the basic metalens equation the phase shift map of the designed lens can be easily calculated. In this dissertation, we designed 2 different size metalens with different focal distance, 33.3mm and 100mm. The MBBs worked as a discrete phase shift which directly changing the phase profile at different location on the metalens surface. At the beginning, we designed metalens phase shift map shown in Figure 6 with different focal distance.

After we calculated the phase shift map of metalens, multiple MBBs nanostructure need to be simulated to satisfy the phase map. During MBBs simulation shown in Figure 7, two different sweeping simulations were applied, one is the MBBs diameter D, and the other one is the gap between the MBBs and substrate edge. The sweep range for diameter is from 110nm to 160nm with step size 1nm. The sweep range of the gap is from 20nm to 120nm with step size 20nm.

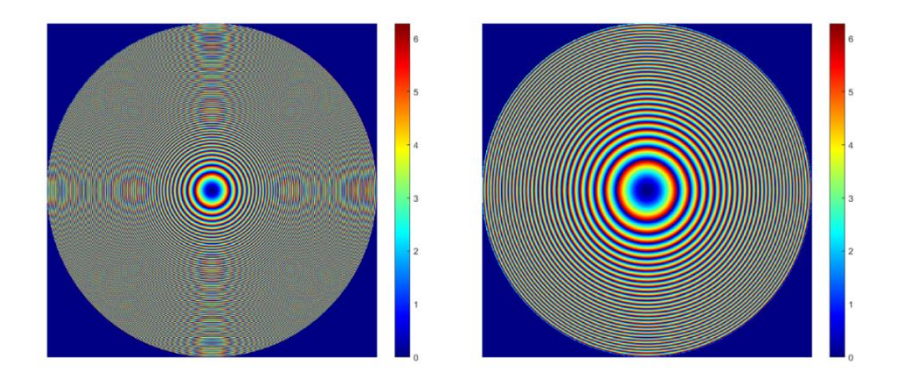


Figure 6 The phase shift map for 2 different metalens design with different focal distance.

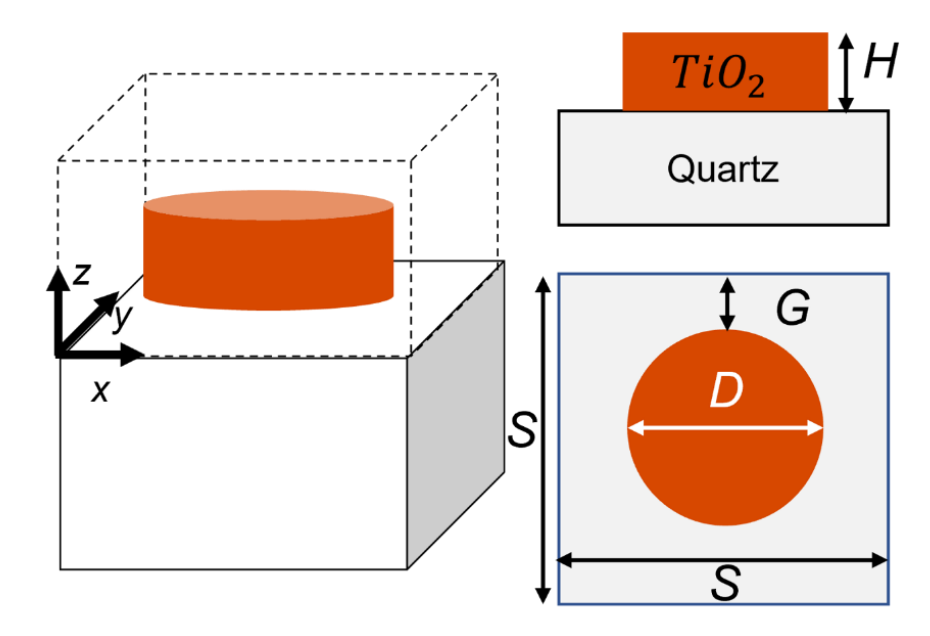


Figure 7 Unit cell MBBs schematic.

After given the certain incident laser wavelength, substrate material and TiO_2 height H, we used Finite Difference Time Domain (FDTD) shown in Figure 8 to calculate single MBBs phase shift.

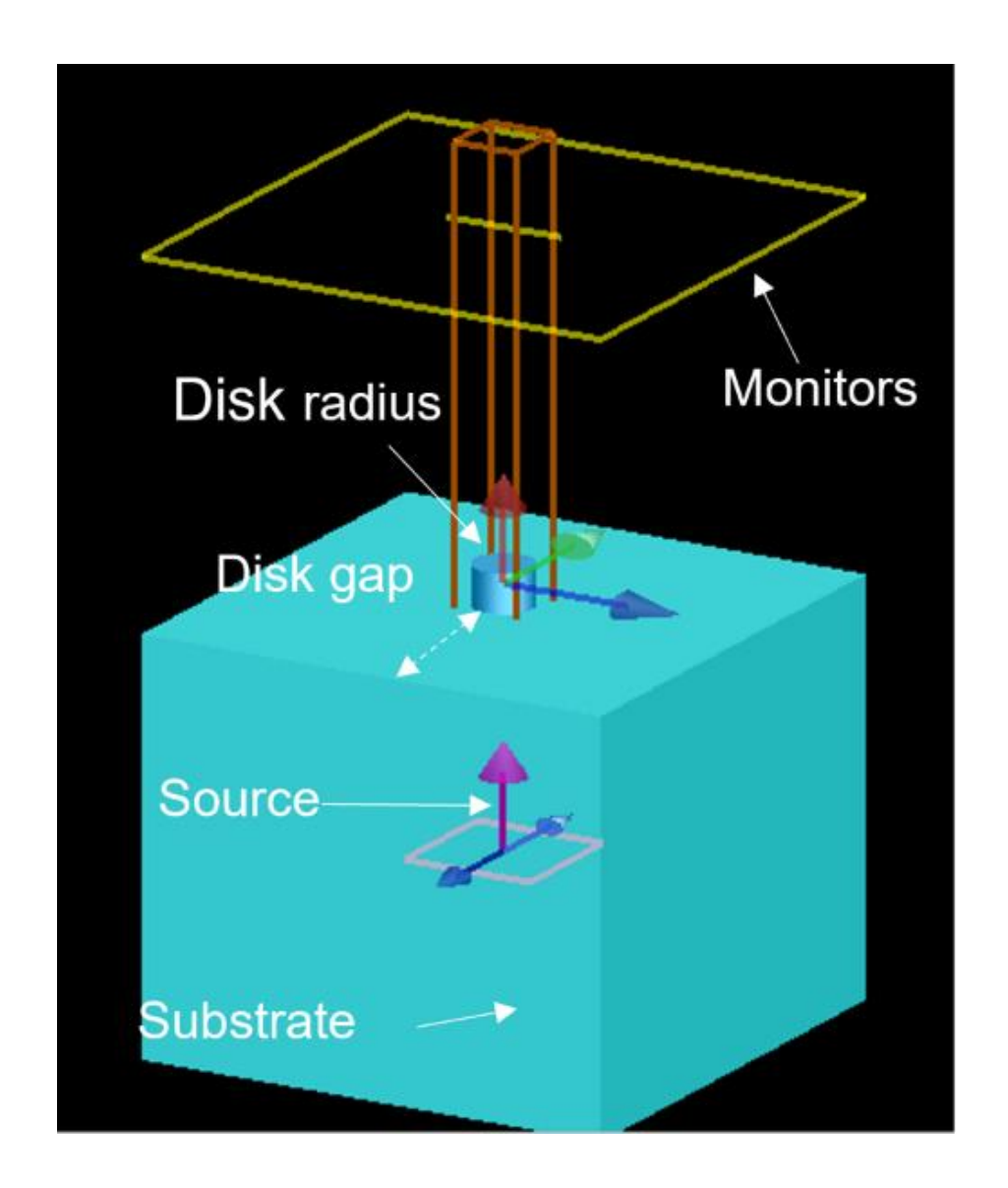


Figure 8 FDTD simulation modeling window.

The FDTD simulation result is shown in Figure 9, on the left is the MBBs efficiency, on the right is the phase shift of each MBBs. The white dash line in Figure shows that phase coverage of the total shift is from $0\sim2\pi$ and also the efficiency remains high.

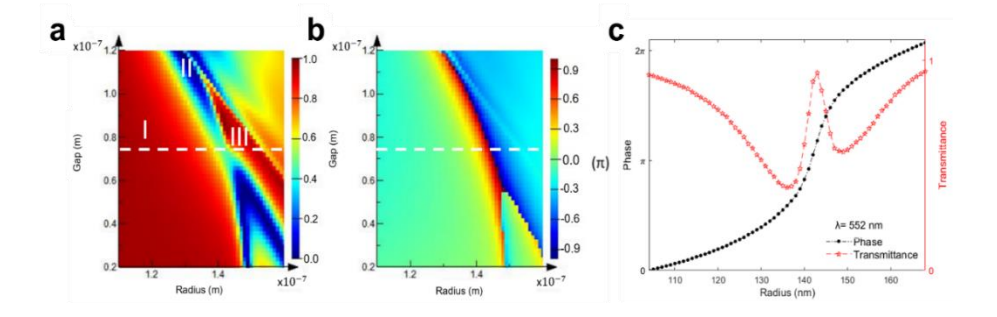


Figure 9 Light sheet metalens FDTD simulation result. (a) Simulated transmission at λ =552nm as a function of the disc radius and gap. (b) Simulated phase at λ =552nm based on the radius-gap plane. (c) A phase plot vs. nano-discs radius by FDTD simulation. When overlaid the transmission and phase simulation result, a set of metasurface nano-discs radius parameters can be found that will achieve a full 2π phase coverage with high transmission.

For the metalens nano-fabrication process, first, a25mmx75mm quartz slide with thickness 1mm substrate was apply in acetone wash and RIE (Ar+ O_2) cleaning. After that, a 155nm TiO_2 was coated on the substrate by atomic layer deposition (ALD) at 150°C and then processed thermal annealing at 475°C for 30 mins. Next, the EBL photoresist PMMA(495-A3) and copolymer(950-A2) were spined on the top of the TiO_2 layer. The double photoresist structure will create the undercut structure during develop and easy for lift off. The EBL processing time was depended on the metalens diameter, for our experiment, the 6 mm diameter metalens takes 72hrs. After the EBL and develop, the Cr was deposited on the substrate to create the hard mask. By leaving the substrate inside the remover 1165 at 75°C for lift-off. After the lift-off, a reactive ion etching (RIE) was applied to etched off the TiO_2 . After the desired pattern left on the substrate, the Cr hard mask was removed by wet etching (DI water+ H_2SO_4). The final fabricated device was washed by DI water and N_2 blow dry.

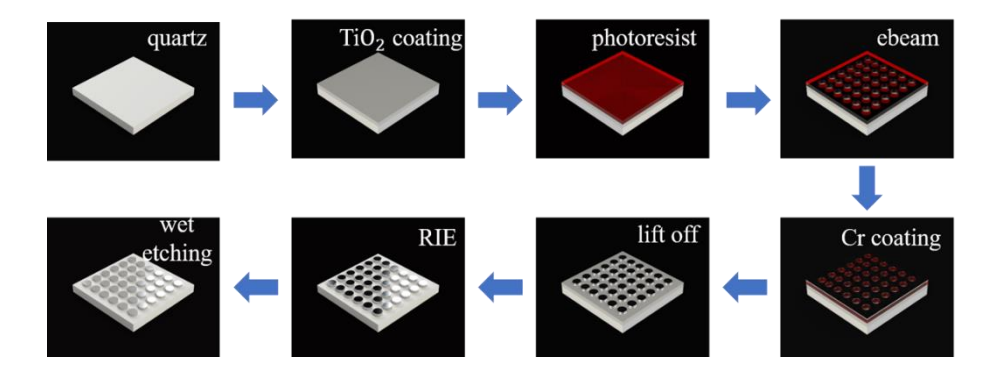


Figure 10 Metalens nano-fabrication process workflow.

2.2.4 Experimental Metalens Optical Characterization Result

Before the fabrication, we calculated the theoretical optical properties of the designed lightsheet metalens. To increase the depth of focus or the field of view, the numerical aperture (NA) was selected as a low value ~ 0.03 . By using equation (4), we first calculated the ideal beam waist which is the thinnest point at the focal length ω_0 of the designed lenses.

$$\omega_0 = \frac{\lambda}{\pi NA}$$

Equation 4 Beam waist calculation

Where the λ is the excitation wavelength and the NA is the numerical aperture of the designed metalens. Another important factor is the depth of focus (known as the confocal parameter), C_p , was calculated by the following equation (5):

$$C_p = 2Z_r = \frac{2\pi w_0^2}{\lambda}$$

Equation 5 Confocal parameter calcuation

Where the Z_r is the Rayleigh length and λ is the excitation wavelength. The designed light-sheet metalens will have a 5.86 μ m beam waist and a depth of focus of 390 μ m.

To characterize the light-sheet metalens, we use a custom-built optical setup (Figure 11). The beam waist and focal distance for different visible wavelength was measured by using the Beam Profile scanner (BeamScan, Photon Inc, CA, USA). We measured the two-dimensional intensity profile of the output beam at three different wavelengths(532nm, 552nm, and 561nm) which are widely used in light-sheet microscopy system light sources.

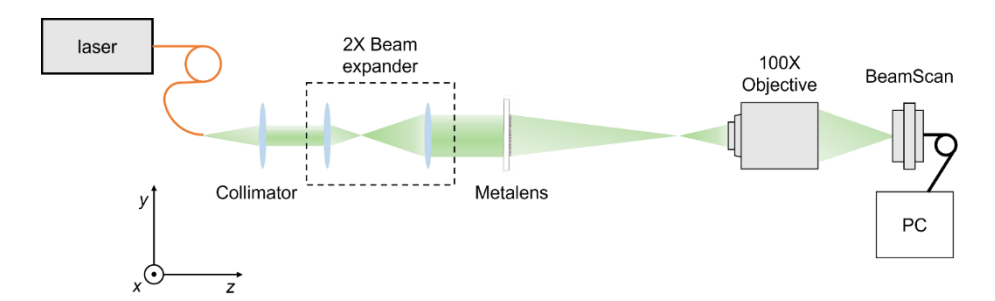


Figure 11 Measurement setup for output beam profile characterization. The metalens based light-sheet is pumped by an OBIS multi-wavelength laser engine (532nm, 552nm and 561nm) at individual wavelengths in the range of interest. At the collection side, the combination of a 100x objective and beam scanner is used to collect the output beam profile and mapping the light intensity distribution images at different wavelength.

Figure 12 (a) shows the light-sheet metalens beam profiles in *yz*-plane, a collimated beam travels along the *x*-axis and passes through the metalens center. A Beam Profile scanner was placed after the metalens to detect the output beam. As expected, the focused beam was captured around the designed position with the focal point shifted axially with changing wavelength. The focused beam spot of the light-sheet metalens in the lateral plane (*xy*- plane) shown in Figure 12 (b) had almost symmetric profiles with 27.01, 12.85 and 13.46 μm full-widths at half-maximum (FWHM) at 532, 552, and 561nm wavelength. The measured beam size is nearly close to the ideal lens design.

Figure 2 (c) compare the output beam profile between a commercial cylindrical lens (LJ1567RM-A, Thorlabs, NJ, USA) and the designed metalens. At the designed wavelength, the beam waist of the designed metalens shows an excellent result compared to the traditional cylindrical lens. As evident in Figure 12 (b) the metalens focal spot profile has a similar FWHM to the conventional cylindrical lens. However, it is difficult to measure the focal plane location for

a low NA optical lens; we selected the focal plane at the maximum intensity during the experiment. As a result, the output beam of the light-sheet metalens would have competed with the traditional cylindrical lens with the same NA.

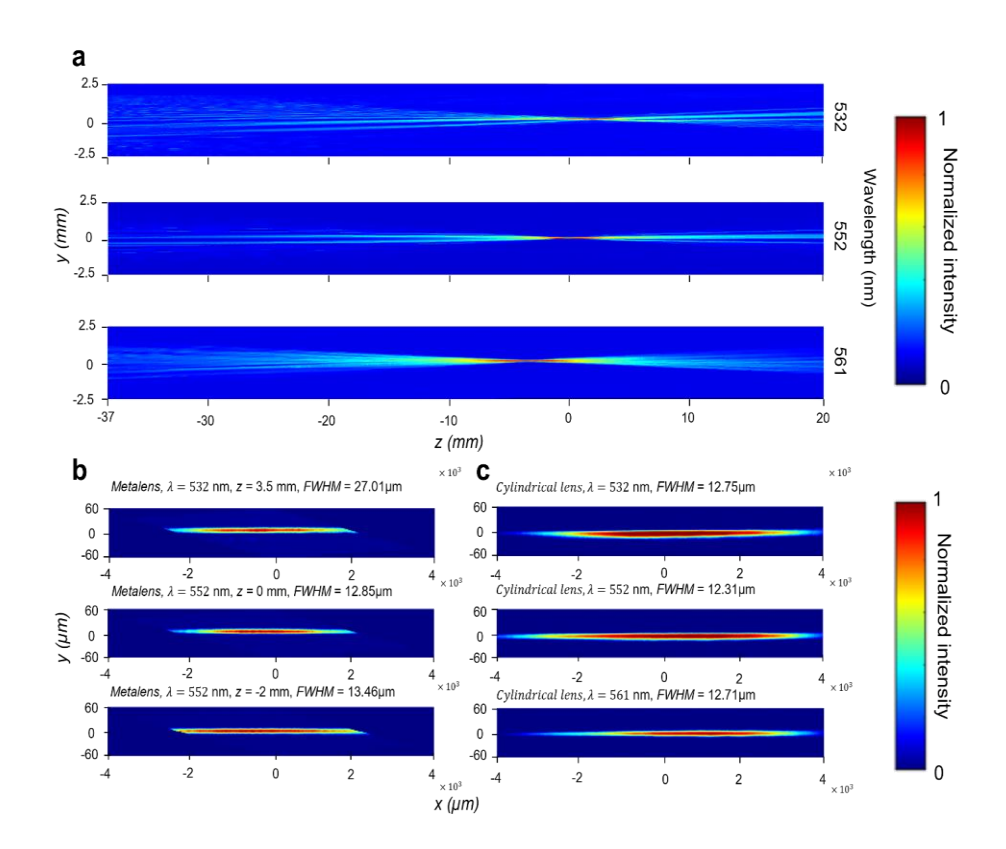


Figure 12 Optical characterization of the light-sheet metalens. a, Measured intensity distribution of the output beam of the metalens alone the propagation direction in the yz-plane at $\lambda = 532$, 552 and 561nm. b, Focal spot profiles of the metalens at corresponding wavelength. c, Focal spot profiles of the cylindrical lens at corresponding wavelength. The focused beam profile with metalens shows a great result compared to the traditional cylindrical lens.

To compare the focusing effects between the nano-fabricated metalens to a traditional cylindrical lens at different wavelength, a Gaussian beam profile result is plotted by MATLAB and shown in Figure 13

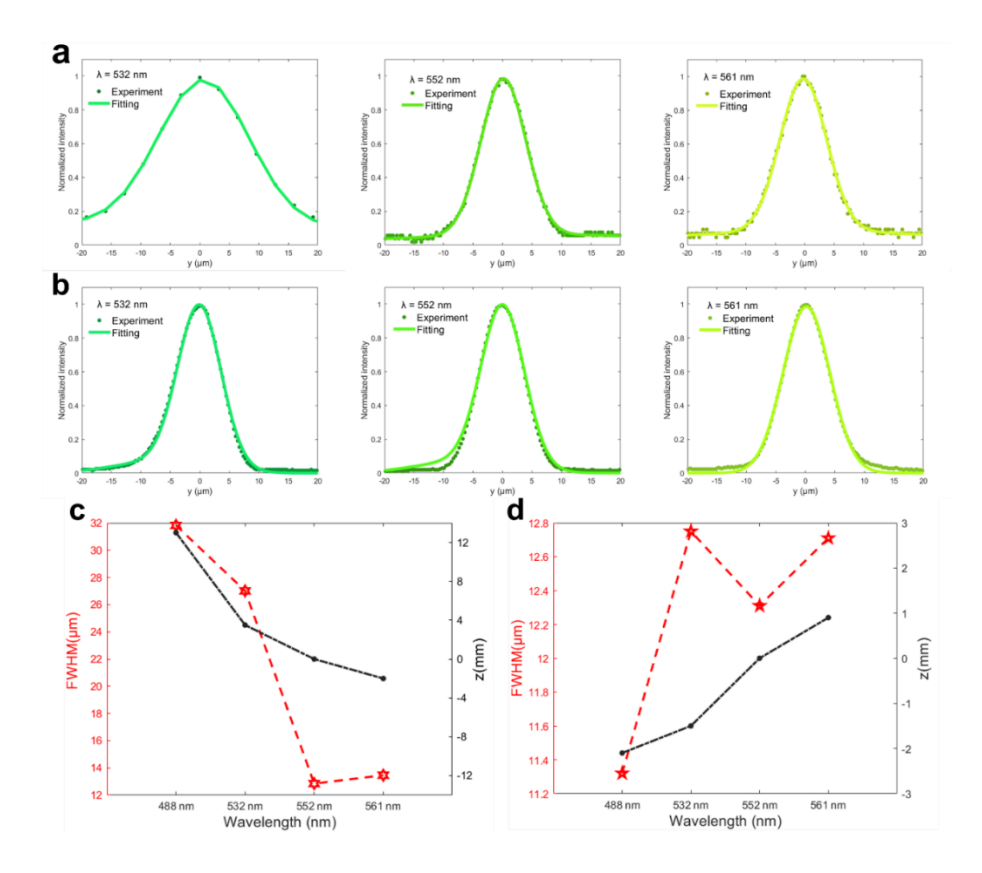


Figure 13 Light-sheet beam waist characterization at different wavelength. a, Metalens based light-sheet beam waist at focal plane on different wavelength from 532 to 561nm. b, Cylindrical lens generated light-sheet beam waist at focal plane on different wavelength from 532 to 561nm. c, FWHM and focal distance plot for metalens based light-sheet at different wavelength. d, FWHM and focal distance plot for cylindrical lens generated light-sheet at different wavelength.

After the beam profile characterization, the focusing effects of the designed metalens was also record by a customized system. By moving the metalens along the objective lens focusing direction (z direction) a series images were captured and projected into the other xy plane shown in Figure 14. By measuring the distance between metalens surface and the objective lens focal point, the thinnest light-sheet was captured at 102.6mm which satisfies the theoretical calculation and design.

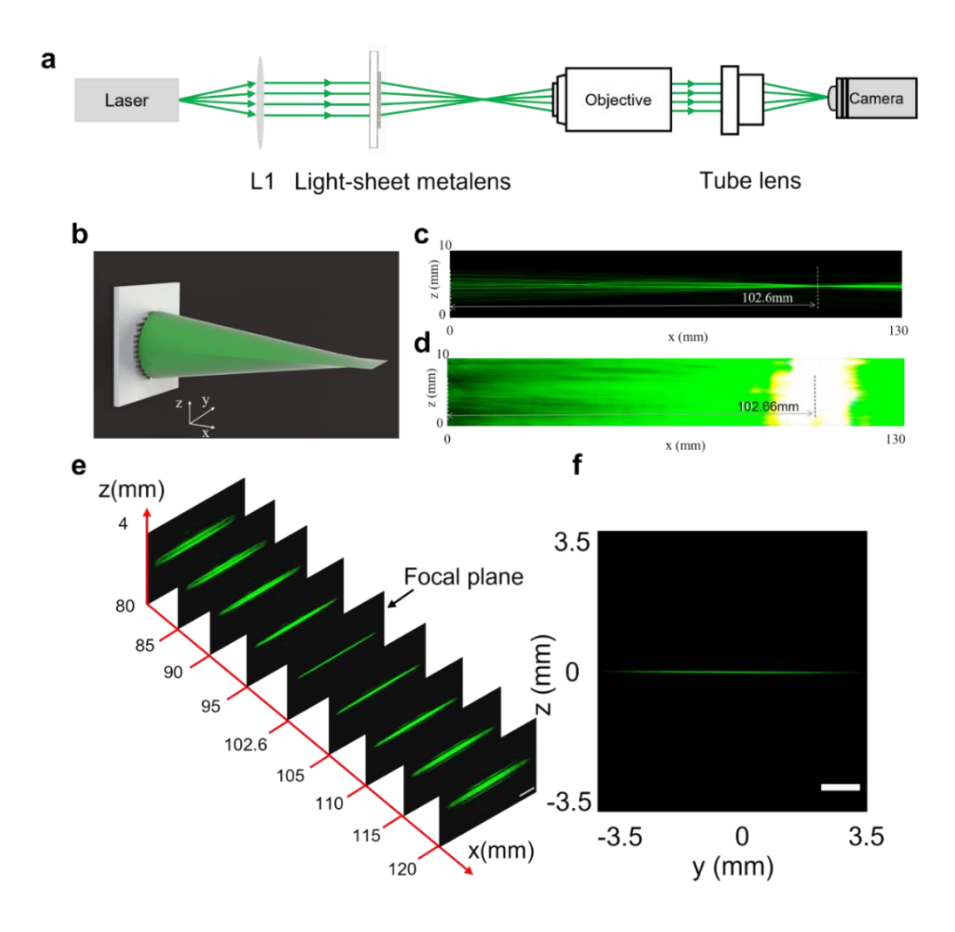


Figure 14 Light sheet metalens focusing characterization under λ =552nm coherent CW laser. **a**, The schematic of the custom-built optical system. **b**, The 3D model of light-sheet illumination produced by the metalens. **c**, The focal distribution for the metalens light-sheet at 552nm wavelength in xz plane. **d**, The focal distribution for the metalens light-sheet at 552nm wavelength in xy plane. **e**, Multiple frames of metalens light-sheet focal distribution in yz plane. **f**, At focal distance, the light distribution in yz plane, the laser beam is well focused by the metalens. Scale bar: 1mm.

2.2.5 Conclusion of Nano-Fabricated Light-sheet Metalens

In this chapter we demonstrate the designed light-sheet metalens. By comparing the theoretical calculation and the experimental optical result we successfully design and develop the metalens for biomedical imaging. Additionally, we also compare the metalens performance to a traditional cylindrical lens at same experimental condition, it also shows a good result which indicates the designed metalens should be able to handling the real optical imaging requirements.

In the next chapter, we will introduce the metalens based light-sheet fluorescence microscope

system for biomedical tissue imaging.

CHAPTER 3: METALENS LIGHT-SHEET FLUORESCENCE MICROSCOPE

3.1 System Introduction

Light sheet microscopy (LSM) has been widely studied by people in biomedical field for the last decades. The excellent optical imaging property which is the selective plane illumination microscopy (SPIM) can not only provide high-resolution images but also enable the system to produce the high-speed, volumetric imaging through short period. However, the size and the costs of the traditional light sheet microscopy system are limited by the optical elements which are usually bulky and expensive. With the great development in metasurface based optical imaging system, more and more people begin to focus on the flat lens optical system reconstruction. Here, we demonstrate a metasurface based light sheet microscopy system which miniaturizes the system size and keeps the ability of the high-resolution biomedical images.

3.2 Metalens Light-sheet Microscope design

To prove the ability of light-sheet metalens that can be used for sectioning imaging, a customized light-sheet microscope has been built and the schematic is shown in Figure 15 (a). The 552 nm laser beam is collimated by L1(AC127-025-A, Thorlabs, NJ, USA) and expanded by using beam expander B1(GBE-02-A, Thorlabs, NJ, USA). The expanded beam was reflected 90 degrees by M1 (PF10-03-P01, Thorlabs, NJ, USA) and passed through the 6mm light-sheet metalens. To ensure the excitation light path perpendicular to the detector light path, another mirror M2 (PF10-03-P01, Thorlabs, NJ, USA) is mounted on a 3-axis stage. By changing the *z*-axis, the light-sheet focus point can be moved toward and backward to the objective lens which meets the objective focus distances. The *x*-axis can be used to control the beam waist position which the thinnest region will be used to excite the fluorescence dye during scanning tissue. The photography of the real optical system setup is shown in Figure 15 (b) and a three-dimension light path model created by

Solidworks is shown Figure 15 (c).

During imaging, the sample tissue is mounted flat on a single axis DC servo motor actuator (Z812, Thorlabs, USA). The tissue sample can travel along the *z*-axis, Figure 15(d), with a constant speed which is synchronized to the camera frame rate. The orthogonal (*en-face*) view will be processed by a *z*-stacking function of multiple *xv*-plane frames.

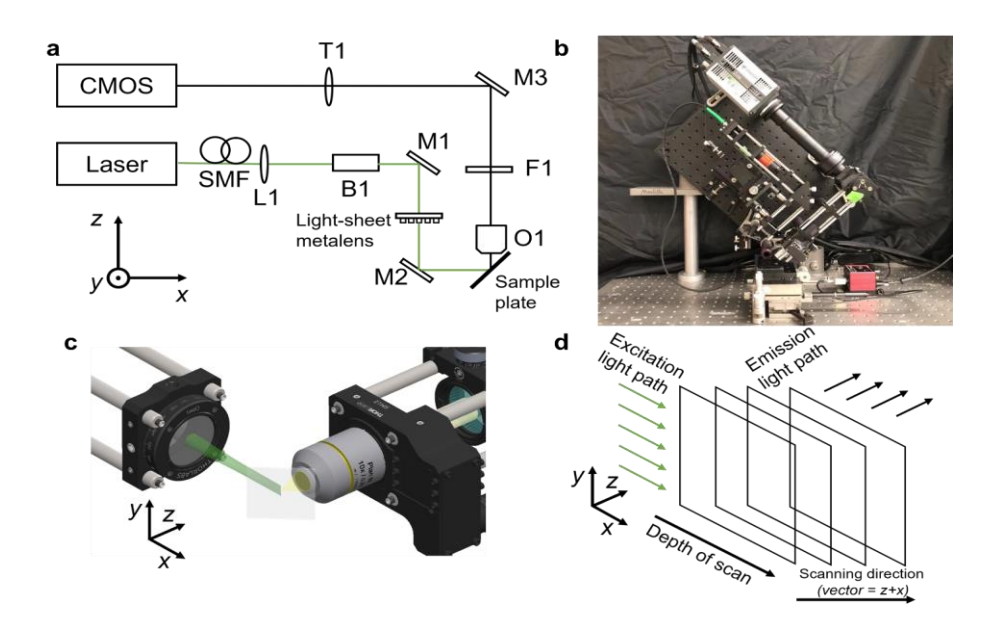


Figure 15 The diagram of microscope optical layout and image reconstruction. a, Solid green lines highlight the optical path of the excitation light. Solid black lines highlight the optical path of the emission light. SMF: Single-mode fiber. L1: Achromatic doublets. B1: Beam expander. M1-M3: Silver-protected mirrors. O1: 10X objective lens. F1: Long-pass filter. T1: 200mm tube lens. b, Photographic image of metalens light-sheet microscope setup. c, SolidWorks drawing of the light path at the scanning plate region. d, The 3D image reconstruction layout. The excitation light travels alone the x-axis into the tissue sample. The COMS camera receives the fluorescence 2D image in xy- plane. The reconstructed images are stacked alone on the z-axis. The en face image of the scanned tissue can be reconstructed at yz-plane. By changing the position of the reconstructed en face images alone on the x-axis, different depths of the scanned tissue structure can be noticed.

3.3 Metalens Light-sheet Characterization

3.3.1 Bright Field Resolution Result

Before testing the fluorescence imaging performed for the designed system, the bright field

resolution was characterized by using the USAF resolution target. Without installing the laser source, the imaging target was place on a xyz manual stage and moved to the objective lens focal plane. To increase the light intensity for CMOS camera capturing the clear image, a white LED light source was placed next to the target and transmit the light into the target surface. After fine tuning the distance between the target and the imaging plane, a grey scale USAF target image was recorded by the camera shown in Figure 16.

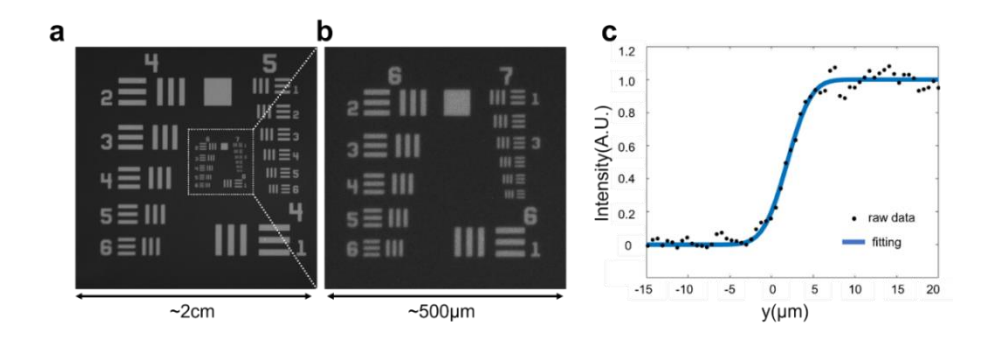


Figure 16 Experimental characterization of the metalens light-sheet microscope resolution. **a,** Experimental image of a 1951 USAF resolution target at low and high magnifications. **b,** A zoomed in USAF target group images. The metalens light-sheet microscope can resolve down to group 7 element 6 corresponding to a resolution of~2.2μm. **c,** The axial resolution of the metalens light-sheet microscope with fitting plot.

The camera image shows that the USAF group 7 element 6 can be detected which corresponding to a resolution of 2.2 μm. To have an accurate resolution result, a line pixel intensity data was collected by ImageJ and plotted by MATLAB. By applying the normalization algorithm to the collected data, the maximum intensity was converted to 1 and the minimum intensity value compressed to 0. In optical system design, the resolution is test by measuring the distance between 10%~90% normalized intensity. In this experiment, the tested bright field resolution is also close to 2μm.

3.3.2 Fluorescence Beads Resolution Result

After the bright field resolution characterization, the fluorescence resolution for the designed

imaging system is tested by the fluorescent beads phantom at laser wavelength 552nm. Even the imaging collection part is the same for both bright field and fluorescence mode, there are still differences. The bright field microscopy relies on the difference's absorption and reflection of light for different imaging samples. On the contrast, for fluorescence microscopy, the image signals are collected from the samples which emitted by the laser. In another words, the fluorescence microscopy provides a better resolution compared to the traditional bright field microscope. In this study, the metalens based light-sheet microscope not only provide the 2D fluorescence image for the bio tissue sample but also the cross-section images to detect the structure under the tissue surface.

To characterize the fluorescence resolution 3 different plane beads images are reconstructed by a series of continuous images. The metalens was designed for focusing the 552nm laser light, a longpass filter 561LP (LP02-561RE-25, Semrock, USA) was placed after the objective lens. To generate the fluorescent signals 200nm diameter beads (FluoSpheres Sulfate Microspheres, yellow-green, fluorescent, ThermoFisher, USA) was selected. The excitation and emission spectrum is shown in Figure 17. For phantom preparations, 20μl beads solution was collected by the pipette and transferred into a 2ml tube. After that, 1% water based agarose solution was prepared and mixed with the beads solution. The mixed solution was vortexed for 1min before loaded onto the glass slide to make the phantom more uniform. Next, the mixture solution was poured on a cleaned glass slide for curd. For the last step, the phantom slide was placed on DC servo motorized stage at objective lens focal plane for continuous imaging acquisition. The fluorescence resolution of the designed imaging system is shown in Figure 18. For the image, for the lateral resolution, in x and y axis the resolution is both 3 μm. For the z axis the resolution is about 27.5 μm.

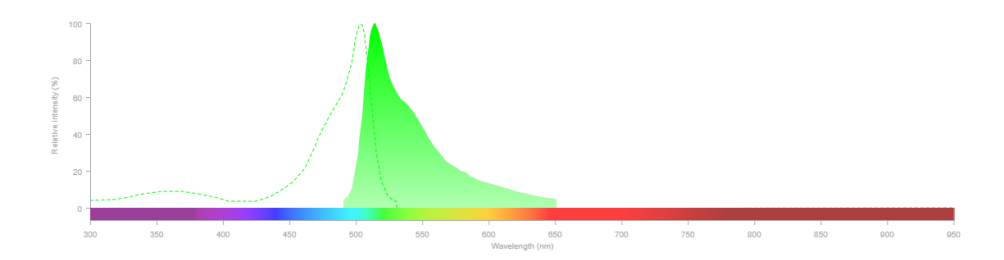


Figure 17 FluoSpheres Sulfate Microspheres, yellow-green, fluorescent beads spectrum.

To determine the designed system has a sectioning imaging effect, another fluorescence imaging experiment was tested with a larger beads diameter size (15 µm FluoSpheres Sulfate Microspheres, yellow-green, fluorescent, ThermoFisher, USA). The beads phantom was prepared with the same procedure and mount on a DC servo motorized stage at the objective lens focal plane. In Figure 19 the single beads target was detected by the camera at the center of the screen. During the beads target traveled along the z axis, a series of fluorescence images were captured. Before the beads was focused on the focal plane, the image was blurry because it was out of focused. After several frames, the beads target finally arrived to the focal plane and the edge of the beads was sharp and clear. Next, the beads target started moving passing the focal plane again and the donut shape structure showed up at the camera side.

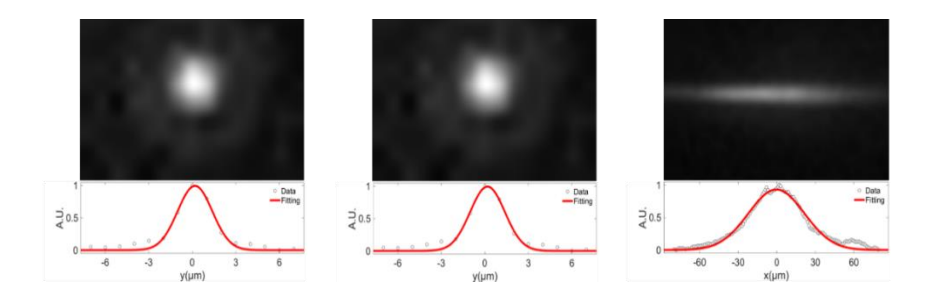


Figure 18 The fluorescence resolution characterization by using 200 nm beads. From the left to right, it shows the beads image in xy- plane, yz- plane, and xz-plane. The fluorescence resolution of the metalens light-sheet microscope is measured by using the FWHM of the targeting beads, shown at the bottom of each imaging plane.

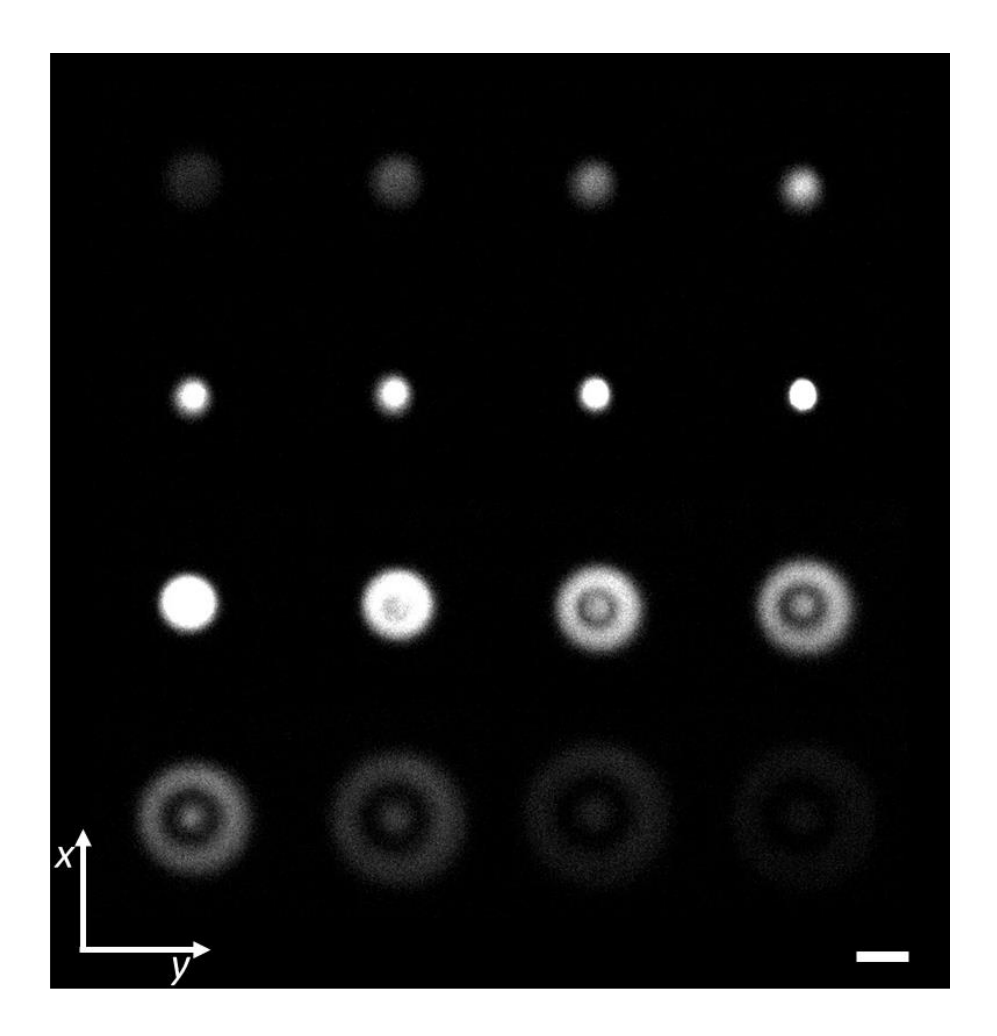
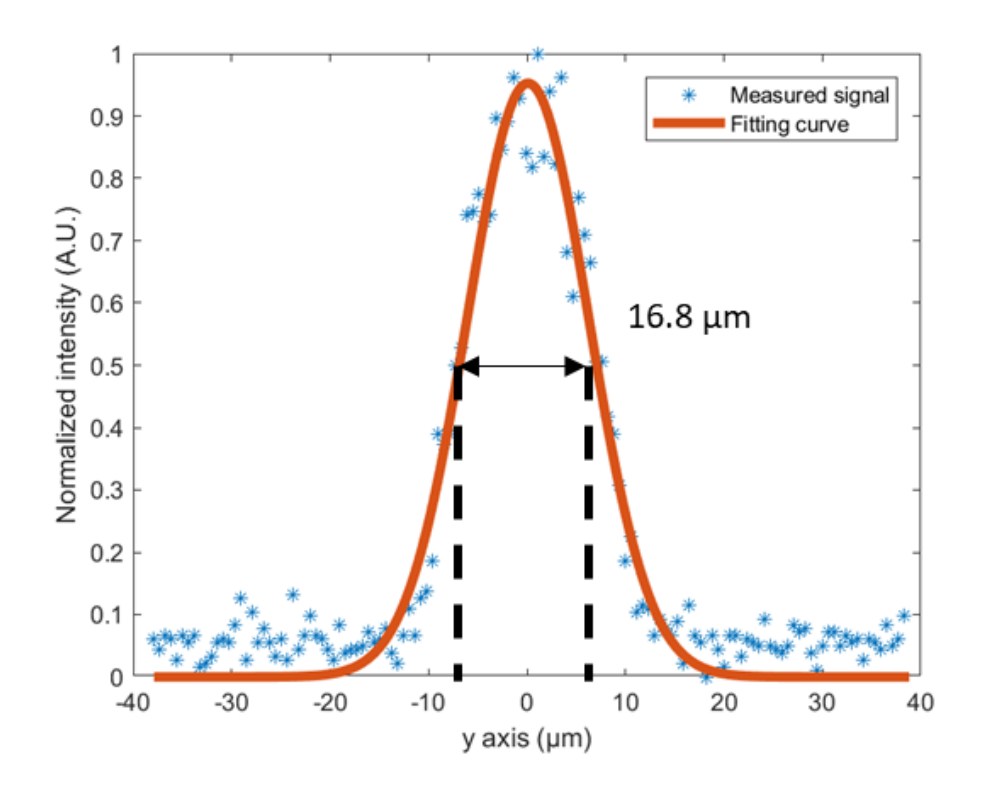


Figure 19 15µm dimeter beads sectioning experiment result. At the first several frames, the imaged beads were not reaching to the focal plane and image was blurry. After a certain frame, the beads target reaching the focal plane and the edge became sharper and clear. For the last several frames, the beads sample was moved passed the focal plane and became blurry again.

To prove the fluorescence resolution of the metalens light-sheet microscope is characterized correctly by the 200nm beads phantom, the 15µm beads phantom image was processed and plotted to measure the size by MATLAB. The measuring result is shown in Figure 20.



<u>Figure 20 15μm beads measurement result.</u> The plot shows that the imaged beads phantom is about 16.8 μm diameter which close to the real physical size.

3.4 Metalens Light-sheet Tissue Imaging Sample Protocol

Different from the traditional microscope hematoxylin and eosin stain (H&E) protocol, the light-sheet fluorescence imaging has less steps and show the volumetric tissue structure result. For the H&E slide preparations, the sample tissue needs to be fixed with the 10% formalin solution or 4% paraformaldehyde (PFA) for over 48 hrs [18, 38-40] and then embedded into the paraffin block for slicing. For the last step, the sliced tissue will be topical stained with different fluorescent dye and ready for imaging [41-43]. Due to the optical imaging limitation for the traditional fluorescence microscope, the tissue slide needs to be thin enough to avoid the blurry images [44, 45]. However, for LSFM imaging the fresh tissue only requires topical staining process and ready for 3D volumetric imaging. In Figure 21 it shows the tissue preparation comparison between the traditional H&E slide and light-sheet tissue imaging.

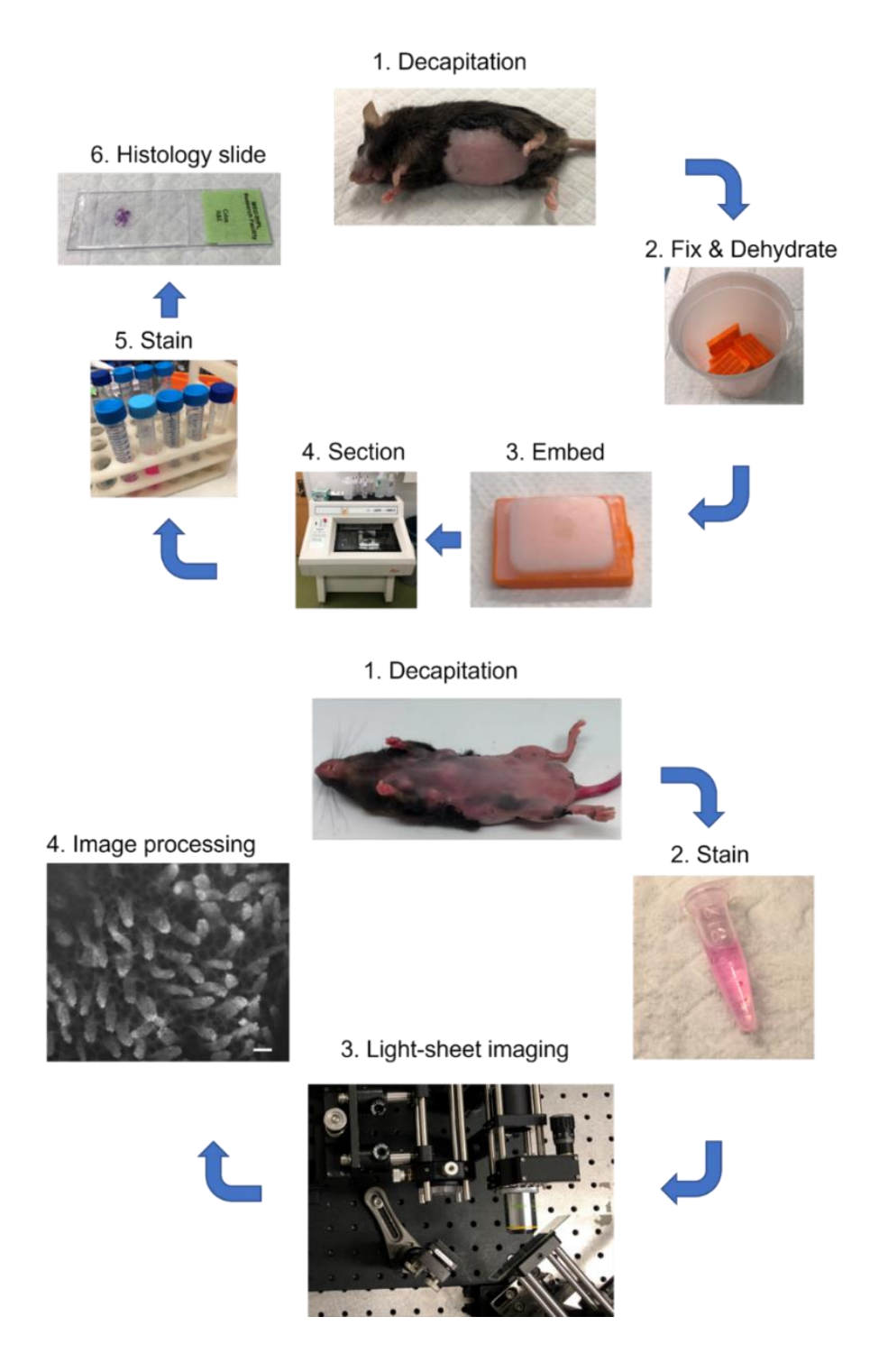
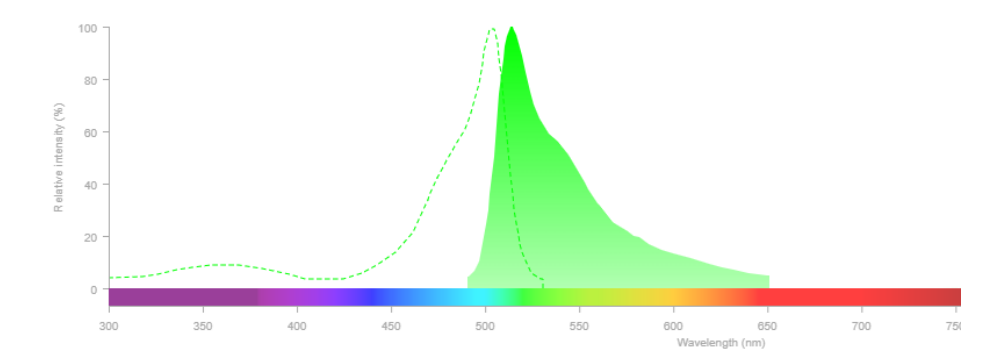


Figure 21 Conventional histology and metalens light-sheet microscope imaging protocol.

In this study, for *ex vivo* tissue imaging, the fresh tissue was harvested from the animal and washed by 1x phosphate buffered saline (PBS) to remove the impurities. After that the tissue was

topical stained with Cyanine Dye 3 (Cy3), concentration 10µg/ml (with 10% DMSO), for 15mins. The fluorescence spectrum is shown in Figure 22. Before imaging, the stained tissue was washed 5 times by PBS for 5mins each time to removed unstained fluorescence dye.



<u>Figure 22 Cy3 fluorescence spectrum plot.</u> The excitation max at 554nm and the emission max is at 568nm.

3.5 Metalens Light-sheet ex vivo tissue imaging

3.5.1 Metalens Light-sheet Microscopy fluorescence imaging of mouse colon tissue

To demonstrate the imaging quality of the light-sheet metalens in comparison with that of conventional light-sheet microscopy, we performed imaging on a fresh mouse colon tissue for *ex vivo* study. The inner surface of the colon tissue contains massive uniform cellular structures with small features (crypts) in lateral and axial directions.

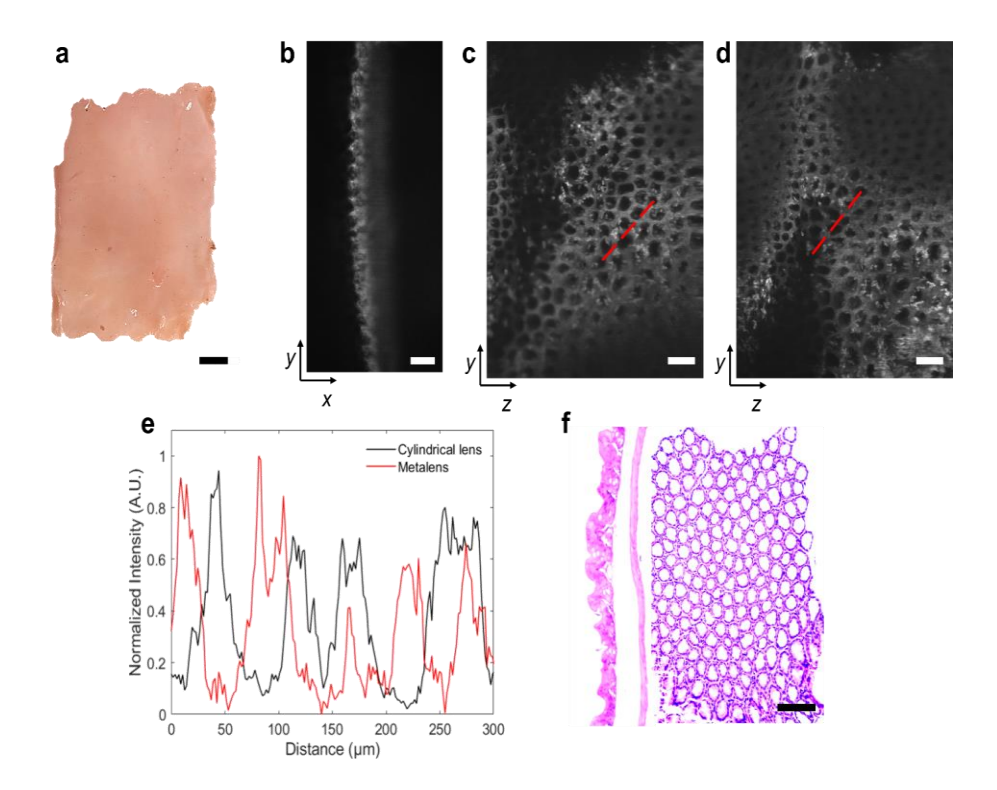


Figure 23 Mouse colon imaging result. Comparison of metalens light-sheet microscopy and cylindrical lens light-sheet microscopy images of mouse colon. (a) A photograph of the mouse colon stained with Cy 3 dye, scale bar: 1mm. (b) The objective view in *xy*-plane for the scanned tissue. The colon vertical structure can be excited by the metalens light-sheet and well-focused into the detection camera. Scale bar: 50μm. (c) and (d) The comparison reconstructed images of the colon between cylindrical lens and metalens. The *en face* view in *yz*-plane of the mouse colon surface (1100 x 885 μm) detected by traditional cylindrical lens light-sheet microscope (c) and metalens light-sheet (d). Scale bar: 100μm. (e) The intensities of a selected distance (300μm) along the red line in c and d are plotted to compare the performance of the cylindrical lens light-sheet microscope (black) and metalens light-sheet microscope (red). (f) The H&E slide image of the mouse colon captured by a commercial microscope, on the left vertical cut colon view, on the right *en face* view of the inner layer of the colon. Scale bar: 100μm.

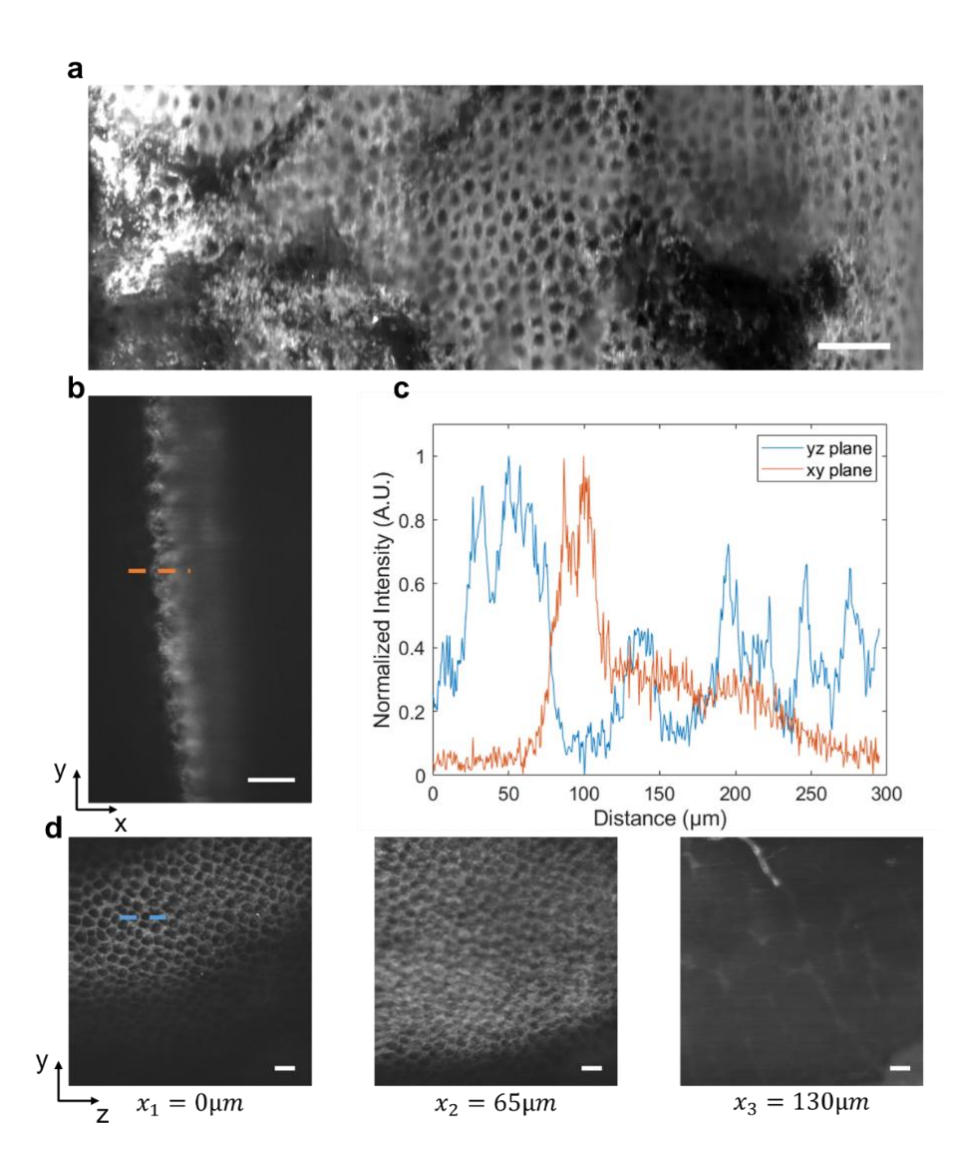


Figure 24 Metalens light-sheet microscopy imaging for mouse colon. (a) A reconstructed *en-face* plane of the mouse colon with a large area0.6x2.3mm. (b) The objective view in xy plane of the mouse colon. A 300 μm fluoresence signal was extracted from the image, normalized and plotted in c to show the contrast. Scale bar: $100 \,\mu\text{m}$. (c) The normalized fluorescence signal plot from xy plane (orange) and yz plane (blue) to show the metalens light-sheet microscopy has a great signal/background contrast. (d) The *en-face* plane of the mouse colon with different depth of x. From left to right, the x distance is 0, 65 and 130 μm. On the tissue surface, the structure of inner layer of the colon is well detected. With the depth of excitation increases, the bottom deeper layer of the colon appears, at $130 \,\mu\text{m}$, the blood vessel of the colon was detected. Scale bar: $100 \,\mu\text{m}$.

A large slice of mouse colon tissue was harvested from a 12-week female mouse after being euthanatized shown in Figure 23 (a). The fresh colon was stained with 100 μl Cy3 dye (10 μg/ml,

10%DMOS) for 10 min, rinsed with phosphate-buffered solution (PBS) for 5 mins, and rapidly imaged using our metalens light-sheet microscope. The colon tissue was scanned along the DC servo motor direction for 1800 single frames and reconstructed into a three-dimension model (Figure 24). With the high-magnification (10x) of the light-sheet metalens microscope, the *en-face* structures of the tissue can be imaged for different depths up to 100 μm. On the surface of the mouse colon, the epithelium structure can be clearly detected and with the increasing depth of the scan, the muscularis region can be reached (Figure 24).

To compare the metalens light-sheet microscopy with the traditional cylindrical lens-based light-sheet microscopy, the mouse colon tissue was imaged by both systems. During the metalens tissue imaging, the objective view in *xy*-plane of the colon is shown Figure 23 (b). The reconstructed *en-face* views in *yz*- plane by cylindrical lens and metalens are shown in Figure 23 (c) and 23 (d). Due to the colon tissue having a volumetric size, both light-sheet systems' two-dimension images can show the altitude differences. After selecting the top surface of the colon, the low ground part shows less optical signal, and the selected illumination plane shows a great tissue feature.

During the tissue imaging process, the signal to background noise ratio is one of the most important factors which directly represent the resolution. The normalized intensity plot crossing a long direction is shown in Figure 23 (e) for both conventional light-sheet and metalens. The contrast of the images shows good performance for both cases. The H&E images of the scanned colon tissue are shown in Figure 23 (f).

3.5.2 Metalens Light-sheet Micoscopy Imaging of Self-assembling Heart Organoid

Compared to the traditional fluorescence microscope which requires the imaging sample to be flat and thin for light focusing, light-sheet microscopy provides an excellent opportunity for researchers to study the small volumetric bio tissue samples. With the development of the organoid study, the inside structure of the organoid is a good target for people to monitor and evaluate the quality of the incubated organoid sample. Here, we demonstrate using the customized metalens light-sheet microscope imaging and reconstruct the 3D model of a volume size 1 mm^3 self-assembling heart organoids.

A 7-days incubated alive heart organoid was soaked into the Cy3 dye for fluorescence staining (Supplementary Information section I). After a short period of staining (30 mins), the heart organoid was rinsed and fixed for imaging. In Figure 25(a), the prepared organoid was imaged by a commercial fluorescence microscope (Thunder, Lecia, USA). From the image, some part of the organoid surface is clear to detect. However, due to the sample type, which is a volumetric tissue target, the edge of the organoid shows an unfocused effect and also the inner structure of the organoid is undetectable. To compare the imaging results between the traditional microscope system and the metalens-based light-sheet microscope system, we mounted the prepared organoid inside the agarose (1%) bed to avoid dried-up and affecting its spatial volume and imaged rapidly by the metalens based light-sheet microscope. A fast light-sheet microscope scanning (< 1 min) was applied to cover the entire area of the organoid sample. Then, the 3D structure of the sample was reconstructed by Amira (Thermo Fisher Scientific, USA) (Figure 25 (b)). A zoomed-in organoid surface image is shown in Figure 25 (c). The cell structures inside the organoid were recorded by the metalens light-sheet microscope. The system shows a good resolution result which each cell structure is about 15µm. A full sectioning image from the camera view (Figure 25 (d)) shows that the depth of light penetration is around 266.68 µm inside the organoid. To study the inner structure of the heart organoid, a set of stacking images in x-direction at different depths is shown in Figure 25 (e) (from 20 µm to 260 µm, step size: 80 µm) and Figure 26 by using ImageJ.

The large chamber structures start to appear with the increasing focusing depth.

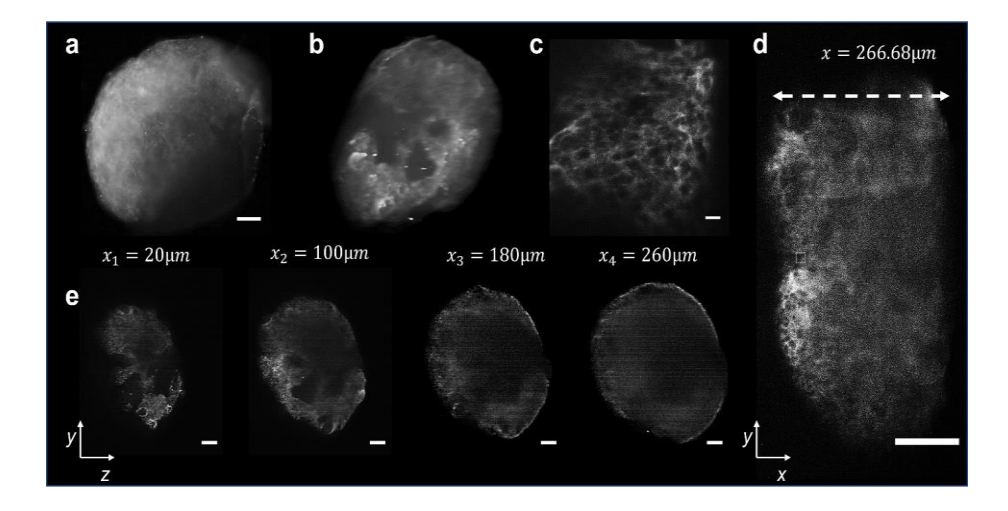
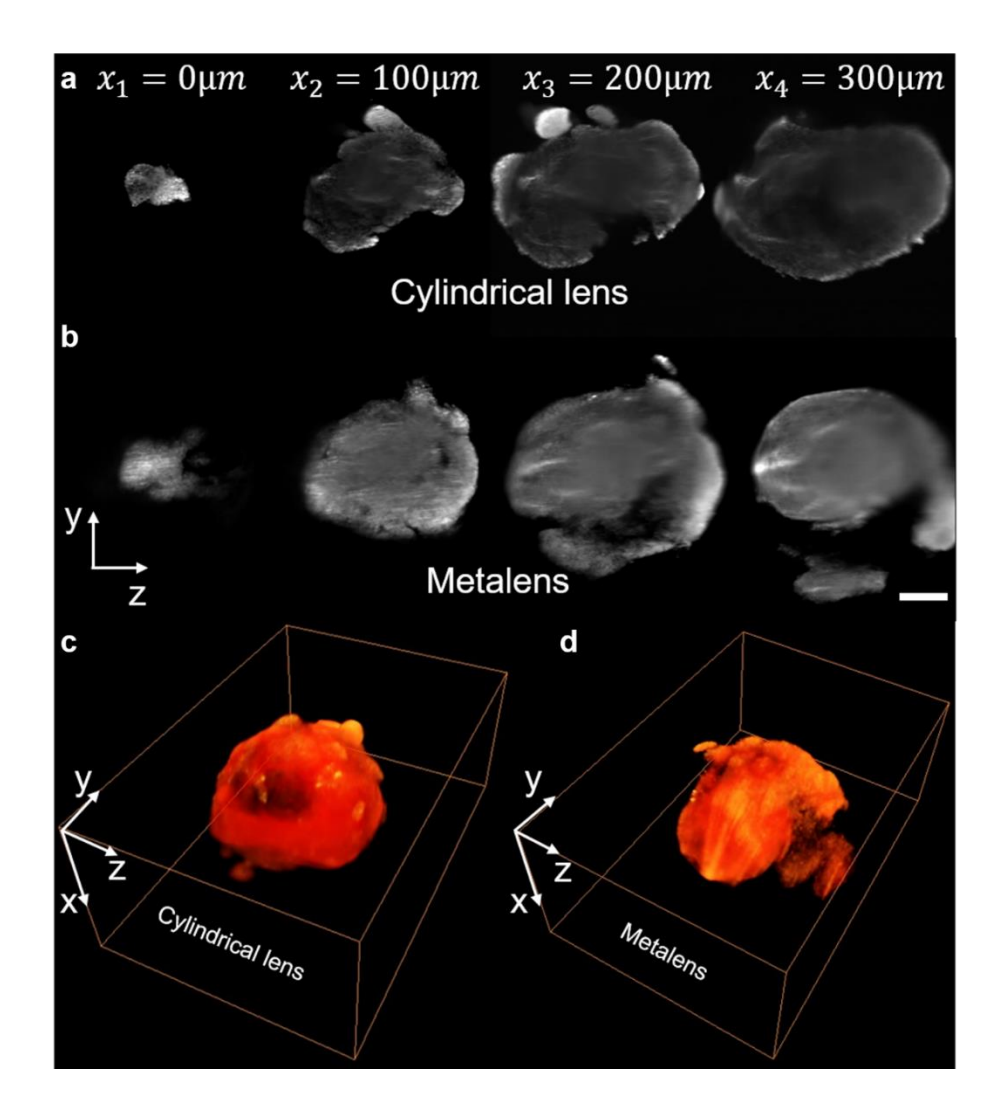


Figure 25 Ex vivo light-sheet microscope imaging of the self-assemble heart organoid. (a) A single organoid image captured by the commercial microscope (Thunder, Leica, USA). Scale bar: 100μm. (b) The 3D reconstructed image of the self-assemble organoid by Amira (Thermo Fisher Scientific, Massachusetts, USA). Scale bar: 100μm. (v) A zoomed-in organoid surface image, the single-cell structures can be detected by the metalens light-sheet microscopy. Scale bar: 20 μm. (d) The objective view in xy- plane of the fluorescence signal excited by metalens. The depth of light penetration into the organoid was about 266.68μm. Scale bar: 100μm. (e) The en face view in yz- plane with different depth of x. From left to right, the total depth of x is 260μm each step size is 80μm. Scale bar: 100μm.



<u>Figure 26 Metalens light-sheet microscopy images of heart organoid.</u> At different imaging depth from 0 to 300 μ m, the reconstructed organoid *en-face* view (*yz* plane) excited by the traditional cylindrical lens shown in (a) and the excited by the metalens shown in (b) scale bar: 200 μ m. (c) The 3D organoid model reconstructed by cylindrical lens. (d) The 3D organoid model reconstructed by metalnes.

3.5.3 Ex Vivo Volumetric imaging of Mouse Breast Tumor

To image the solid and bulky tissue target such as tumor tissue, the light-sheet beam used to excite the fluorescence dye is hard to penetrate the tissue surface and reach to a deeper area due to the tissue light absorption and scattering. To solve this issue, an index matching method and tissue clearing protocol were applied during imaging of the mice tumor tissue (Figure 27).

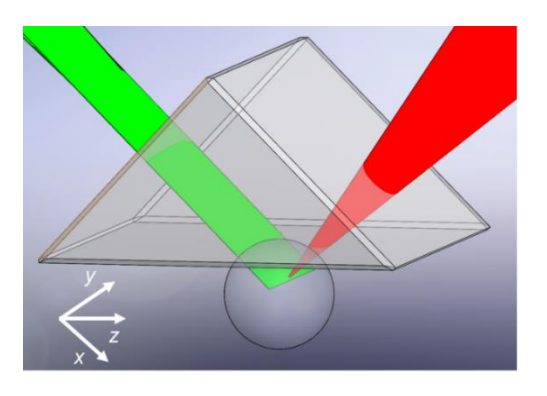




Figure 27 Microscopy index match and tissue clearing protocol. (a) The excitation and emission light path with prism for the light-sheet microscopy. The UV fused silica right-angle prism (PS614, Thorlabs, USA) was used to improve the laser quality when it entered the tissue due to the optical index matching. Before the imaging, 90% glycerol solution was applied on the tissue surface and attached to the prism. (b) The tissue clearing solution, FocusClear (CelExplorer, Taiwan), was used to clear the tumor tissue. The fixed tumor was soaked into the clearing solution at room temperature for 24 hrs.

A 5x5 mm² piece of breast tumor was harvested from the female mouse(Stain: MUC1/MMTV, Age: 14 weeks) after the euthanasia and fixed with 10% formalin for 24 hours, shown in Figure 28 (a). After the tissue fixation, the tumor was topical stained with Cy3(10ug/ml, 10% DMOS) for 10mins and rinsed in PBS for 5 mins. The prepared tumor tissue was finally processed by a single-step clearing method for 12 hours and ready for metalens light-sheet microscope imaging. In Figure 28 (b), it shows the camera view in *xy*-plane of the tumor during the scanning. By having the additional optical optimization steps, the light penetration range was extended from 266.68 μm to 350 μm. The sample tumor sample H&E image is shown in Figure 28 (c) and the 3D reconstructed tumor model is shown in Figure 28 (d). To discover the inner structure of the tumor tissue, the collected stacking images were processed by ImageJ reslicing. From the light-sheet incident direction *x*, at different layers inside the tumor from 0 to 350μm, the inner tissue structures such as lipids are captured, shown in Figure 28 (e) (i)-(viii). A zoomed-in lipids image at 120μm and 350μm depth are shown in Figure 28 (f) and (g).

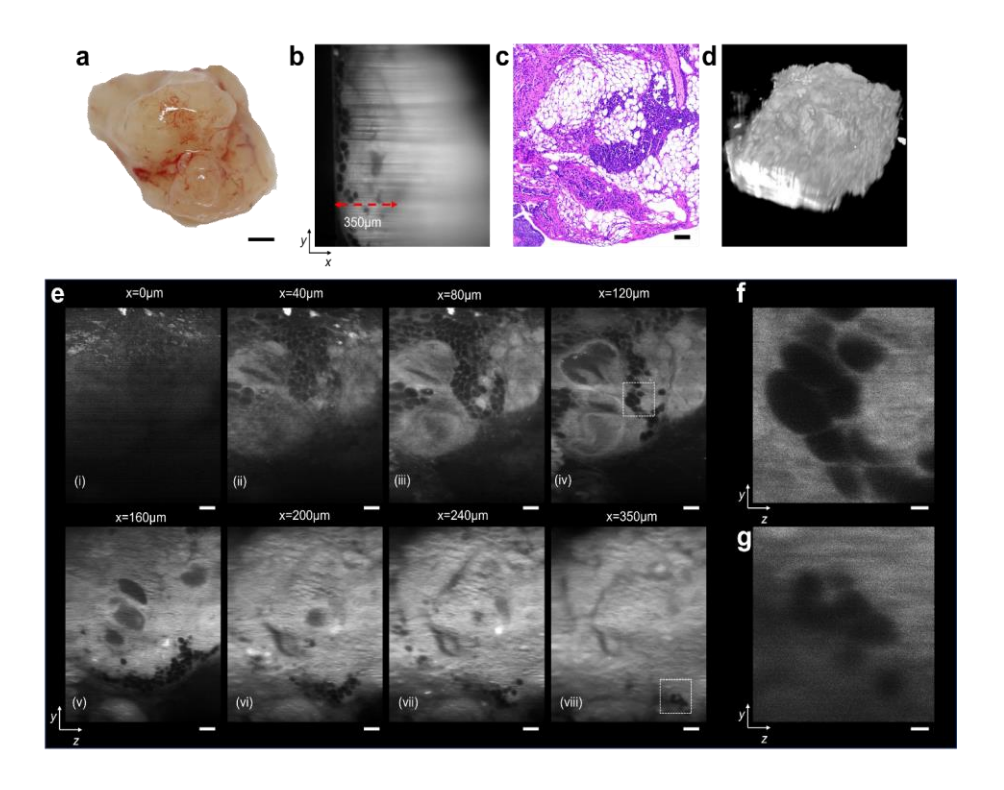


Figure 28 Ex vivo light-sheet microscope imaging of breast tumor using metalens. (a) Photographic image of the breast tumor, scale bar: 1 mm. (b) The objective view image in *xy*-plane of the tumor tissue, the depth of the light focus can be extended to 350μm. The inner structure of the tumor can be clearly detected. Scale bar: 100μm. (c) The histology slide of the same tumor tissue. Scale bar:100μm. (d) A 3D reconstructed image of the tumor tissue by Amira (Thermo Fisher Scientific, Massachusetts, USA). (e) The *en face* cross-sectional view in *yz*-plane of the tumor tissue with different depths of focus (i to viii: 0 to 350μm). Scale bar: 100μm. (f) A zoomed-in image from e(iv) at a depth of focus 120 μm. Scale bar: 20μm. (g) A zoomed-in image from e(viii) at a depth of focus 350 μm. Scale bar: 20 μm. With the increase of the light focused into the tissue upon 350 μm, the edge of the inner structure of the tissue was still clear.

3.6 Metalens Light-sheet in vivo tissue imaging

3.6.1 Metalens Light-sheet Microscopy in vivo Imaging of mCherry Modified Zebrafish

To prove the ability of metalens light-sheet microscope to detect the tissue inner structure, a genetic modified zebrafish (mCherry at heart region) was used as a target. The zebrafish embryo was prepared and incubated inside the incubator at 37.6°C before imaging. After 72 hours the zebrafish cardiomyocytes have reached a fully developed stage and are ready for imaging (Figure 29 (a)). The zebrafish embryo was embedded with 1% agarose on a glass slide which the embryo

stayed alive for more than 30 mins and its position was fixed for a stable imaging scanning. Then, the embryo was placed under the metalens light-sheet microscope at the desired position. During the imaging period, the shape and structure of the zebra heart can be clearly detected and recorded by the camera (Figure 29 (b)). The blood vessel, atrium and ventricle of the zebra were monitored during the imaging period. Several complete resting and contracting beating cycles of the heart were also recorded (Figure 29 (b)- (d)).

After the *in vivo* zebrafish embryo heart beating recording, we applied the optical flow algorithm using the Farneback method [47-49] to obtain more beating pattern information. This approach enables us to track and calculate beating vectors in the heart region. In Figure 29 ©, it shows the movement vectors directions during a single beating cycle. After that the heart beating rate was calculated and plotted in Figure 29 (d). The average beating rate is about 111.67 bpm.

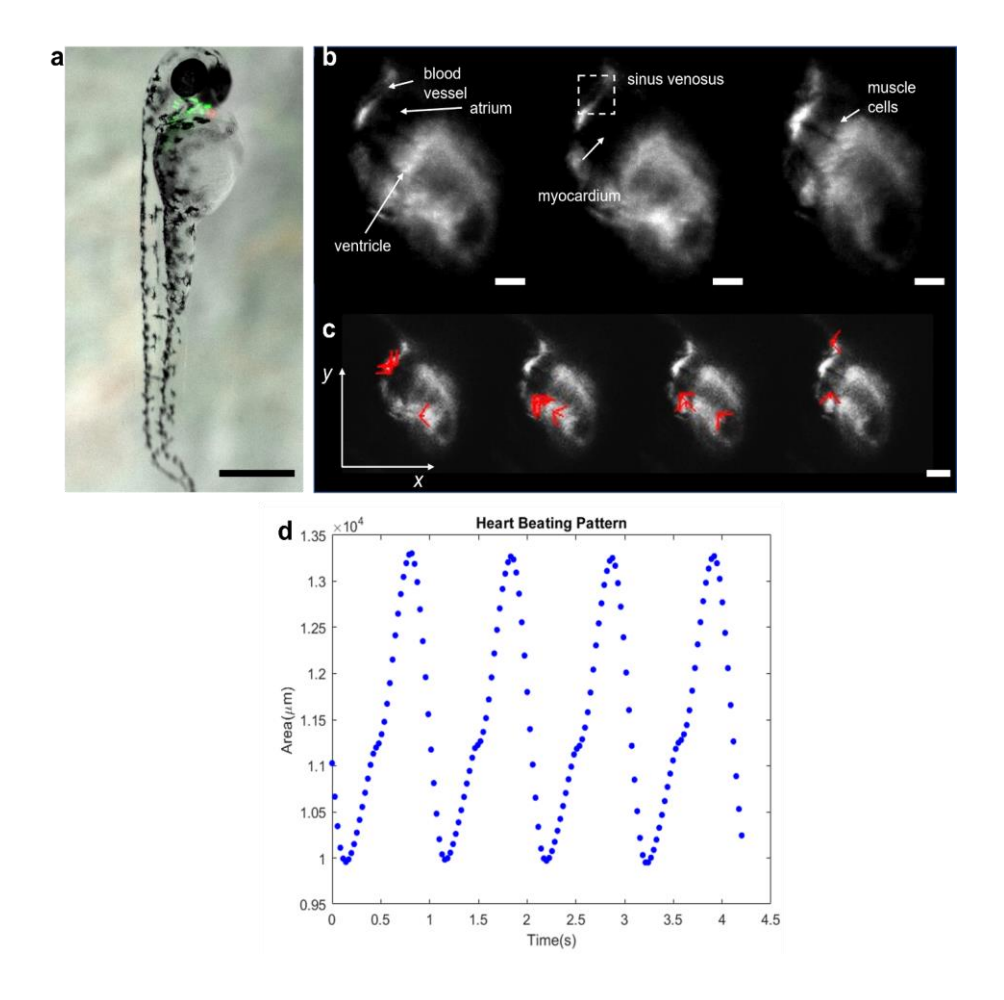


Figure 29 *In vivo* light-sheet microscope imaging of zebra cardiac system using metalens. (a) The stereoscope image (Leica M165 FC, US) of a 72-hours alive zebrafish with bright field and fluorescence mode (Gray: Bright field, Green: GFP, Red: mCherry). Scale bar: 1mm. (b) During the single segmentation cycle, objective view of the zebrafish heart at a different stage. From left to right: Resting stage, middle stage, and contracting stage. Scale bar: 25μm. (c) Using the optical flow algorithm to track the zebrafishheart movement. From the left to right, it shows a complete segmentation from the resting stage to the contracting stage. Scale bar: 25μm. (d) The zebrafish heart beating pattern for four segmentation periods. The average beating rate is around 112 bmp.

3.6.2 Metalens Light-sheet Microscopy In Vivo Mouse Blood Vessel Imaging

By applying the prism on the solid and non-transparent tissue surface will match up the optical index which increases the imaging depth. We experimentally used our light-sheet system on the small animals for imaging scanning. A 3-month-old normal mouse was selected for the ear blood vessel *in vivo* imaging. The pre-shaved and Cy3 injected mouse was placed on the single-axis

motorized stage with a warm pad and the ear area was applied 90% glycerol and attached to the prism lower surface (Figure 30 (a)). A stereomicroscope mouse ear vessel image is shown in Figure 30 (b) which is used to compare the vessel structures between our metalens-based light-sheet microscope result and the bright field image, shown in Figure 30 (c).

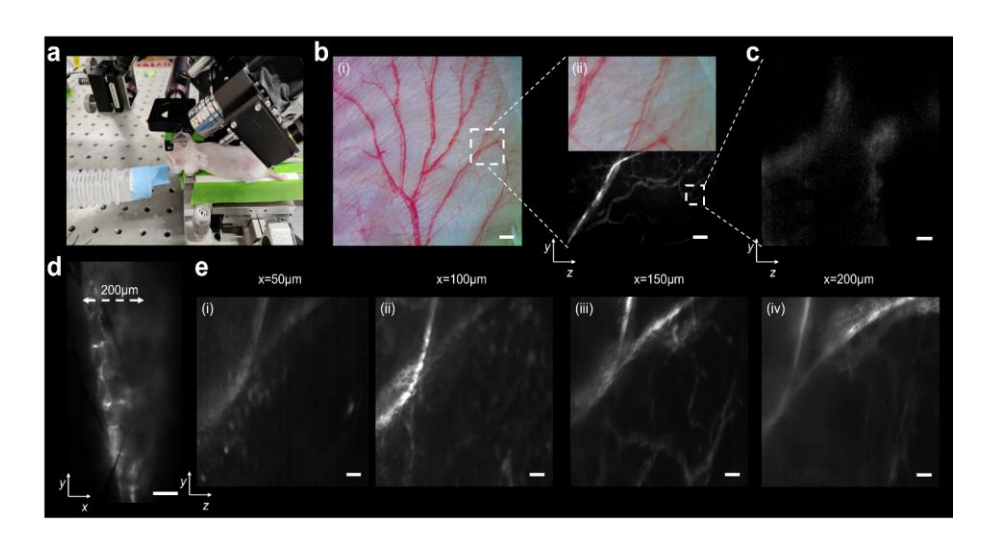


Figure 30 Metalens light-sheet microscope mouse-ear blood vessel *in vivo* imaging. (a) A photo for mouse ear mounted on the metalens light-sheet microscope system. The ear was attached to the prism with 90% glycerinum as index media. (b) (i) A mouse-ear vessel structure image captured by the stereomicroscope. Scale bar: 2.5mm. On the right, (ii), a zoomed-in image of the vessel structure stitched with the reconstructed metalens light-sheet microscope scanning imaging in *yz*-plane. Scale bar: 200μm. (c) A zoomed-in mouse-ear vessel image from b(ii). Scale bar: 10μm. (d) The objective view in *xy*-plane of the mouse ear blood vessel images. The blood vessel inside the mouse ear can be excited with a metalens light-sheet beam and shows a great contrast. The deepest area that can be detected by the camera is about 200 μm without any light scattering and optical tissue light absorption. Scale bar: 100 μm. (e) The reconstructed *en face* view in *yz*-plane of the mouse ear blood vessel. With the increase of the light focused into the tissue, the selected plan illumination can be detected up to 200 μm. Scale bar:50μm.

During the *in vivo* imaging, there were two image modes that we applied, non-scanning mode and large area scanning mode. For the non-scanning mode, we fixed the mouse ear position and directly observed the blood flowing condition through the objective view in *xy*-plane. During the imaging, the accumulated Cy3 particles can be clearly tracked inside the vessel and the motion trails were recorded by the camera, shown in Figure 30 (d). Later, the collected video data and

system settings parameters can be used to calculate the mouse blood-flowing speed.

For the large area scanning mode, the mouse-ear was traveled alone with the prism in a single direction at a constant speed, and a set of images was collected by the camera for 3D reconstruction. In Figure 30 (e), four *en-face planes* reconstructed images show the mouse ear inner vessel structure at different depths from 50 µm to 200 µm.

3.7 Metalens Light-sheet Microscopy Discussion

Compared to the other flat optical devices based on Huygens resonator principle, our design employs the high-index material TiO_2 and successfully extends the working wavelength into the visible range. Typically, the Huygens metasurface-based flat optics is widely used in the NIR study. The working wavelength range is limited by the material selections. However, because of the excellent properties of TiO_2 we introduced in the previous section, the fabricated device has a remarkable performance at the visible range. In addition, through our light-sheet metalens experiment, we demonstrated that the designed device has great potential in biomedical applications. For example, it can achieve the fluorescent imaging by using Cy3 dye and RFP (hChR2(H134R)-m Cherry) as targeting tools for *in vivo* or *ex vivo* study. According to the measurement results, the acceptance wavelength of the designed metalens can be extended from 532nm to 561nm indicates more biology samples could be imaged by the current microscope system.

In addition, compared to the other group's work using the metallic slit microlenses to generate a light-sheet for biomedical imaging [50], our design largely increases the illumination light-sheet effect width from 500 μ m to 6 mm. This may not only allow us to have a large FOV but also significantly reduce the imaging scanning time for 3D biological tissue reconstruct. On the other hand, the fluorescent image resolution has also been improved to 1.9 μ m which is 230% greater

than the reported microlenses light-sheet microscopy system. The capability of our current optical system setup satisfies the requirement for biomedical imaging applications such as cell culture and organoid culture studies.

The development of compact and thin optical devices are the key factor for the future biomedical instrumentation. In this work, we demonstrate that the metalens is a promising optical element for biomedical applications. The fabrication process of our designed light-sheet metalens is simple and costless which only requires the Electron Beam Lithography (EBL) and single lift-off steps compared to the traditional optical lenses. Moreover, to reduce the whole microscope system size, the MEMS scanner can be integrated into the system to achieve beam scanning.

In conclusion, the fabricated metalens can be used to replace the conventional cylindrical lenses in the fluorescence light-sheet microscope modules. The optical focusing properties of the designed metalens were tested and measured by several different custom-built systems. As a result, the plane wave diffraction effect can be explained by the Huygens lens principle which manipulates the wavefront by using individual nanostructures. In comparison to the previous Huygens lens-based metasurface, we optimized the nanostructure material and geometry which extended the working wavelength to the visible range. The high-refractive index and lower attenuation coefficient of titanium dioxide (NDs) allow us to produce high transmission efficiency metalens. Furthermore, the result of the designed system shows great potential in biomedical imaging systems. Particularly, we have demonstrated the superior performance of optical sectioning and 3D fluorescent imaging for our light-sheet metalens. Furthermore, with the development of nanotechnology, the costs and the fabrication complexity have been largely reduced indicating a promising future in miniaturization of optical components. For future work, the potentials and advantages of the light-sheet metalens suggest that a miniaturized, high-

resolution and low-cost scanning imaging system for biological and biomedical study can be achieved.

CHAPTER 4: NIR II WAVELENGTH FLUORESCENCE IMAGING SYSTEM

4.1 NIR II Fluorescence Imaging with Large-field-of-view Mesoscope

4.1.1 Large-field-of-view Mesoscope Research and Background

From the previous chapter we have successfully demonstrated the metalens based light-sheet microscope system at visible wavelengths for *ex vivo* and *in vivo* biomedical tissue imaging. By using the light-sheet excitation light, it can achieve fast volumetric tissue structure reconstruction. Although the collected data such as mouse tissue, zebrafish and heart organoid provide a great optical resolution for people to study the inner tissue structure, the light scattering and tissue absorption effects at deeper level under the tissue surface still prevent us to reconstruct deeper structure (>350µm) model.

To facilitate biomedical study, optical imaging technology has become a very important tool for early detection and diagnosis of diseases, due to its ability for non-invasive monitoring of the biomolecules, cells, and tissues [46, 47]. However, there are severe impediments for wide application of traditional optical imaging methods due to the light scattering by tissues and limited light penetration depth [48, 49]. To increase the light penetration depth, confocal microscopy is commonly applied for *in vivo* studies to provide high resolution fluorescence imaging [50, 51]. However, the weakness is obvious due to the trade-off between the scanning speed and resolution, which reduced the ability for imaging a larger field of view (FOV).

It has been well recognized that near-infrared light (NIR) is absorbed and scattered less by tissues [52-55]. An attractive NIR dye for *in vivo* study is the indocyanine green (ICG), which has been approved by FDA for human imaging. ICG can be excited with a 780nm laser source and emits in both NIR I (800~1000nm) and NIR II (1000~1400nm) fluorescence windows. Recently, ICG fluorescence in the NIR II window has been applied to image the biomolecules under the tissue

surface such as the blood vessel [55-57] as light scattering in that window is much attenuated [58, 59]. However, the detailed information of the tissue structure obtained was unclear because the magnification was not sufficient, and the intensities of the fluorescence signals were generally not strong enough. To address these issues, in this work, we report the design of a custom-made costeffective NIR II mesoscope system with an InGaAs camera, which has a compact size, and can ultra-sensitively fluorescence image in the short-wave infrared (SWIR) regime in high-resolution. The designed imaging system has a 2.7mm x 2.2mm field of view with a 3.48x magnification. Compared to the pervious groups' work using the macroscale microscope system for NIR II biomedical tissue study [60, 61], our system provides a minimum 6.9µm imaging resolution which is sufficient to capture the detailed tissue structures at a deeper layer under the skin. With traditional microscopy imaging, even using a small magnification objective lens to maintain a larger field of view, the optical working distance is still limited. To the contrary, the designed mesoscale NIR II imaging system has a 45.6mm working distance single-lens reflex (SLR) camera lens, which may easily enable live animal imaging, tissue preparation and imaging guiding surgery.

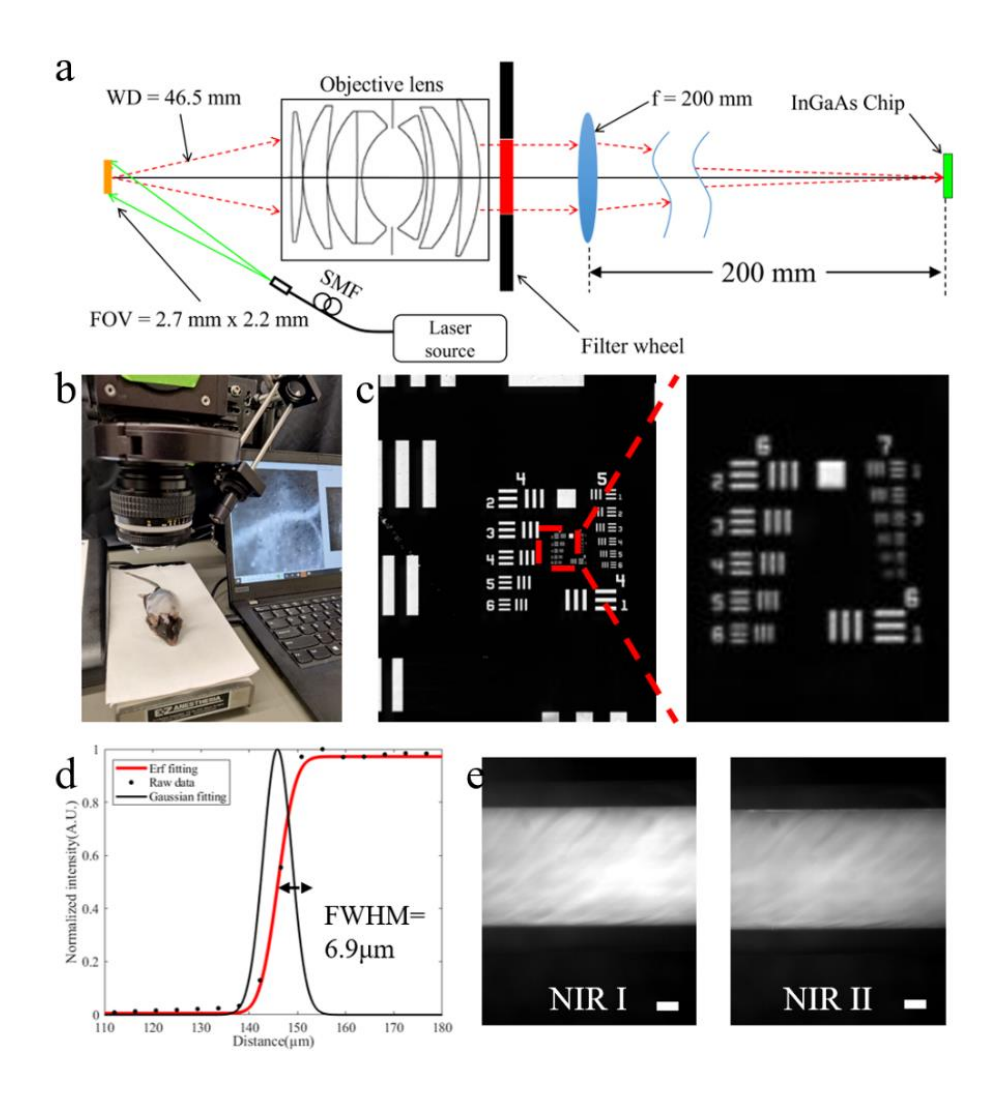
4.1.2 Mesoscope System Design and Method

To study the performance of the SWIR mesoscope system, ICG was selected as the fluorescence agent for *ex vivo* and *in vivo* tissue imaging. The schematic diagrams of the imaging system, i.e., SWIR mesoscope is shown in Figure 31(a). A photo of the actual system setup for *in vivo* imaging study is shown in Figure 31(b). For the fluorescence imaging, the samples were excited by a 780nm and an 808nm laser beam, which spread on its surface equally. The output of the laser power was both 3.5mW as measured by a power meter (PM100D, Thorlabs, New Jersey, USA), to ensure that the fluorescence intensities from excitation by different wavelengths were

comparable. For the emitted light, it was collected by the Nikon SLR camera lens (Nikkor, f=50mm, WD=46.5mm) after passing through the filter wheel containing two different fluorescence filters, i.e., band-pass filter (FF01-935/170-25, Transmission band: T_{avg} >93% 850-1020nm, Semrock, New York, USA) and 1064nm long-pass filter (edge wavelength λ =1086nm) (BLP01-1064R-25, Semrock, New York, USA). The filter wheel can easily separate the ICG signal into NIR I (800-1000nm) and NIR II (1000-1700nm) windows. The filtered light was focused by the 200mm tube lens (TTL200, Thorlabs, New Jersey, USA) into the InGaAs camera (Alizé 1.7, Photon etc, QC, Canada) with 100ms exposure time.

The bright field resolution was characterized by using the USAF target as shown in Figure 31 (c). The SWIR mesoscope has the full width at half maximum (FWHM) about 6.9µm shown in Figure. 31 (d). The system has a 3.48x magnification, which can detect the small features of the imaging samples such as blood vessels. The total FOV of the designed SWIR mesoscope system is about 2.7mm x2.2mm.

To demonstrate the system imaging ability for NIR I and NIR II windows, an ICG mixed agarose phantom with concentration 100µg/ml was placed at the imaging plane. The 808nm laser diode spreads the light equally on the target surface. The phantom height was adjusted until the edge of the sample is clear. By switching the filter wheel, the excited ICG signal in NIR I and NIR II can be separated and captured by camera shown in Figure 31 (e).



<u>Figure 31 SWIR imaging system design and characterization.</u> (a) SWIR mesoscope schematic. (b) A photo of the *in vivo* mouse imaging experiment setup. (c) The bright field USAF target image. (d) The resolution plot for SWIR mesoscope. The system has a 6μ m resolution. (e) The ICG phantom fluorescence images ($100\mu g/ml$), on the left NIR I window and on the right NIR II window, scale bar: $200\mu m$.

4.1.3 NIR II Mesoscope Ex Vivo Fluorescence Imaging

Due to the advantages of the NIR II window for tissue study, which include reduced autofluorescence and tissue scattering, the deeper tissue structure can be detected by the mesoscope system. To show the capability of our custom-made system, the mouse breast tumor tissue was imaged and shown in Figure 32 (a) and the H&E image is shown in Figure 32 (b).

The fresh tumor was harvested from a 4-month-old female mouse (MMTV/PyMT) and topically stained with 100µg/ml ICG fluorescence dye for 10mins. After the staining, the sample tissue was rinsed by PBS 5 times for 5 mins. The sample tissue was subsequently placed on the clean glass slide and mounted on the mesoscope imaging plane for imaging. For the fluorescence imaging, an output 3.5mW 808nm laser beam with beam size 5mm diameter was distributed on the tissue surface. The ICG NIR I and NIR II window images were collected, and the depth of focus was compared. For the NIR I window, the structure of the tissue surface can be clearly distinguished. However, with the increasing depth inside the tissue, the imaging resolution began to deteriorate with the small features appearing blurry. On the contrary, the NIR II window gave higher resolution images even when focusing deeper on the tissues. Representative images from NIR I and NIR II window with the same magnification of the same tissue areas are shown in Figure. 32 (c) and (d). For comparison of the tumor images, a zoomed in images are shown in Fig. 32(e) and (f) with the excitation wavelength at 808nm. It is obvious that at NIR II window, the inner tumor area, such as lipid structures, has a better contrast and sharpness than the result at NIR I window.

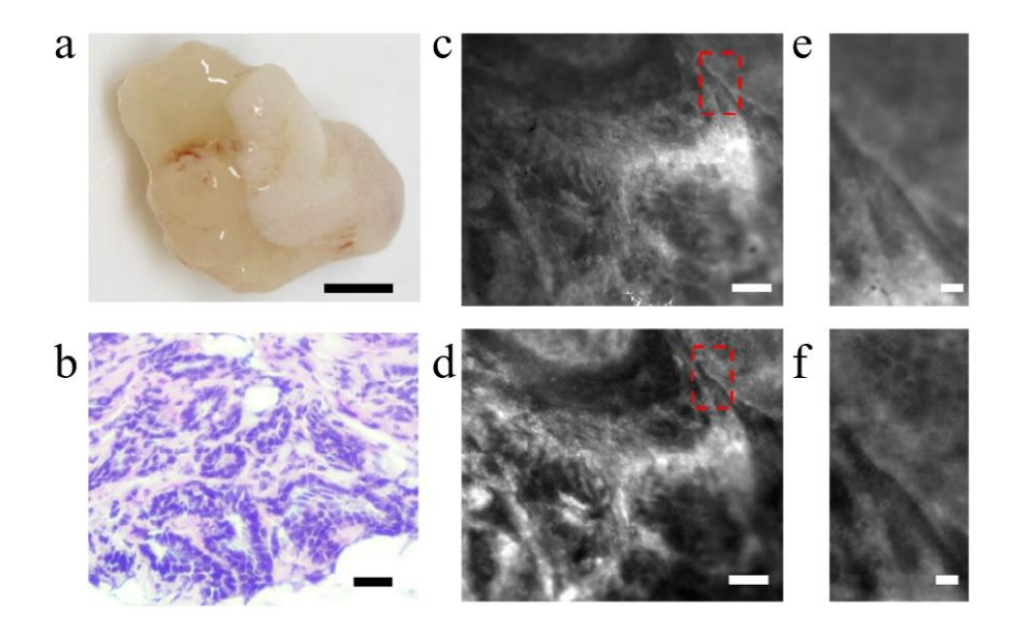


Figure 32 Ex vivo tumor tissue fluorescence imaging at NIR I and NIR II window by the SWIR mesoscope system. (a) Mouse breast tumor photo, scale bar: 2mm. (b) Breast tumor H&E slide, scale bar: 200 μm. (c) and (d) Fluorescence tumor image at NIR I window and NIR II window, scale bar: 200 μm. (e) and (f) The zoomed in tumor image at NIR I window and NIR II window, scale bar: 50 μm.

4.1.4 NIR II Mesoscope In Vivo Fluorescence Imaging

With the great results of NIR II imaging *ex vivo* demonstrated, we moved to a SWIR *in vivo* mouse imaging aided by ICG. All procedures performed on animal were approved by the University's Institutional Animal Care & Use Committee and were within the guideline of human care of laboratory animals. A tail-vein injection was applied to the mouse (MMTV/PyMT) with 200µl ICG (10mg/ml) 20 mins before imaging. In Figure 33 (a), a custom-made macroscale SWIR imaging result of the mouse ear region at the NIR II window is shown, which gave blurred images and blood vessels could not be clearly discerned. In Figure 33 (b) and (c), a set of high magnification mesoscope mouse ear images is shown to compare the imaging results from NIR I and NIR II windows. At the NIR I wavelength, the major blood vessel could be detected. However, at NIR II wavelength, not only the major vessels but also more capillaries which buried under deeper tissue layer were clearly observed.

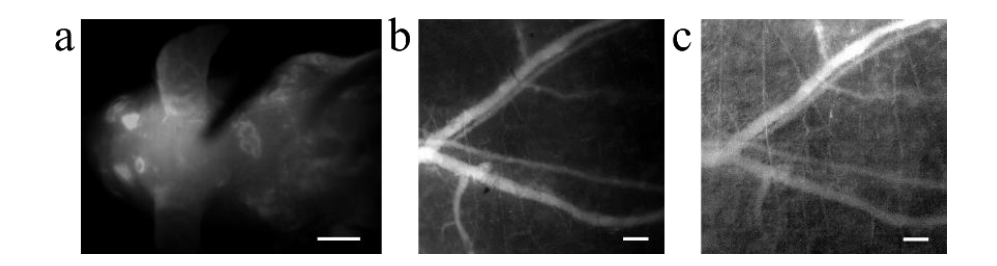


Figure 33 *In vivo* mouse ear vessel imaging at different NIR windows. (a) Macroscale fluorescence image at NIR II window, scale bar:1cm. (b) SWIR mesoscope vessel image at NIR I, scale bar: 200μm. (c) SWIR mesoscope vessel image at NIR II, scale bar: 200μm.

Another two different types of tissue images results for SWIR mesoscope are shown in Figure 4. A 4-month-old tumor mouse was tail-vein injected ICG and anaesthetized for imaging shown in Figure 34 (a). Two macroscale fluorescence images for tumor area and mouse tail at NIR II wavelength are shown in Figure 34(b) and (c). Two sets of mesoscope images at NIR I and NIR II results for different tissue types are shown in Figure 34 (d) and (e). For the tumor tissue, at NIR II wavelength, the deeper tumor shape such as vessel and porous structures showed a better contrast compared to the NIR I wavelength. The result from the tail vessel images is more obvious, at the NIR I wavelength due to the tissue scattering the vessel buried at deeper level does not have a sharp edge and clear shape. However, the NIR II wavelength provided us much greater fluorescence imaging resolution.

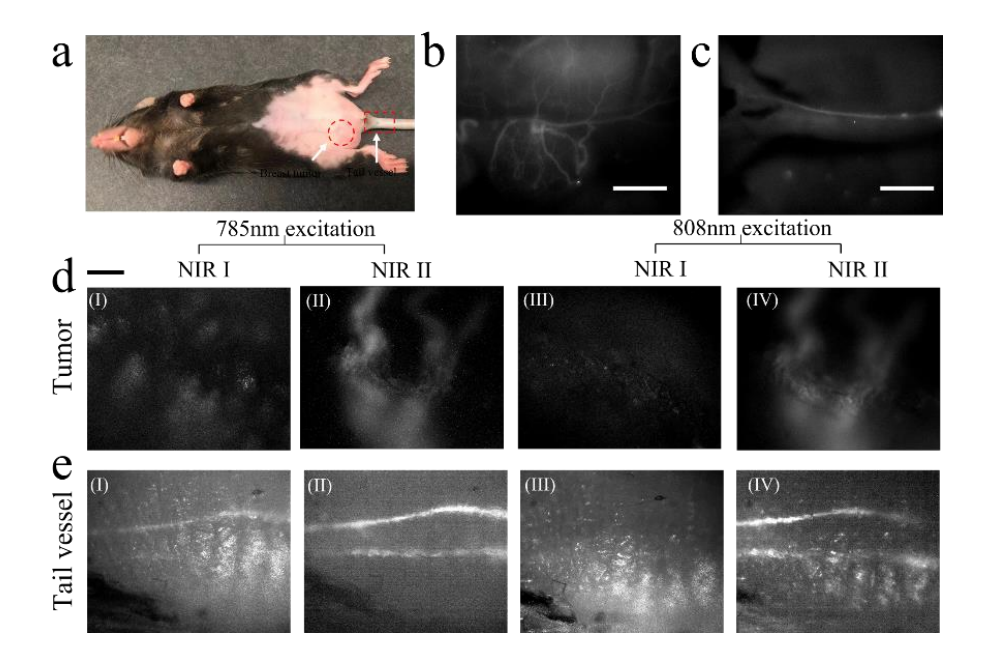


Figure 34 *In vivo* imaging in NIR I and NIR II windows by the SWIR mesoscope system. (a) A 4-month-old tumor mouse photo. (b) The SWIR macroscale fluorescence image at tumor region, scale bar:5mm. (c) The SWIR macroscale fluorescence image at tail region, scale bar:5mm (d) SWIR mesoscope image at tumor region for different NIR windows, scale bar:500μm. (e) SWIR mesoscope image at tail region for different NIR windows, scale bar: 500μm.

4.1.5 NIR II Mesoscope Discussion

This study reports the SWIR fluorescence imaging for ICG using a custom-made mesoscope system. While many groups have reported that the ICG in NIR II window has little tissue absorption and light scattering, those imaging systems gave low resolutions due to insufficient magnification and weak fluorescence intensities. As a result, although large veins in tissues in live mice can be detected using the InGaAs camera, small features such as capillaries are not visible due to the resolution limitations. In this paper, our work shows that using the custom-made cost-effective SWIR mesoscope, the imaging resolution can be significantly improved enabling the imaging of fine capillaries in mice, while keeping a larger FOV. We expect this new microscopy approach aided by NIR II window of ICG can become a useful technology for non-invasive biological imaging and imaging guided surgery.

4.2 NIR II Light-Sheet Fluorescence Microscope for Mouse Tumor Imaging

4.2.1 NIR II Light-Sheet Fluorescence Research and Background

With development of the biological system study, more researchers are interested in detecting the structure of the imaging sample for ex vivo and in vivo even at the molecular scale [62, 63]. To achieve the three-dimensional (3D) imaging reconstruction, confocal microscopy method[64] is mainly selected as the most common tool which provides high-resolution 3D images. However, due to the weak fluorescence intensity generated by the imaging target and the low scanning rate across a large field of view (FOV), the confocal microscopy is not an optimized way to recover the tissue structure for large area imaging [65]. Light-sheet fluorescence microscopy (LSFM) is such a powerful system which can provide high speed scanning rate, require low fluorescence signal and high imaging resolution [66, 67]. For light-sheet microscopy, in optical light path design, the illumination laser beam is focused by a cylindrical lens and formed a thin sheet which penetrates the imaging target to excite the fluorescence signals. For the detection path which is performed the light beam perpendicular to the illumination and collect the signals within a range inside the imaging samples from the surface to a deeper level. During the scanning, a set of highresolution cross section images of the sample are collected and can be used to reconstruct 3D model.

To study the inner structure of the imaging biological sample, light scattering effect has limited the image qualities when detecting the deeper tissue layers. People are using LSM to image small transparent target at visible range such as zebra fish, organoids, and the tissue sample after clearing method[68-70]. To improve deeper tissue imaging qualities, the longer wavelength such as at NIR II window, the light scattering and absorption by the tissue will dramatically reduce[71, 72].

There are several classes of fluorescence dye and probes at NIR II window for cell/tissue labeling[48, 54, 72]. Here we demonstrate NIR II LSM using the IR-iNP NIR IIb probe (Inorganic quantum dot based) which may extend the excitation and emission up to NIR II window (1000-1600nm). At this wavelength range, the reduced light scattering effect allows us to extend the imaging depth of a solid tumor tissue up to 1mm without any clearing method which provides a great potential for non-invasive tumor imaging study[58, 73, 74]. The collected sets of images also provide us a great opportunity to reconstruct the blood vessel structure tumor tissue structure for both *in vivo* and *ex vivo* experiments.

4.2.2 NIR II LSFM Optical Setup and Design

The customized imaging system is based on the traditional inverted LSM and the schematic of the optics design is shown in Figure 35 (a). An 808nm wavelength laser diode (LD808-SE500, Thorlabs, NJ, USA) is coupled into a single mode fiber and connected to the fiber port, L1 (PAF-X-2-B, Thorlabs, NJ, USA) to collimate the illumination beam. The collimated beam passes through a relay lens, L2 (AC254-30-B, Thorlabs, NJ, USA) and L3 (AC254-100-B, Thorlabs, NJ, USA) to expand the beam. A cylindrical lens C1 (LJ1567RM-B, Thorlabs, NJ, USA) forms the beam to a light sheet and focuses on the imaging plane. A right-angle optical prism P1 (PS610, Thorlabs, NJ, USA) is placed between the illumination and collection light path, shown in Figure 35 (b). A thin layer of 80% glycerol is applied to the gap between prism and imaging sample to compensate optical refractive index mismatch and improve the light quality when enter the tissue. For the fluorescence signal collection, an objective lens (Nikon 10x 0.3 CF Plan, Tokyo, Japan) is focused perpendicular at the light-sheet illumination in *y-z* plane, shown in Figure 35 (c). The collection beam is filtered by F1 (LP920-25.4, Midopt, IL, USA and BLP01-1064R-25, Semrock, New York, USA) to remove the excitation laser beam. Then the collimated light focused by the

tube lens L4 (AC254-100-C, Thorlabs, NJ, USA) onto the InGaAs camera (Ninox 640 II, USA). For the sample scanning, a single axis stage is driven by the actuator and synchronized with the camera frame rate.

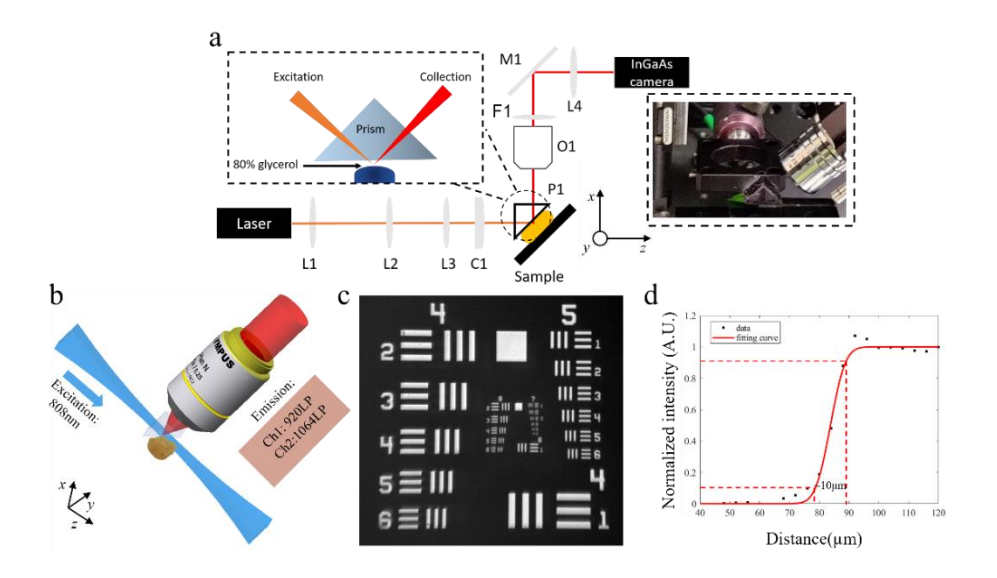
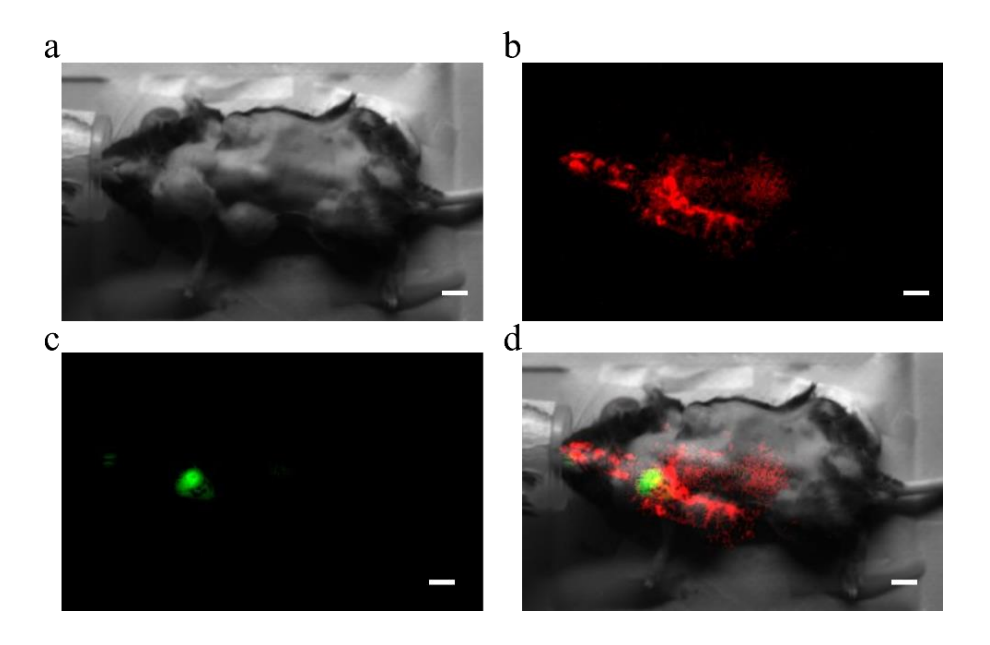


Figure 35 NIR II light-sheet microscopy schematic and characterization. (a) NIR II SLFM schematic. (b) The photo of the SLFM sample imaging plane. (c) The 3D model of the excitation and emission light path. (d) The USAF target bright field image captured by collection path. (e) The line intensity plot of the USAF target image, from $10\% \sim 90\%$ the resolution is about $10\mu m$.

To characterize the designed imaging system resolution, an USAF target was select to detect the collection side bright field resolution shown in Figure 35 (d). By normalized intensity plot of a single line from the USAF target is shown in Figure. 35 (e), from the $10\%\sim90\%$ intensity curve, the resolution of the LSM is about $10\mu m$.

4.2.3 Imaging Sample Preparation For In Vivo

For *in vivo* imaging, a single mouse (Stain: MUC1/MMTV, Sex: Female, Age: 10-month) was tail vein injected with 150 µl IR-iNP NIR IIb probe (5mg/ml) based on its weight (5mg/kg)[75]. After the injection, the mouse was anesthetized with isoflurane and monitored by a customized NIR II macro-scale imaging system to track the fluorescence signal full body distribution shown in Figure 36 (a).



<u>Figure 36 The macro-scale images of the imaging mouse after injection.</u> (a) The bright field image of the injection mouse. (b) After injection 10 mins, the wholebody mouse fluorescence image at NIR II window. (c) After injection 24hrs, the whole-body mouse fluorescence image at NIR II window. (d) Combined 10mins and 24hrs fluorescence image. Scale bar: 1cm.

After 10 mins injection, the mouse was imaged by the NIR II macro-scale imaging system. From Figure 36 (b), the main body blood vessel structure is clear the see which indicates that the injection particles are flowing around the mouse body. From Figure 36 (c), after injection 24 hrs, the same mouse was imaged again to detect the fluorescence signal distribution at NIR II window. As we expected, the particles are accumulated at the tumor region and the vessel signals became weaker. Once the signal was detected from tumor area, the SLFM *in vivo* imaging can be implemented.

4.2.4 NIR II LSFM Ex Vivo Tumor Imaging and 3D Reconstruction

To demonstrate the potential application of the NIR II SLFM, in Figure 37 (a), it shows the result of the objective view in *x-y* plane during image scanning. The result shows a great tissue structure from its surface to the deeper layer inside the tumor. From the image, at the surface of the tumor sample, the tissue texture is solid and have a curved shape, with the light increasing to

the deeper area, the capillaries nets inside the tumor appears and the multi-hole structure appears. The H&E slice image of the same tumor is shown in Figure 37 (b). The reconstructed 2D *en-face* images perpendicular to the illumination direction is shown in Figure 37 (c). A larger FOV (4x2mm) image of the tumor provides a great contrast result of the tissue structure. Finally, a 3D reconstructed model of the scanned tumor sample is shown in Figure 37 (d). The total volume of imaging region is about 2964x1280x740µm³.

To show the effects of light scattering at different emission wavelength, here we used the NIR II LSM scanned same tumor tissue block with two different filters, 920nm long-pass filter and 1064nm long-pass filter. The imaging result is shown in Figure 38 (a)-(i) and (ii). From the objective view, x-z plane, by using the 920nm long-pass filter the depth of the imaged tumor inner structure is about 400µm and the deeper tissue structure became fuzzy and blurry. However, at the NIR II window which the emission light above 1000nm, the imaging depth can be extended to 740µm. To directly observe the imaging depth limitation at different wavelength, in Figure 38 (b) and (c), the reconstructed *en-face* images for the same tumor sample compared with different light penetration effects in z direction. In Figure 38 (b), the emission of 920nm wavelength, the depth limit approximately reaching the maximum at $z=500\mu m$. However, at a long emission wavelength, 1064nm, the depth limit can be extended to 1mm, and image remains good contrast, shown in Figure 38 (c). The comparison results directly prove the suppressed scattering effect at longer wavelength[49]. In Figure 38 (d), the line intensity at same position with different emission wavelength also shows that, with the increasing depth limit the red curve (>1064nm window) always give us a sharper peak than the blue curve (>920nm window).

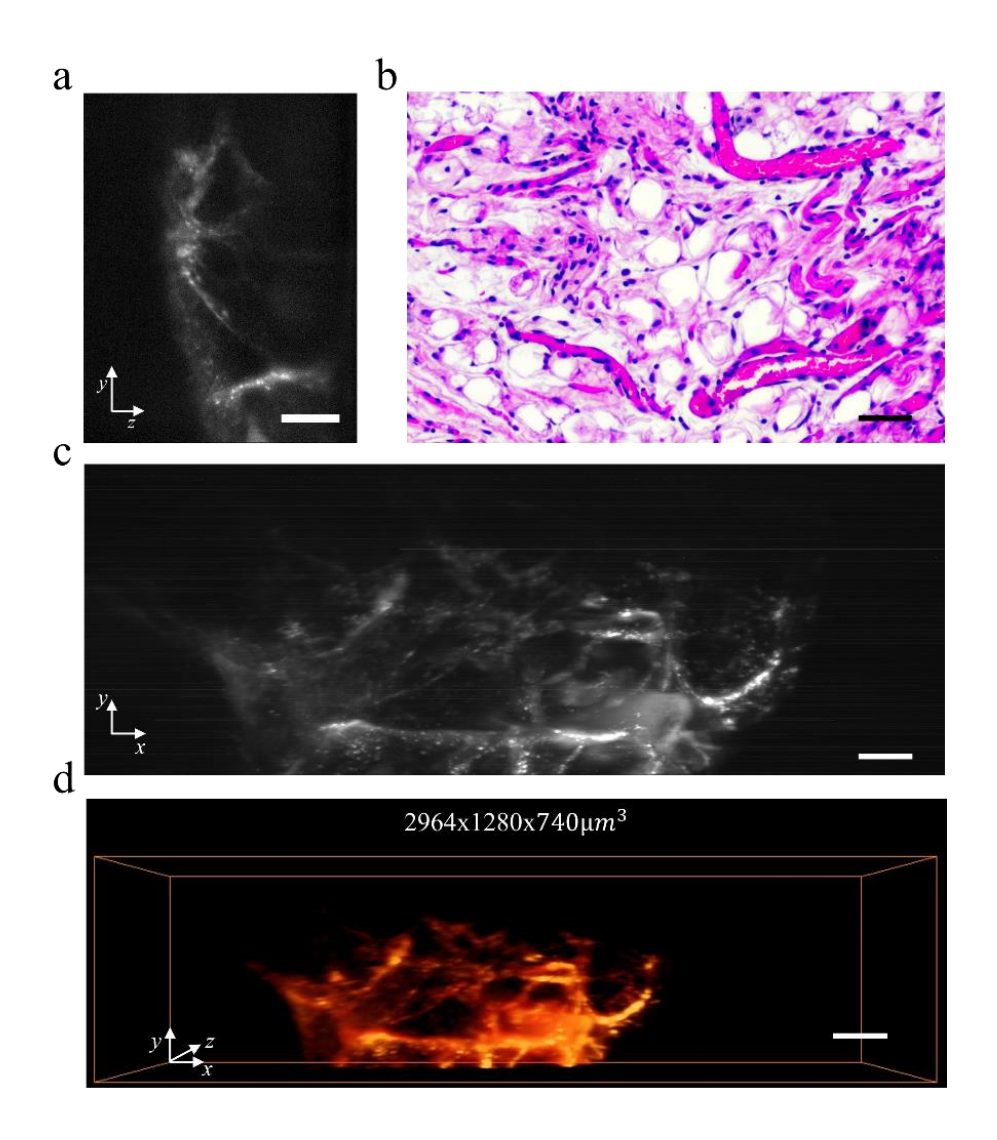


Figure 37 ex vivo NIR II SLFM tumor imaging result. (a) The objective view image at x-y plane during scanning. Scale bar: 200 μm . (b) The same H&E slice image of the same tumor tissue, scale bar: 100 μm . (c) The reconstructed en-face image of the scanned tumor tissue, scale bar: 200 μm . (d) The 3D reconstructed tumor model of the scanned sample, the total volume is 2964x1280x740 μm^3 , scale bar:200 μm .

After discussing the suppressed scattering at different emission wavelength, we scanned the mouse breast tissue close to the solid and firm area shown in Figure 39. In Figure 39 (a), the reconstructed *x-z* plane image has a larger FOV about 4mm x 2mm. From the image, the multiple bright dots indicate the cells distribution around the tumor area. An intensity alone the white dash line (Figure 39 (c)) shows the background and signal contrast.

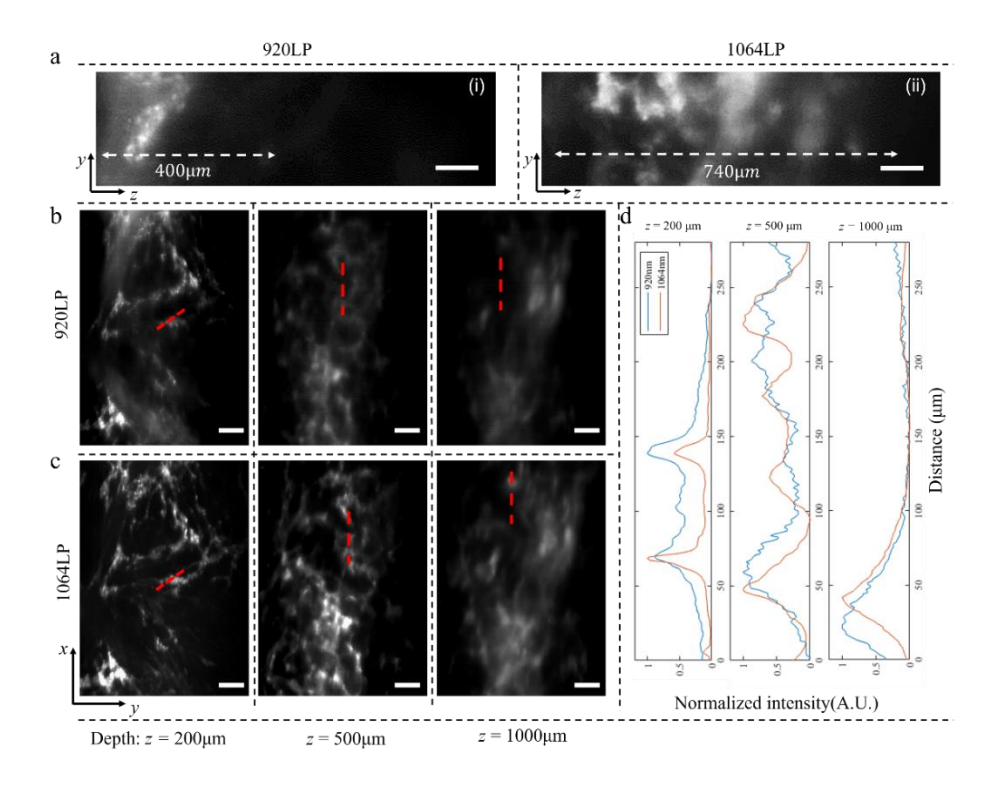


Figure 38 LSFM ex vivo mouse tumor imaging result at different emission wavelength. (a) The objective view in x-z plane, (i) 920nm long-pass filter and (ii) 1064nm long-pass filter, scale bar: $100\mu m$. (b) At emission >920nm window, left to right the results of depth limit in z direction increases from $200\mu m$ to $1000\mu m$. (c) At emission >1064nm window, left to right the result of depth limit in z direction increases from $200\mu m$ to $1000\mu m$. Scale bar: $200\mu m$. (d) Line intensity plot at different depth limit, the blue curve: >920nm and red curve: >1064nm.

A zoomed in image (200μm x 150μm FOV) from (a) is shown in Figure 39 (b). The intensity plot of the smallest fluorescence dot signal is shown in Figure 39 (d). By fitting the collected signal with Gaussian function, the FWHM of the bright spot is approximately 15μm which satisfies the cell size. Also, at the objective view in *x-y* plane, the structure inside the tumor is well detected shown in Figure 39 (e). With increasing the image depth, from the tumor surface to a deeper layer, the vessel structure and loose porous structure are well demonstrated. To have a better understanding about the tumor tissue structure, a 3D model was created by using the stacking scanning images, shown in Figure 39 (e). From the 3D model, it presents the solid tissue region is located at the left part of the reconstruction window block and a cross shape vessel net is connected

near the center region.

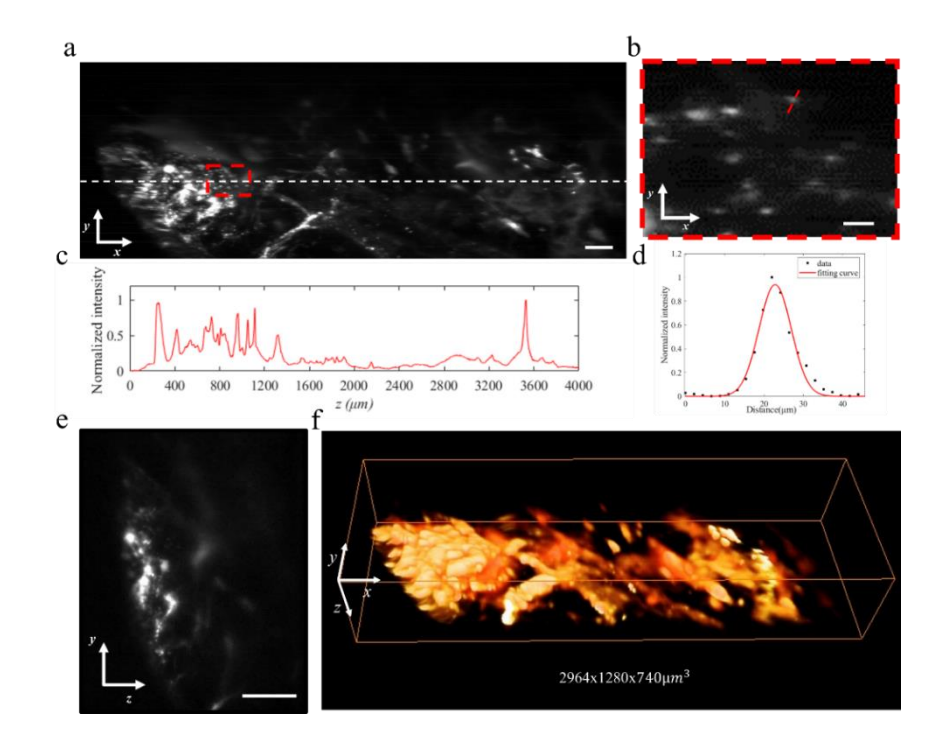


Figure 39 ex vivo scanning tumor images and 3D model reconstruction. (a) A reconstructed x-z plane tumor image with FOV 4x2mm, scale bar: 200μm. (b) A zoomed in image from (a), the single cell of the tumor is well detected, scale bar: 40μm. (c) Intensity plot alone the white dash line in (a) shows a great contrast between the background and fluorescence signal at NIR II window. (d) The zoomed in region single cell plot, the FWHM is approximately 15μm. (e) Objective view image in x-y plane during scanning, scale bar: 200μm. (f) The 3D reconstructed tumor tissue model.

4.2.5 NIR II SLFM Non-invasive In Vivo Optical Sectioning Imaging of Mouse Tumor

NIR II LSFM enabled the ability of non-invasive *in vivo* sectioning images for mice tumor study. To demonstrate the imaging performance of our system, the MUC1/MMTC breast tumor was injected the IR-iNP NIR IIb probe 24hr before imaging. The mouse was anesthetized and embedded on a warm pad to keep the body temperature during imaging. To detect the tumor vasculature's structure and blood flow behavior, the mouse was scanned in a fixed position under the LSM and short videos were recorded during imaging. In Figure 40 (a), it shows the cross-section view of the tumor capillaries distribution near to the tumor region at NIR II window. A

series of images was recorded and processed to track the fluorescence signals flowing inside the vessels, shown in Figure 40 (b). The green dash spot shows the signal starting position, and it flows along the white arrow direction to the red dash spot.

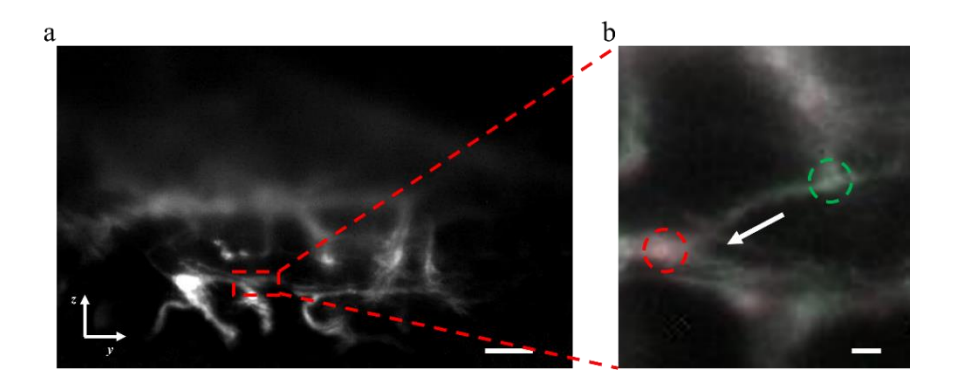


Figure 40 *In vivo* mouse tumor vasculature image. (a) The objective view in x-y plane for tumor area vessel structure, scale bar: 200 μ m. (b) The zoomed in image from (a) shows the blood flow direction from green spot to red spot along the white arrow, scale bar: 20 μ m.

4.2.6 NIR II LSFM System Discussion

In this chapter we have presented the customized NIR LSM for *in vivo* and *ex vivo* biomedical tumor study. We have shown that by using our approach the scanning imaging depth at NIR II window can be extended up to 1mm without any clearing method. It also proves the at the light scattering and absorption by the tissue have been suppressed at a longer wavelength. The designed NIR II LSM system provides series of high-resolution stacking images which may also use to reconstruct the 3D model for the scanning samples. As we mentioned in pervious section, for *ex vivo* study the *en-face* plane image which perpendicular to the illumination path provides a great contrast between the background and the fluorescence signals. With the increasing depth along the illumination direction, the deeper layers tissue structure can be easily detected such as capillaries and single cell. The fluorescence resolution of the designed system is about 10µm which is enough to capture the important information during biomedical tissue study. The reconstructed 3D model of the scanned sample shows a good result in tissue structure such capillary network. Due to the

high sensitivity of the InGaAs camera, the acquisition time for single image frame can be less than 50ms which allows us to scan a large FOV (4x2mm) sample area within 2mins.

For *in vivo* tumor structure study, the NIR II LSM is not only a non-invasive imaging system but also can provide a continuous cross-section image which allows us to track the blood flow direction and inner layer tissue structure. Finally, we conclude that the NIR II LSM is a considerable promising imaging system for biomedical tumor study. The capability of the designed system shows a great potential for non-invasive tissue scanning for tumor diagnosis and 3D model reconstruction.

4.3 NIR II Fluorescence Imaging System Discussion

In this chapter, we demonstrated 2 different fluorescence optical imaging system at NIR II wavelength. During the imaging experiments, we have proved that at NIR II window, the light scattering and tissue absorption effects have been largely reduced which allow us to detect the deeper tissue under the sample surface.

Table 2 Comparison of visible and NIR wavelength system imaging result.

Imaging System	Magnification	Excitation	Emission	Resolution	Penetration Limitation
Metalens LSFM	10X	552nm	561nm	3µm	350µm
NIR II Mescope	3.48X	780/808 nm	>1064nm	6.9µm	4mm
NIR II LSFM	10X	808nm	>1064nm	10µm	740µm

After reviewing the results, we found that at visible wavelength, the sectioning tissue imaging can reach to 350µm with clearing method applied before the optical resolution decreases. However, at NIR II window, without extra tissue handling technique such as tissue clearing the light penetration can be easily extended to 740µm which gives us a great opportunity to reconstruct a large volume of tissue structure. A table of different system comparison is shown.

CHAPTER 5: MOEMS BASED NIR CONFOCAL MICROSCOPE

5.1 NIR Confocal Microscope Research and Background

Based on the last chapter imaging result, we found that for biomedical tissue imaging especially for deep tissue structure 3D reconstructions the excitation and emission wavelength is critically important for both resolution and light limitation controls. To increase the sample imaging resolution, confocal fluorescence microscope is an essential tool for biomedical study. In this chapter, we present a customized MOEMS based NIR miniaturized confocal microscope handheld system which not only keep the high imaging resolution but also achieve fast large area scanning.

The basic confocal microscopy method can be tracked back to the mid-1950s developed by Marvin Minsky[76, 77]. However, this useful technique has not been widely applied until the laser technology and digital computing speed full developed. In the 1980s, the first fluorescent biological confocal microscope system was demonstrated[78, 79]. The key factor for developing the confocal microscope system is point illumination and spatial filtering technique which people always place a pinhole at the middle of the light collection path to block the scattering light. With the fast development of fiber technology, the single mode fiber (SMF) which the core size is about 6~10µm can be used as spatial filter to create confocal effect.

Due to the special optical properties, the confocal microscope not only provides the high lateral resolution imaging but also good axial resolution. To achieve the ultra-resolution, the confocal microscope requires high performance optical lens which makes the whole system bulky and complicate to use. On the other hand, the scanning speed also limits the imaging field of view which is hard for people to image a large tissue sample. To overcome these challenges, we purpose an ideal to integrate MEMS scanner and superconducting nanowire single-photon detector

(SNSPD) technology together to achieve fast real time confocal imaging and large field of view.

5.2 Thin-Film PZT Piezoelectric MEMS Scanner

Different from the traditional galvo scanner, using MEMS scanner device can reduce the system size and provide faster scanning speed. Compared to the electrostatic and electrothermal actuation MEMS device, thin-film piezoelectric actuation mechanism (PZT) MEMS device requires low driving voltages and currents [80-83]. To accomplish our design and needs, our collaborator Dr. Hiroshi Toshiyoushi's group provided us 4 different 2D thin-film PZT MEMS scanner (in table 3). The designed scanner uses thin-film lead-zirconate-titanate oxide (PbZrTiO3, PZT) as piezoelectrical material to generate the force to change the mirror direction for beam scanning.

Table 3 Thin-film PZT scanner.

Device	Device thickness	Fast axis
		frequency
Y853-3-4-3	20µm	2690Hz
Y853-2-5-9	30µm	4328Hz
Y853-2-4-3	30µm	4267Hz
Y853-2-4-6	30µm	4237Hz

In Figure 41, it shows the schematic of the designed PZT MEMS scanner. There are 8 individual pins to control and sensing the device. By applying the voltage at V1~V2 and V5~V6, the outer actuation arms (slow axis) can drive the mirror vertically. To increase the mirror tilting angle, the input voltage of pins 1 and 2 or pins 5 and 6 should have a 180° phase differences. To drive the inner axis (fast axis) horizontally, another 2 inputs voltage with 180° phase differences will be applied to V3 and V4. The PZT scanner scanning schematic is shown in Figure 42.

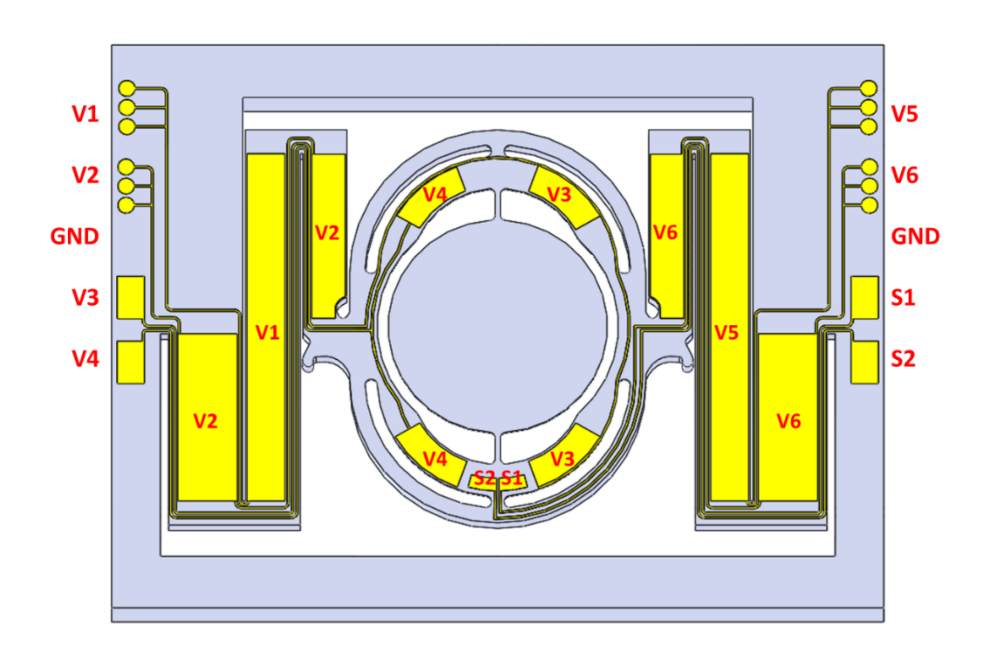


Figure 41 Thin-film PZT MEMS scanner schematic.

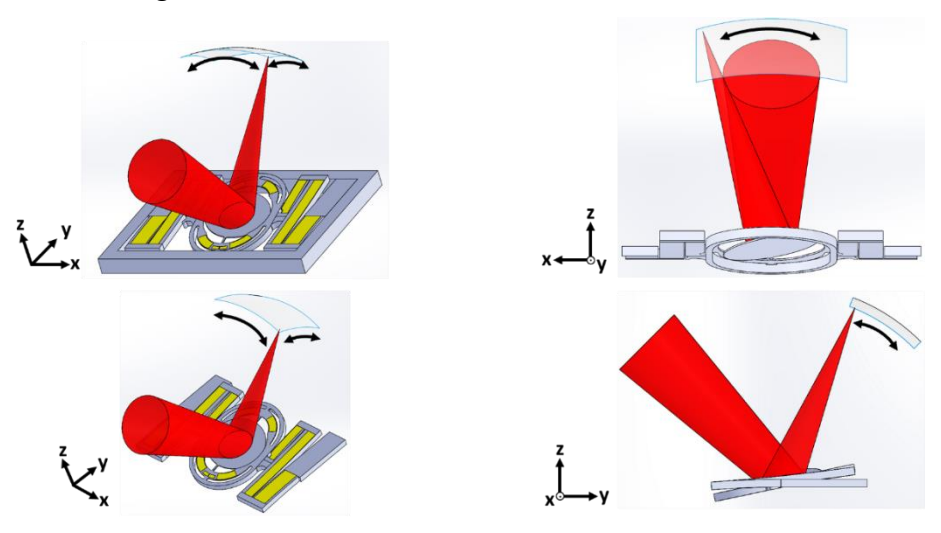


Figure 42 Thin-film PZT MEMS titling schematic.

The PZT MEMS scanner has a 2mm diameter gold coated mirror at the center area to achieve the 2D beam scanning. In our design, the collimated beam size is about 1mm size at 785nm wavelength which is perfectly selected for this MEMS device shown in Figure 43

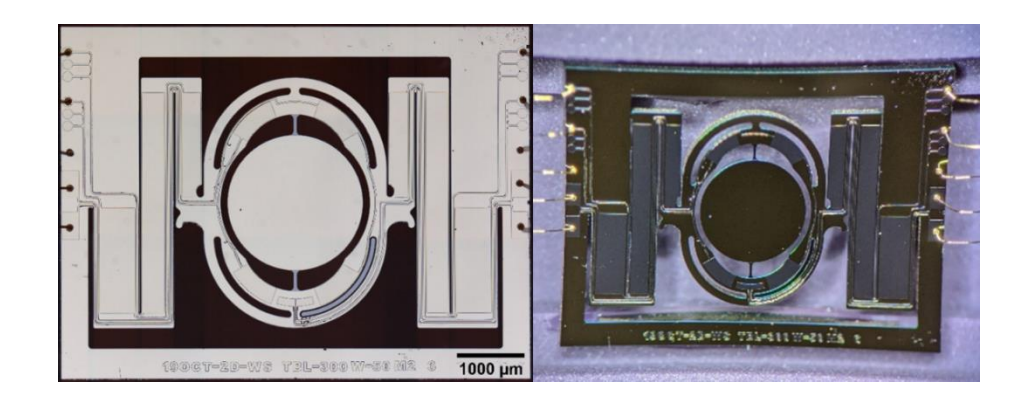


Figure 43 Thin-film PZT MEMS scanner with a 2mm gold coated mirror.

To have a large scanning area, the PZT MEMS scanner was tested with a sweeping voltage source for both axes to find the resonate frequency shown in Figure 44 and Figure 45.

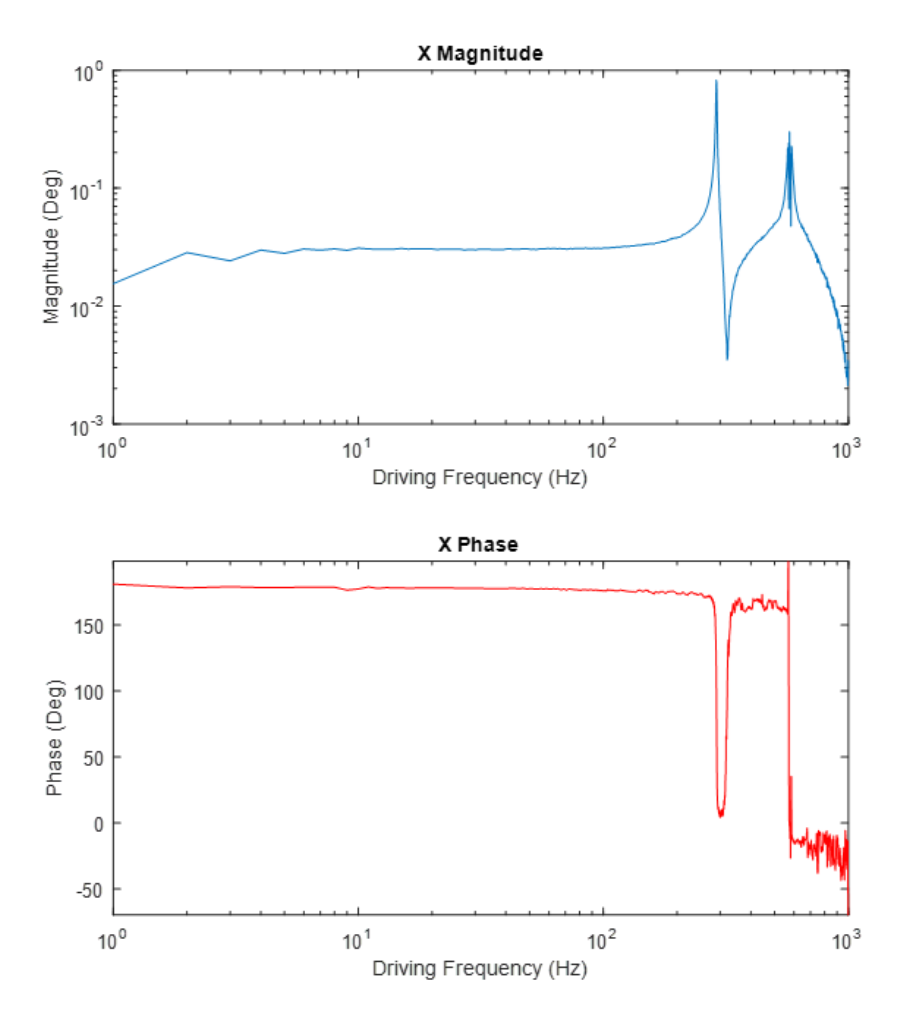


Figure 44 PZT MEMS scanner outer resonate frequency.

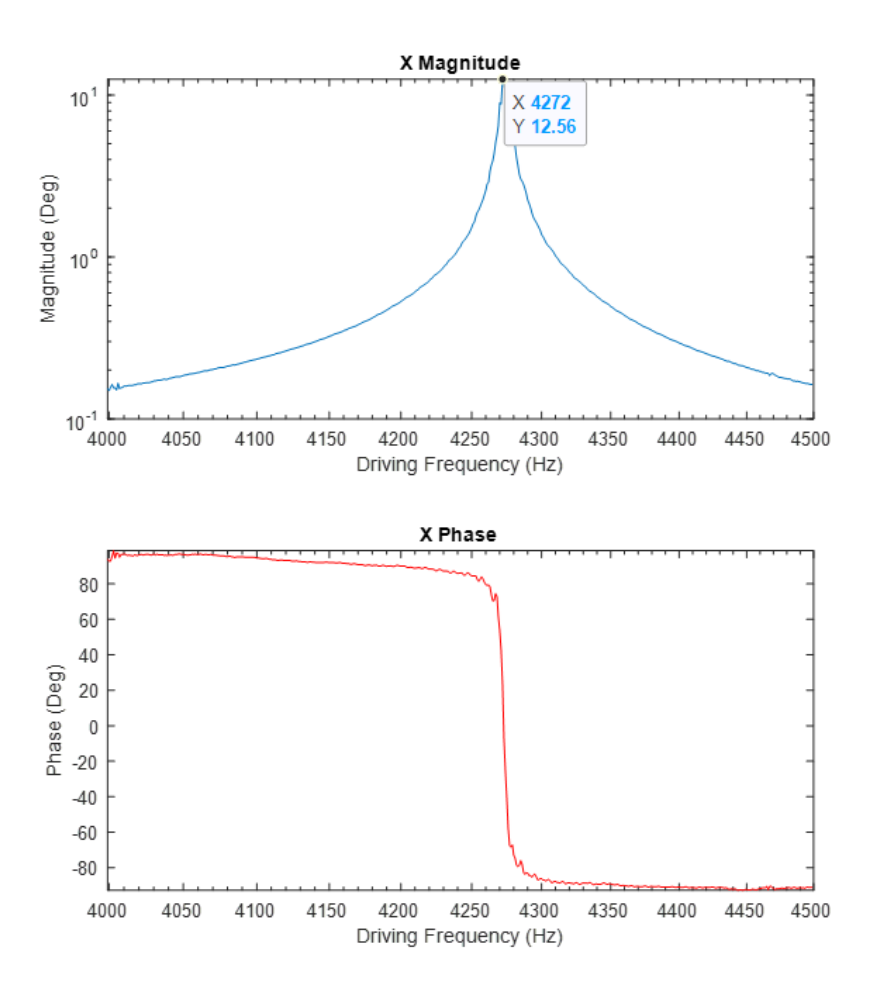


Figure 45 PZT MEMS scanner inner resonate frequency.

After the testing, the resonate frequencies for outer axis and inner axis were at 550 Hz and 4272Hz.

5.3 Superconducting Nanowire Single-Photon Detector

In traditional confocal microscope systems, people use the photomultiplier tube (PMT) [84, 85]to detect the emission photons and reconstruct it into the 2D pixel array for imaging. However, the sensitivity and quantum efficiency are limited by the detector material and hard to detect the weak light source.

To increase the designed system imaging ability, the superconducting nanowire single-photon detector (SNSPD) is a useful tool to collect the fluorescent light. The SNSPD technology has been widely used in today such as quantum information [86], quantum computing [87, 88], single

photon emitter characterization [89], on-chip quantum optics [90, 91] and LIDAR [92, 93].

The idea of the SNSPD is to form a thin film superconducting material to a meandering nanowire structure by micro-fabrication and installed into a cooling environment below its superconducting critical temperature. Due to its physical properties, the nanowire structure is extremely sensitive to the temperature changes which can be caused by the single photon absorption [94-96]. The working principle of the SNSPD is also straight forward and the workflow is showing in Figure 46 [94-100].

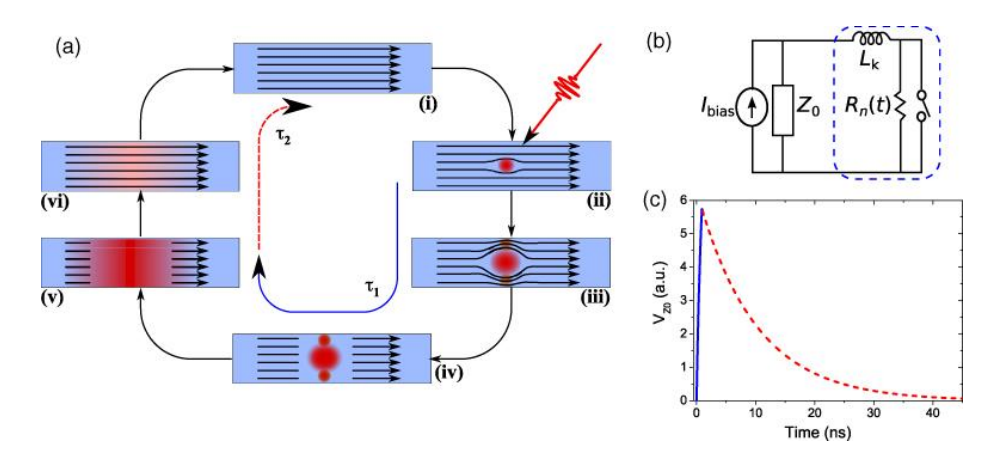


Figure 46 Basic operation workflow of SPSPD [96]. (a) An illustration for a detection cycle. (i) Nanowire at superconducting state. (ii) Single photon nanowire absorption and generate a small hotspot. (iii) The hotspot forces the current flow around the affected area, (iv) A resistive barrier generated across the full width of the nanowire channel. (v) The flowing current blocked by the high resistance nanowire. (vi) Nanowire returns to the original superconducting state. (b) The equivalent circuit of SNSPD. (c) A simulated output voltage pulse of the SNSPD. Blue and red represent the phase changes during one detection cycle.

When the nanowire is in superconducting state, a DC current is biased through the nanowire below the critical temperature. When single photon hits on the nanowire structure and absorbed by it, a small hotspot is generated. The hotspot forces the current flow around the affected area and increases the local current density. When the current density exceeds the critical current density, it creates a resistive barrier and blocks the channel. During this time, a detectable pulse voltage across the nanowire is formed and the Joule heating is built at local region. With the Joule heating

stops the local hotspot temperature drops down and returns to superconducting state

To detect the electrical behavior a simple equivalent circuit is shown in Figure 46 (b). The L_k is he kinetic inductance, $R_n(t)$ is the time dependent hotspot resistance and the I_{bias} is the biased current. The voltage across the load impedance Z_0 can be measured as the pulse output voltage [100, 101]. For the designed LR circuit, the time constant $\tau_1 = \frac{L_k}{Z_0 + R_n(t)}$, limits the rise time of the voltage pulse. By closing the switch at the right side of the circuit, the hotspot resistance can be removed this can be used to express the bias recovery time constant $\tau_2 = \frac{L_k}{Z_0}$. Once the single photon hits the nanowire, the state of the system transforms from superconducting to non-superconducting which also leads the nanowire into the insensitive time zone, dead time or reset time. The equation to calculate this time period is:

Equation 6 SNSPD dead time or reset time calculation.

$$\tau_1 + \tau_2 \approx \tau_2$$

The corresponding pulse voltage result is shown in Figure 46 (c). The critical factor to determine the dead time period is the L_k which is related to the nanowire dimension and material properties.

To image the biomedical tissue sample at NIR II wavelength, the custom-made SNSPD device (Quantum Opus, Novi, MI, USA) was selected as the detection sensor. The working temperature of the design nanowire is around 2.5K and the working wavelength center is at 1550nm. To characterize the designed sensor, the dark current which is the bias current are measured by field-programmable gate array (FPGA)-based time tagger (Time Tagger Ultra, Swabian Instrument GmbH, Stuttgart, Germany). To optimize the sensor performance, the final bias current that we tested is around 11.15µA. And the dead time of the nanowire is 40ns which the pulse sampling rate is 20MHz. To convert the pulse signal to light intensity information, we directly add up the

total pulse count in a short period and use output it as the intensity level for imaging reconstruction. For example, the NIR miniaturized confocal microscope handheld system has a sampling rate at 2MHz which leads the time period to count number of pulses to be 500ns so that the maximum count will be around 12.

5.4 NIR Miniaturized Confocal Microscope System Scanning Method

For the MEMS scanner device, when the driving voltage frequency reaches to the resonate frequency the scanning range can be maximized. By driving both axes of the MEMS at resonate not only increase the FOV but also form a special scanning method, Lissajous scanning. The Lissajous scanning can be created by using two sinusoidal waveforms varies with the frequency and phase shown below:

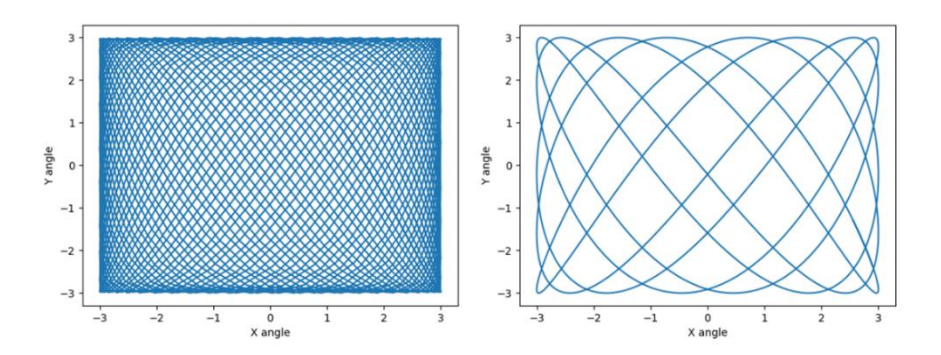
Equation 7Lissajous scanning equation.

$$\begin{cases} V_x(t) = Asin(2\pi f_x + \varphi_x) \\ V_y(t) = Bsin(2\pi f_y + \varphi_y) \end{cases}$$

Where the A is the amplitude of the driving voltage in x axis, f_x is the resonate frequency in x axis and φ_x is the phase. B is the amplitude of the driving voltage in y axis, f_y is the resonate frequency in y axis and φ_y is the phase.

For real time imaging, the frame rate (FPS) is the dependent on the greatest common divisor (GCD) of the two inputs frequency. In our system, the designed PZT MEMS has a fast axis frequency at 4328Hz and slow axis frequency 828Hz, so the FPS is 4.

Even the Lissajous scanning pattern can generate a fast-imaging speed and large field view, the selection of the input frequency is also critical which affects the dead pixel area. For example, in Figure 47, two different Lissajous scanning patterns are generated by MATLAB with different frequency combination



<u>Figure 47 Lissajous scanning pattern with different frequency.</u> (a) The simulation frequency is at 30Hz and 20Hz. (b) The simulation frequency is at 3Hz and 2Hz.

In the left image, the simulated frequency is at 30 and 20Hz which leads a high line density pattern. In the right image, the frequency is 10 times less than the first simulation which leads the line density lower with lots of blank area. During the imaging reconstruction, the collected data points are filled back to the x by y pixel array, so that the line density directly effects the filling factors. With lower frequency, many area can not be filled with the signal data which causes dead pixel.

5.5 System Schematic and Assembly

To reduce the system size, all optical components are integrated on a 3D printed mount. The schematic and Solidworks model image is shown in Figure 48.

For the fluorescence excitation, a 785nm 125mW laser is used as light source. A SMF is connected to the laser engine and the light is collimated by a lens (84-128 Edmund Optics, USA) into a 1mm beam. The collimated beam is reflected by dichroic mirror (FF925-Di01-25x36, Semrock, USA). Next, the 1mm beam is coupled into the commercial collimator for 1310nm wavelength and delivered by another SMF. The SMF is connected to another SMF based collimator (GT-Achr-980-SM900-1, GRIN TECH, GmbH, Germany) shown in Figure 49 and installed in the customized 3D printed holder. And then, the PZT MEMS scanner is placed 45° at the end of the holder to reflect beam 90°. Another 2 lenses (LA1024-B, Thorlabs, USA) are used to form a *f*-

theta lens pair to provide the highest performance in lasering scanning. The imaging sample is place 15mm away from the *f-theta* lens pair for real time NIR II confocal imaging. For the collection side, the emission light transmitted back to the SMF based collimator to form the confocal effect. The emission light is greater then 1000nm wavelength and can be passed through the dichroic mirror. Finally, the emission light is coupled into another SMF to match the SNSPD fiber core size for photon detection.

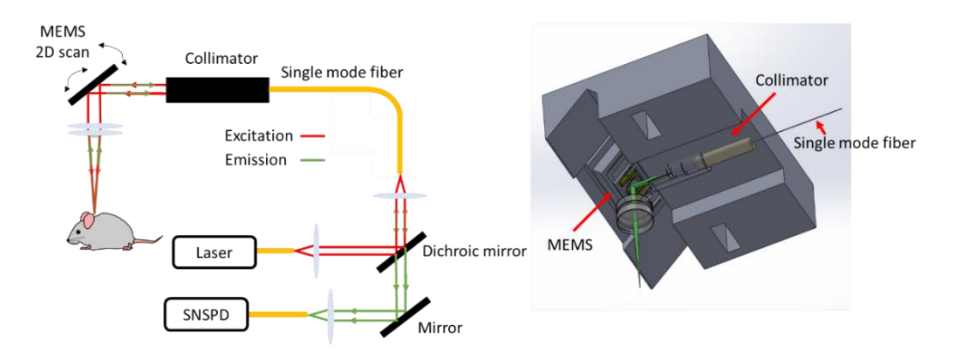


Figure 48 Miniaturized confocal microscope handheld system schematic and 3D drawing. (a) The red line is the excitation light path, and the green line is the emission light collection path. (b) Solidworks drawing and assembling of the designed handheld system.



Figure 49 4mm diameter collimator GT-Achr-980-SM900.

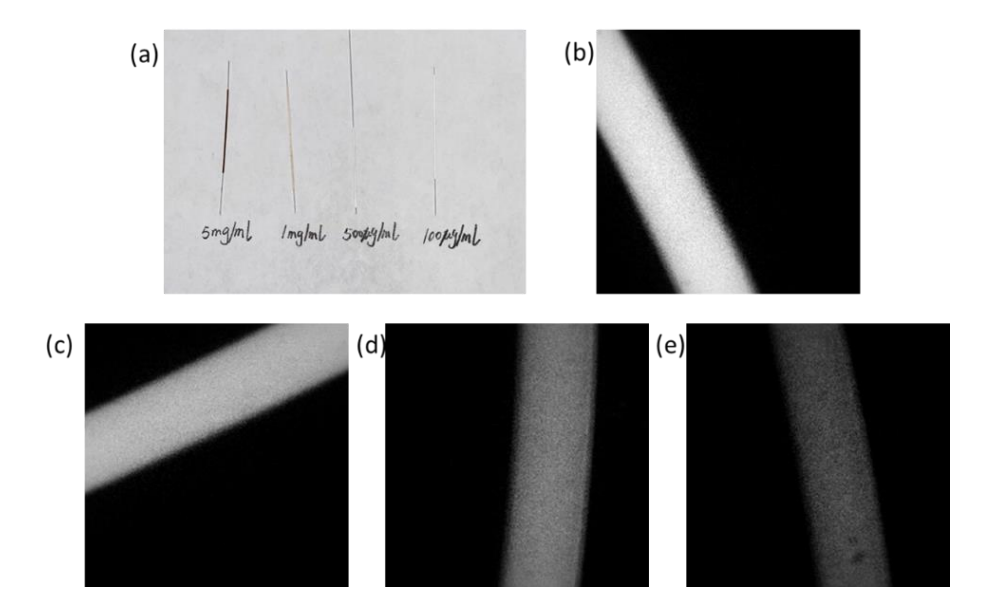
The assembled system photo and Lissajous scanning pattern test image is shown in Figure 50.



<u>Figure 50 Photo of the designed handheld system and scanning pattern.</u> (a) MOEMS based NIR confocal microscope handheld system photo. (b) The PZT MEMS scanning pattern for Lissajous scanning.

5.6 NIR II Confocal Microscope Handheld System Imaging Characterization

To test the designed system can be used for NIR II wavelength depth tissue imaging, a group of fluorescence phantom samples were imaged and shown in Figure 51.



<u>Figure 51 NIR II phantom imaging result.</u> (a) 4 different QD phantom in the capillary tubes. (b) Phantom concentration 5mg/ml. (c) Phantom concentration 1mg/ml. (d) Phantom concentration 500 μ g/ml. (e) Phantom concentration 100 μ g/ml.Tube OD 360 μ m.

During the phantom imaging, the output laser power from the handheld system is about 9.3mW. The phantom samples placed on a xyz axis stage to find the best focal plane of the designed system. To have the Lissajous scanning pattern, the MEMS driving frequency was set to the resonate frequency. To control the scanning range, the amplitude of the driving voltages was also optimized with is inner axis (fast) 0~4V and outer axis (slow) 0~1.2V, shown in Figure 52.

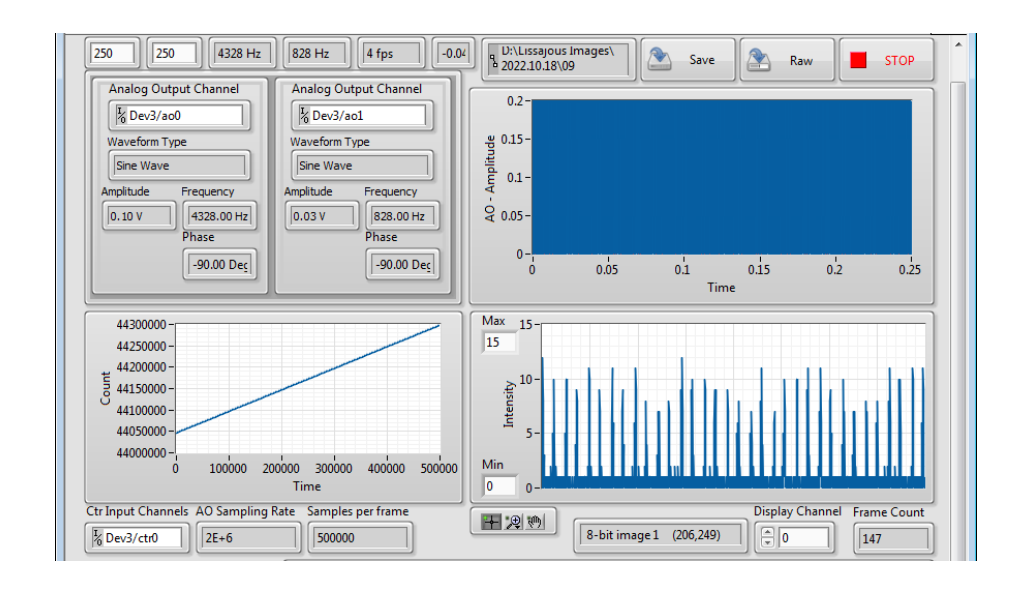


Figure 52 NIR II imaging LabView UI and parameter setting.

To optimize imaging resolution, the number of pixels was set to 250x250. At the lower right bottom in Figure 52 it shows the SNSPD pulse counting level, like the calculation in the last section, the level range is from 0 to 15 which can cover the full range of the maximum pulse output.

5.7 NIR II Confocal Microscope Deep Tissue Imaging

The advantage of imaging at NIR II wavelength is to reduce the light scattering and tissue absorption effect. Many researchers are using these optical properties to image the mouse brain vessel net without removing the skull and scalp. For our handheld system, the emission peak is selected at 1550nm which can easily satisfy the deep tissue imaging requirements. In Figure 53, it shows the result of the phantom tube covered by different thickness of mouse brain slides

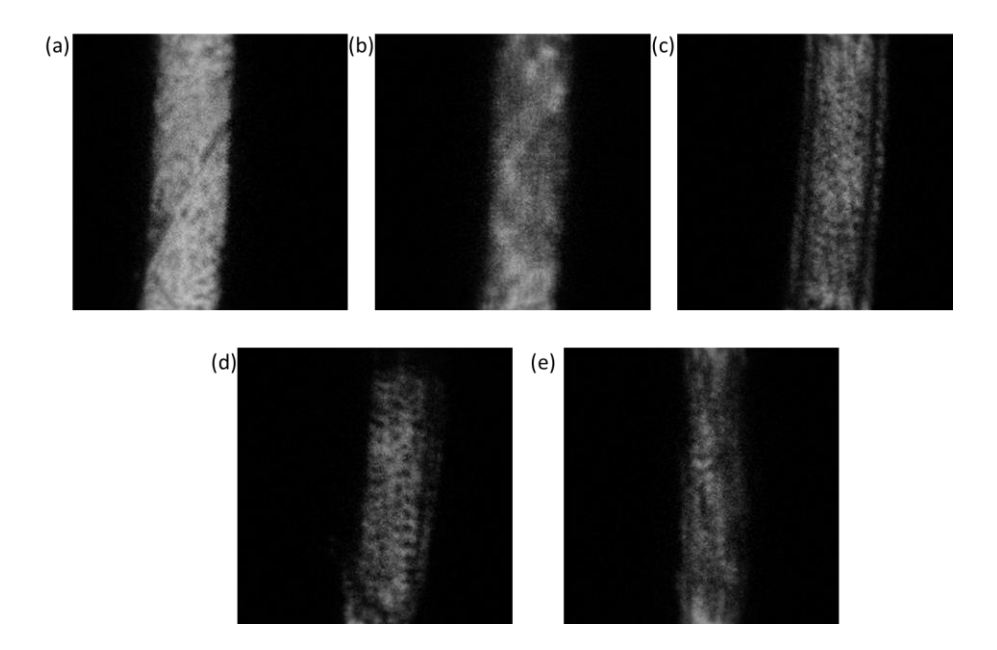


Figure 53 Phantom tube with different thickness brain slides covered for NIR II imaging. (a) Brain slide thickness 50μm. (b) Brain slide thickness 100μm. (c) Brain slide thickness 150μm. (d) Brain slide thickness 200μm. (e) Brain slide thickness 300μm. Phantom concentration is 5mg/ml.

As a result, even the phantom tube was covered by different thickness of the brain slides, the images showed a great contrast and clear features which identifies the ability of the designed system for deep tissue imaging.

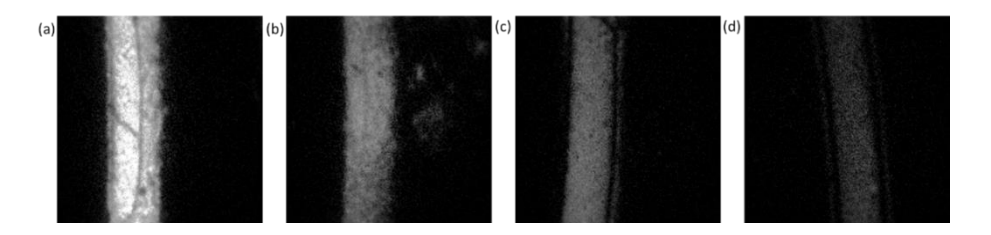


Figure 54 Mouse skull phantom tube imaging result. (a) 5mg/ml tube under mouse skull. (b) 1mg/ml tube under mouse skull. (c) 500μg/ml tube under mouse skull. (d) 100μg/ml tube under mouse skull.

To prove that the designed system can be used for non-invasive mouse brain vessel imaging, a fresh mouse skull was harvested and used to cover the phantom tubes. Also, to optimize the concentration of the fluorescence dye for future *in vivo* experiments, different concentrations phantom tubes were imaged under the same thickness mouse skull shown in Figure 54.

From the imaging result, even the concentration of the phantom has been diluted to 100x less than the standard injection limitation, the emission light signal can still be detected by the SNSPD and reconstructed to the 2D image. Meanwhile, the small features of the skull sample are also collected by the system due to the light intensity difference and projected to the detector sensor.

5.8 NIR II Confocal Microscope Brian Tissue Imaging

After test the designed confocal microscope system by phantom tubes, an *ex vivo* mouse brain tissue was imaged shown in Figure 55. To prepare the tissue sample, the fresh mouse brain was harvested from the normal mouse after dissection and fixed by 4% PFA solution for over 48hrs [18, 38, 39]. The fixed brain sample was merged into the 30% sucrose solution to prevent the tissue damage during frozen cutting for 12hrs [102, 103]. After that, the whole mouse brain was mounted to the Leica microtome machine and frozen to -20°C for thin slide cutting. There are 3 different thickness brain slides (50, 150 and 200μm) prepared for QD topical staining at different concentration (500μg/ml, 1mg/ml and 5mg/ml). The brain imaging result is shown in Figure 55.

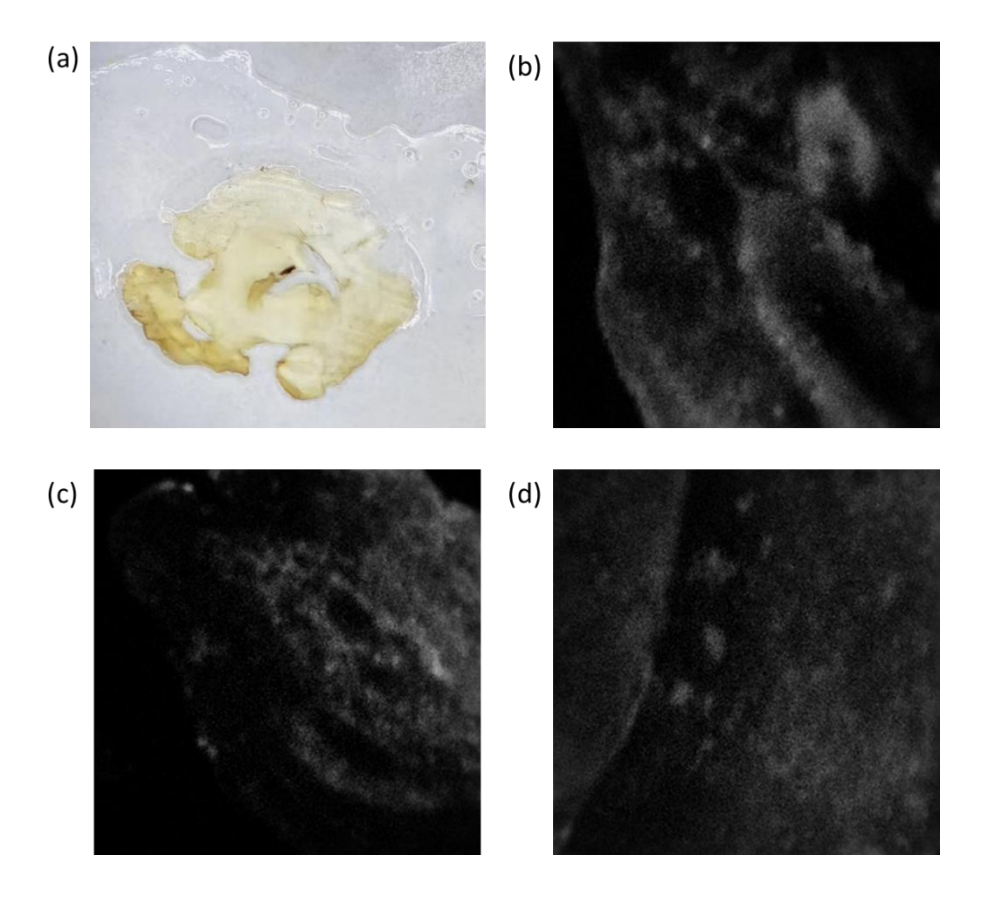


Figure 55 Brain tissue imaging result. (a) A photo of the prepared brain slides at 200 μ m thickness. (b) NIR II confocal imaging for 5mg/ml staining for 200 μ m brain slides. (c) 1mg/ml staining brain slide at 150 μ m thickness. (d) 500 μ g/ml staining brain slide at 50 μ m thickness.

5.9 MOEMS Based Miniaturized NIR Confocal Microscope Handheld System Conclusion

In this chapter, we have successfully proofed the concept of the miniaturized confocal microscope handheld system and demonstrated the imaging abilities. Compared to the traditional single axis confocal microscope system, the new design dramatically reduces the size and keep the high optical resolution. Meanwhile, using the Lissajous scanning method, the imaging FOV and PFS have been increased which is used for non-invasive biomedical imaging and imaging guidance surgery. For the fluorescence imaging, at NIR II wavelength, the light penetration can be extended such as under skull vessel imaging. In the future experiment, the handheld system could be used to monitoring mouse brain vessel activities.

CHAPTER 6: MOEMS AND MIRCO-RING BASED ORPAM

6.1 Introduction to Optical Resolution Photoacoustic Microscope

Optical resolution photoacoustic microscopy (ORPAM) has become to a popular topic in recent years due to its unique properties. Compared to the fluorescence imaging, ORPAM is a label-free imaging system that widely used in non-invasive biomedical tissue imaging study such as oncology [104], neuroscience [105], label-free histology [106] and cardiology [107], etc. The image information is provided by the sample thermoacoustic effect which generates acoustic wave and detected by the ultrasonic sensor. The data that collected by the scanning OR-PAM system not only provides the 2D lateral resolution [108] but also contains the axial resolution information which can be used to create 3D modeling due to the acoustic wave properties.

In this chapter, we demonstrate a miniaturized system by using the MOEMS and micro-ring sensor to construct a handheld photoacoustic probe. Compared to the traditional ORPAM system which using the single axis confocal microscopy as basic optical structure, the new designed system has a more compact size. The micro-ring sensors (MRRs) [109] are provided by our collaborator Dr. Cheng Sun from Northwestern University. In the pervious study such as Dr. Lihong Wang's group, the ultrasound signals are commonly collected by the transducer or hydrophone sensor. However, the size of the senor makes the whole imaging system bulky and require precise optical alignment. On the contrast, the MRRs is a flat transparent sensor which can be easily integrated into the handheld system.

6.2 First Generation OR-PAM Tabletop System

The schematic of the OR-PAM imaging setup is shown in Figure 56. A 532nm pulsed laser with a pulse duration of <10ns and repetition rate of 1kHz was used as the excitation source. The laser beam was travelled in free space and reflected by 2 mirrors to adjust the center position. After

the beam was centered a beam expander L1 and L2 lenses pair, the beam was used to expand to 4mm diameter. Then we used another lens to couple the laser beam into a (SMF) which can be easily delivered to the microscope side. On the other side of the SFM, it was attached on a customized collimator to pass the light into free space. Next, the beam was expanded again to fit the back aperture of the 10x objective lens. A hydrophone detector was placed next to the objective lens and pointed to the focal point to collect the ultrasound signals. To mount the imaging samples, a small water tank was placed on the Voice Coil 2D stage. During the imaging, the hydrophone and sample were both merged into the water to prevent ultrasound decreasing.

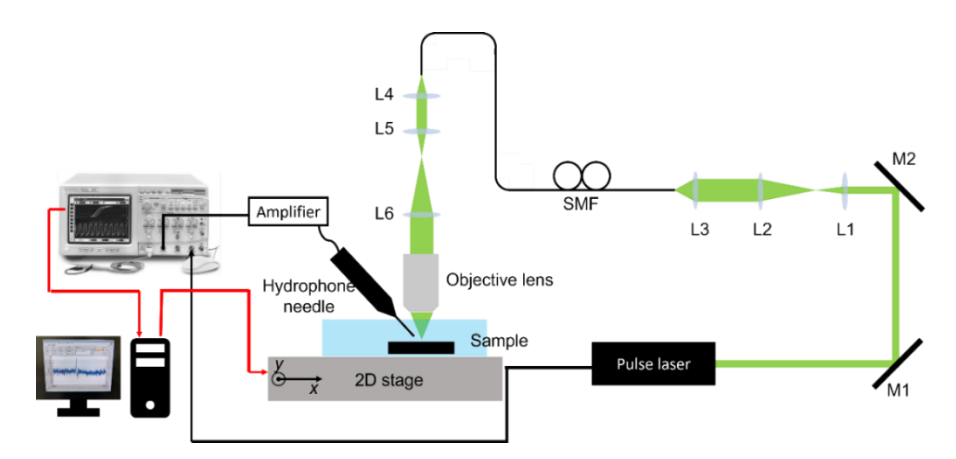


Figure 56 The schematic of the OR-PAM tabletop. A 532nm ns pulse laser generates the excitation light source, the TTL of the pulse signal is sent to the DAQ card for scanning synchronization. The free space beam is coupled into a single mode fiber and connect to the microscope side. To fit the back aperture of the 10x objective lens, another beam expander is used. For ultrasound signal collection, a hydrophone is placed next to the beam focusing spot. For scanning imaging, the 2D voice coil stage is used to carry a water tank and achieve the 2D scanning. The prepared phantom or tissue sample are merged into the water to prevent the ultrasound signal losses.

6.3 Scanning Method and Data Acquisitions

For OR-PAM imaging, the scanning method is different to the fluorescence imaging such as confocal microscope. The imaging speed is no longer limited by sampling rate but by the laser repetition rate. For our system, the 532nm pulse laser has a repetition rate from 1kHz to 25kHz

which is slower than the MOEMS confocal microscope system 2MHz sampling rate. In this case, the Lissajous scanning is not the ideal pattern to collect the ultrasound data. Here, we present a raster scanning mode to acquire the continuous ultrasound signals. To balance the image pixel size and the total scanning time, the laser repetition rate is the critical factor in this experiment.

To calculate the OR-PAM scanning time and reconstructed image pixel size, a set of equation is shown below:

Equation 8 OR-PAM scanning time and pixel number calculations.

$$\begin{cases} T_{total} = \frac{1}{f_y} \\ Pixel_y = \frac{2 \times Peroid_y}{Peroid_x} = \frac{2 \times f_x}{f_y} \\ Pixel_x = \frac{Peroid_x}{2 \times T_{rr} \times ave} = \frac{f_{rr}}{2 \times f_x \times ave} \end{cases}$$

Where the T_{total} is the total scanning time. f_y is the y axis scanning frequency and f_x is the x axis scanning frequency. f_{rr} is the laser repetition rate. ave is the acquisition average number.

6.3.1 Digital Mode Scanning

For the digital mode the schematic is shown in Figure 57. The laser control box generated the trigger signal for both laser head, oscilloscope and computer board. After the trigger signals have been detected, the PI QuickScan control box will apply the voltages on the 2D stage to control the *x* and *y* axis. At the meantime, the oscilloscope will start acquiring data once the stage moved to the desired position.

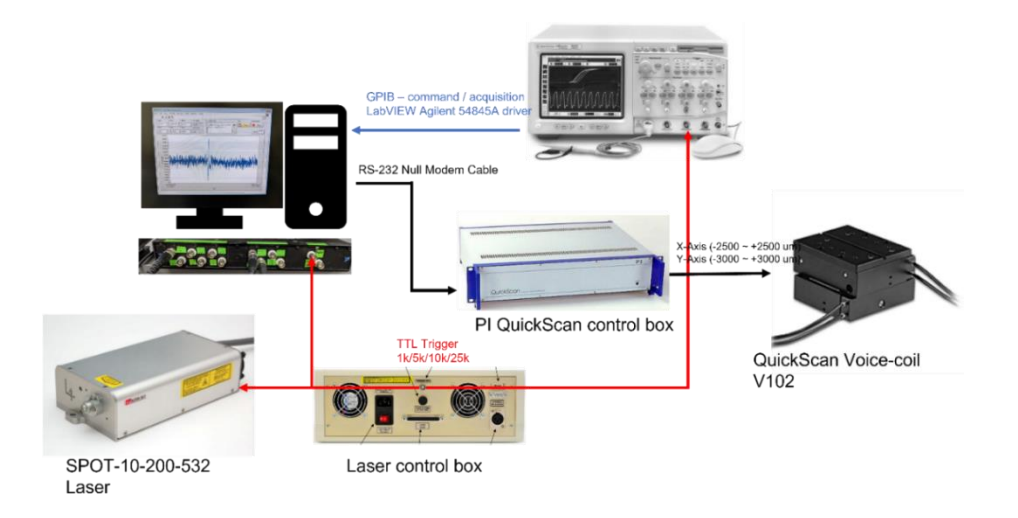


Figure 57 The schematic of the digital scanning mode.

During the data acquisition, an average algorithm is applied to the signal collection which to reduce the AC noise level. However, increasing the average number will also increases the PA sample scanning time. Another issue while we increase the average number is that during the imaging reconstruction processing the along the fast-scanning axis the odd row and even row pixels will have a mismatching effect. The main reason causes this issue is that during the collecting the PA signal, the stage is still moving to its next location (shown in Figure 57). To proof our thoughts, we applied 2 different digital scanning pattern, bidirectional scanning and unidirectional scanning (shown in Figure 58). For the bidirectional scanning pattern, the stage is moving as a zigzag shape. During the forward and backward scanning, all PA signals are collected. On the contrast, the unidirectional scanning, the PA signal will be only collected during the slowing moving period and after that the stage will fast shift back to the origin positions for another row pixel scanning.

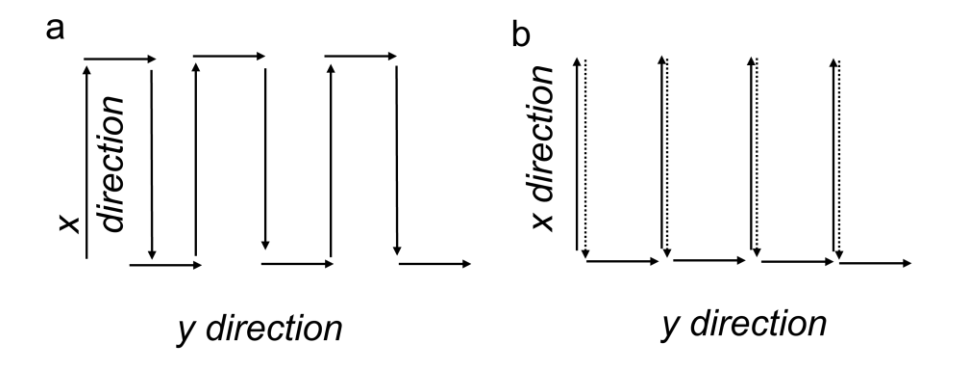


Figure 58 Digital scanning modes. (a) Bidirectional. (b) unidirectional.

6.3.2 Analog Mode Scanning

Even the digital mode scanning can provide us a good, reconstructed PAM image, however, the discrete scanning compared to the continue scanning is more time consuming. To achieve a larger area imaging scanning, we applied an analog mode scanning to the PAM system shown in Figure 59.

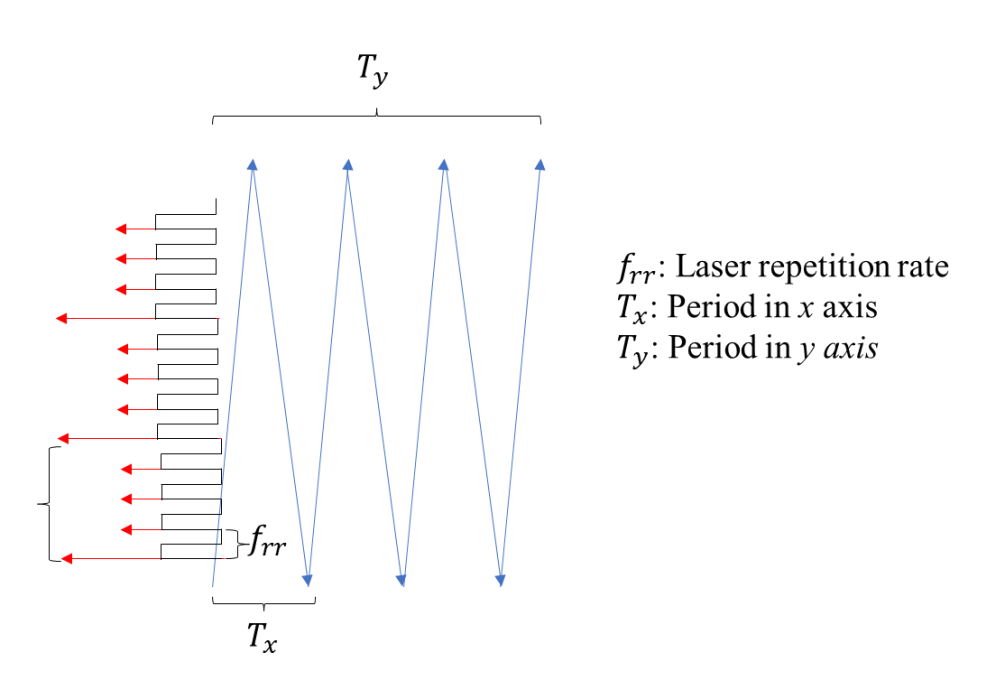
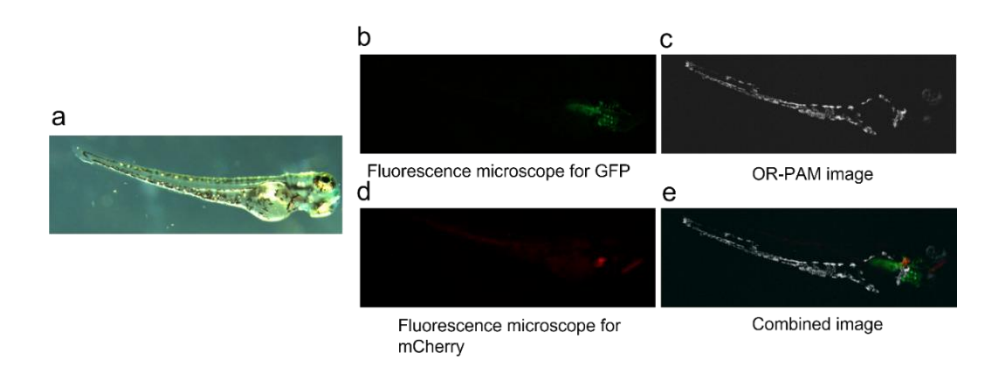


Figure 59 Analog scanning schematic.

6.4 OR-PAM Tabletop In Vivo Imaging

To test the imaging quality of the analog mode scanning, zebra fish embryo was selected as the imaging target. The transgenic fluorescent mCherry and GFP modified zebra fish embryos were incubated in a 28.8°C incubator for 7 days. The healthy embryo was transfer on a 0.5% agarose-based mount bed at room temperature. The bright field image of the embryo is shown in Figure 60



<u>Figure 60 OR-PAM tabletop zebra fish in vivo imaging.</u> (a) The photo of the zebra fish embryo. (b) The fluorescence microscope imaging for GFP channel. (c) OR-PAM imaging for zebra fish melanin. (d) The fluorescence microscope imaging for mCherry channel. (e) The reconstructed 3 channel imaging.

In Figure 60 (b) and d, it shows the fluorescent images of the embryo captured by the Lecia stereo microscope. The strongest signals are coming from the heart region which satisfies the transgenic method. In Figure 60 (c), the fish melanin is captured and located at low location of the fish body. And in Figure 60 (e), three channels combined image shows all the detail information of the fish embryo.

6.5 MRRs Based OR-PAM System

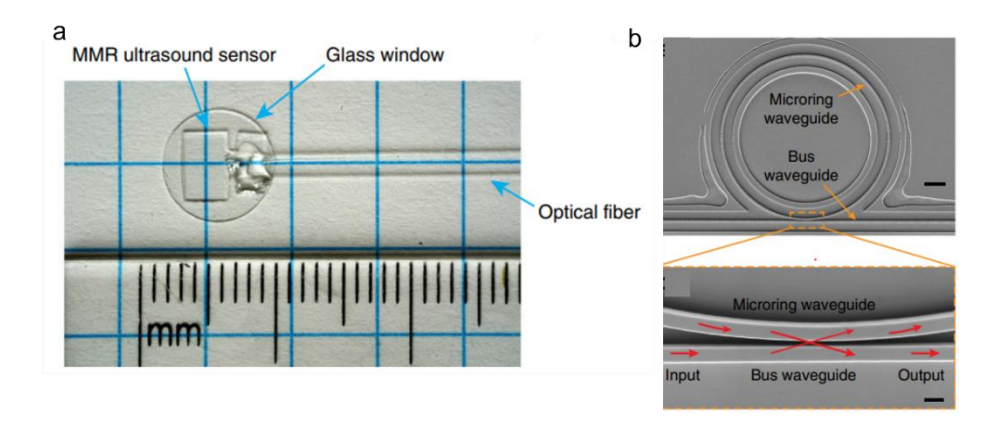
6.5.1 MRRs Introduction

With the development of the OR-PAM system, more and more researchers begin to focus building the miniaturized system such as portable OR-PAM, handheld probe and endoscope system. One of key component in the OR-PAM system is the transducer sensor. The traditional

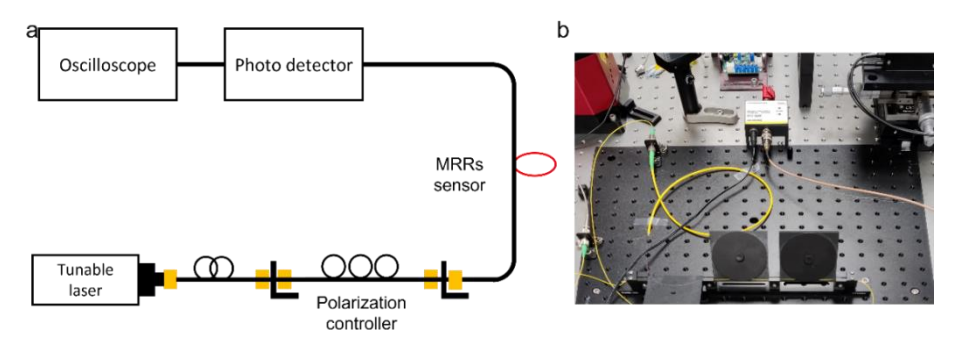
ultrasound transducers usually have bulky size, on the contrast, recently people are likely to start the study of optical fiber-based ultrasound sensor, such as micro-ring resonator [110-112]. This new optical fiber-based sensors not only have a smaller physical size but also have a larger working bandwidth[113]. Another advantage of this sensor is that the whole device is fabricated on a quartz slide and the inner structure is transparent which can be used for multimodality optical imaging, the MRRs sensor will not create a light scattering or absorption.

In this section, we demonstrate a system which combines the fiber-based micro-ring resonator sensor with PAM. We received the fully fabricated micro-ring resonator sensor from Northwestern University and integrated with our customized PAM system.

In Figure 61 (a), it shows a photo of the micro-rings resonator (MRR). There are two major components inside the MRRs sensor: MRRs waveguide and bus waveguide shows in Figure 61 (b). For the ultrasound detection, the MRRs uses the optical way to sense the signals. To optimize the best performance of the MRRs sensor, it needs to set the driving light source at the local resonate wavelength. A customized optical driving circuit is designed and shown in Figure 62. A tunable laser source (TLB-6172, Newport, USA) is used to find the MRRs resonate wavelength. The laser range is from 765~781nm with 150pm step size. The free space laser is coupled into the SMF and connected to the polarization controller to change the fiber polarization. After that a mechanical splice connects the SMF and the MRRs input SMF. When the resonate wavelength of the MRRs is located, the sensor is place above the ultrasound source. The tiny ultrasound vibration will change the MRRs local resonate and affect the light intensity which passes through the waveguide. An avalanche photodiode is used to collect the light intensity varieties and converts to voltage changes. Finally, the ultrasound information is collected by the DAQ card or an oscilloscope and formed into 2D PAM images.



<u>Figure 61 Micro-ring resonator sensor.</u> (a) a photo of the real MRR sensor. (b) The SEM image of the micro-ring inner structure [113].



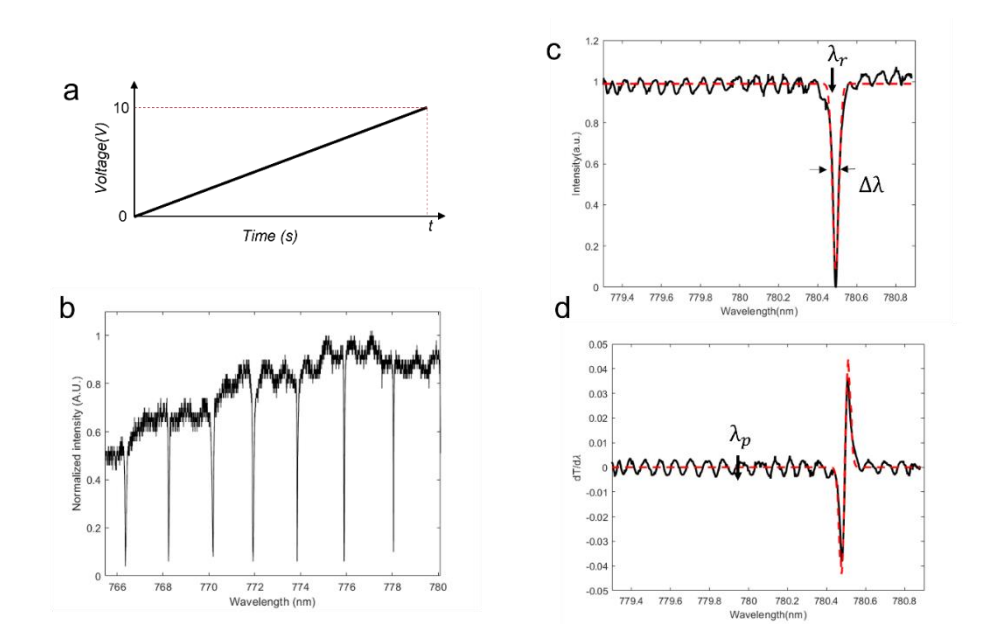
<u>Figure 62 MRRs driving optical design.</u>(a) The schematic of the designed optical driving circuit. The tunable laser is used to find the MRRs local resonate, and the polarization controller is used to change the fiber polarization. The photodetector detects the light intensity changes during the ultrasound hits the micro-ring structure and converts to the analog voltage. The voltage signal is collected by the oscilloscope and used to reconstruct into 2D images. (b) The photo of the customized MRRs driving circuit.

To find the local resonate of the MRRs sensor, a full wavelength scanning is created by the tunable laser shown in Figure 63 (a). During the tunable laser sweeping the full wavelength, the MRRs spectrum information was detected by the oscilloscope shown in Figure 63 (b). After we located the sharpest resonance, we did a small range wavelength sweeping around resonance to capture the detail information (Figure 63 (c)). The center resonance of this device is about 780.45nm and the Q factor which determine the sensitivity of the device can be calculated by:

Equation 9 MRRs Q factor calculation

$$Q = \frac{\lambda_r}{\Delta \lambda}$$

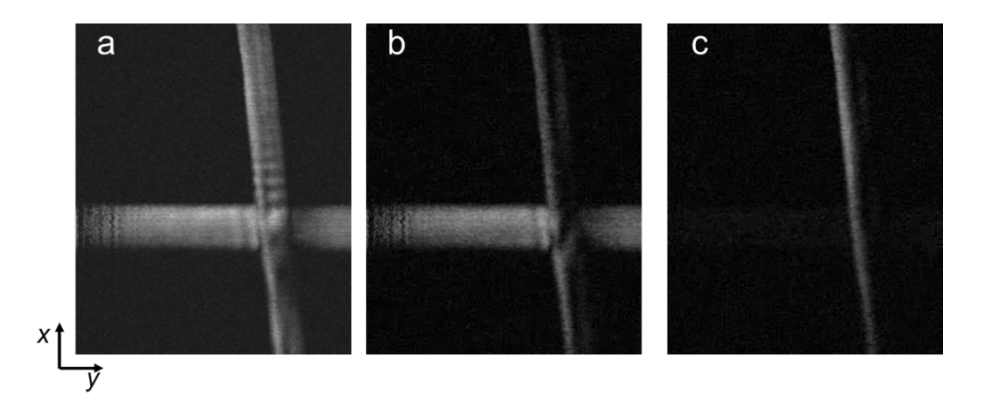
Where the $\Delta\lambda$ is the FWHM of the fitting Gaussian curve about 55.6pm, and λ_r is the center wavelength resonance. The Q factor of this device is about 14036.87.



<u>Figure 63 The characterization measurement of the MRRs.</u> (a) The sweep voltage input for tunable laser. (b) MRRs full resonance spectrum of MRRs. (c) Transmission spectrum shows the dip caused by the strong WGM-induced optical resonance. (d) transmission change with respect to the resonance shift derived by the first derivative of the transmission spectrum.

6.6 OR-PAM Tabletop with MRRs phantom Imaging

To test the imaging quality of the MRRs sensor based OR-PAM, the hair target was place inside the water on the 2D stage as the previous traditional OR-PAM setup. In figure 64, it is the MRRs PAM scanning result, the FOV is $1000\mu m \times 1100\mu m$ and step size $5\mu m$.



<u>Figure 64 MRRs based OR-PAM tabletop phantom imaging result.</u> (a) Two hair is place in an orthogonal position. (b) The lower layer of the hair image. (c) The top layer hair image.

The fluorescence signals can be directly detected by the photo detector and convert into the digital pixel intensity value. However, the photoacoustic signal is a 2D signal which measures the depth of the sample. In each single PA signals, we can convert the amplitude of the signal and map it into pixel intensities along the time domain. Using the time information and the sound speed, the distance information can be calculated. Instead of 3D scanning like confocal microscope imaging, to reconstruct the 3D sample structure a 2D scanning is enough to collect the three-dimensional information shown in Figure 64 (b) and (c).

6.7 MOEMS and MRRs Based Miniaturized OR-PAM Handheld System

To reduce the system size and make the imaging system portable for biomedical imaging, here we present our MOEMS and MRRs based OR-PAM handheld system. A thin-film PZT MEMS scanner is used to achieve the beam scanning. However due to the current device which the resonate frequency for the inner axis is too fast to the laser repetition rate, we only use the outer axis in the DC scanning mode. For the other scanning axis, the handheld system is placed on a single axis voice coil stage and moving orthogonally to the inner axis, shown in Figure 65.

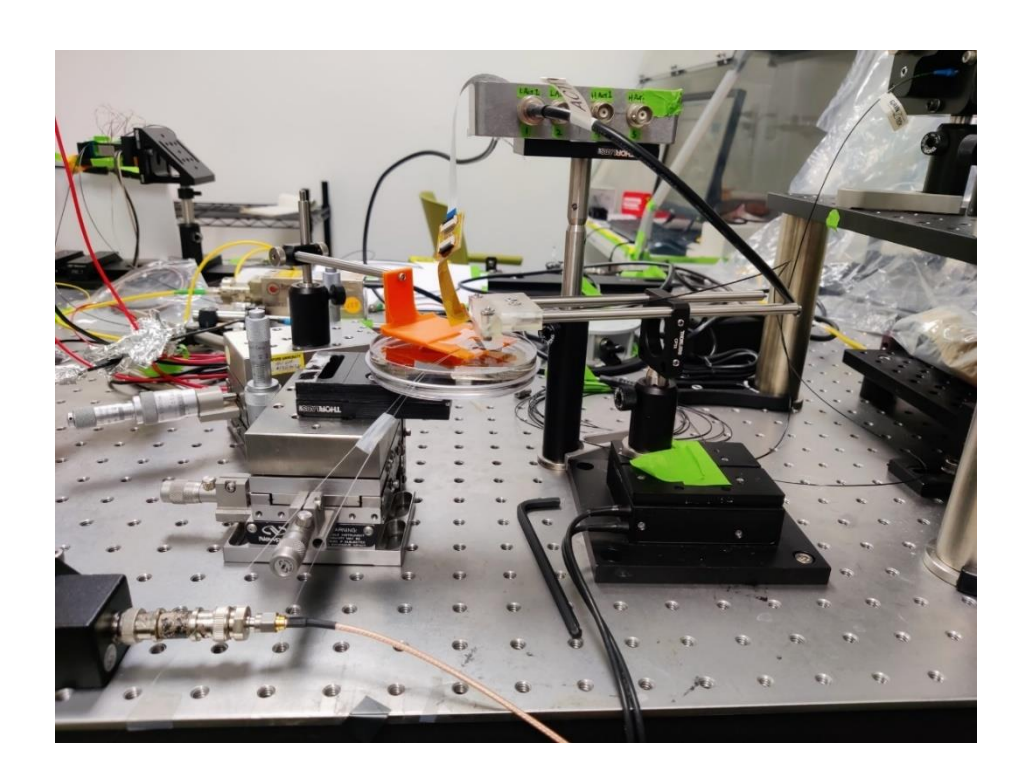


Figure 65 MOEMS and MRRs based OR-PAM handheld system photo.

The MRRs sensor is mounted on another 3-axis stage to find the best ultrasound collection position. Due to the property of the designed MRRs, the excitation laser light can easily penetrate the quartz substrate and focused on the sample surface to generate the ultrasound signals.

To test the FOV of the designed system, the USAF Cr coated target is placed under the water at the laser focal plane. During the scanning, the ultrasound signal is collected by the MRRs and reconstructed into a 2D image, shown in Figure 66.

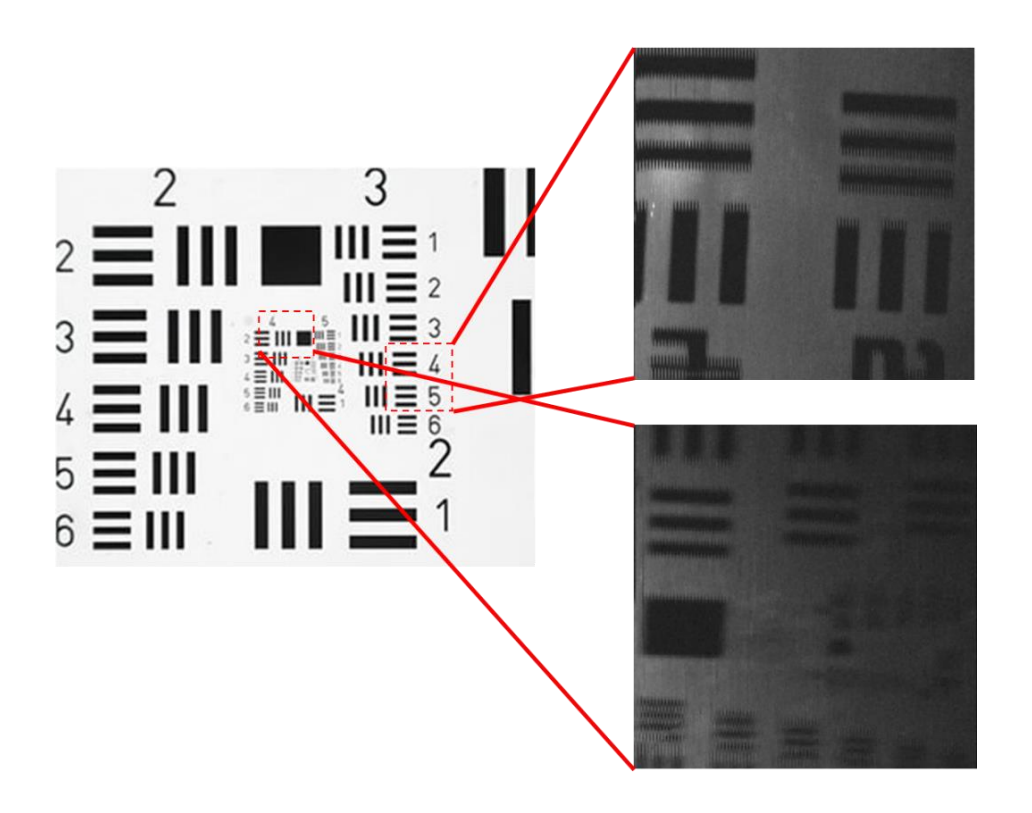


Figure 66 MOEMS and MRRs OR-PAM FOV result.

To drive the MEMS scanner outer axis, a triangle wave with amplitude $0\sim20\mathrm{V}$ voltage generated by the DAQ card. For the single axis voice coil stage, the driving voltage is $0\sim0.5\mathrm{V}$ and the waveform is sawtooth wave for one time scanning. For the result, the image pixel size is 200x200 and the FOV is calculated by the real USAF dimension which is $618x556\mu\mathrm{m}$.

6.8 MOEMS and MRRs OR-PAM Handheld System Phantom Imaging

To detect the designed system imaging performance, a set of phantom imaging experiments are created. The imaging result is shown in Figure 67. The 7.5µm diameter carbon fiber sample are fixed on a glass slide and place at the laser focal plane, shown in Figure 67 (a). For the imaging location testing, the MEMS scanner and voice coil were driven by a lower amplitude compared to the FOV measurement. A 0~20V voltage is applied to the MEMS scanner and a 0~0.5V voltage is applied to voice coil stage. After the scanning location a higher resolution imaging is collected by reducing the scanning area which allows more ultrasound signals can be collected in a small region,

shown in Figure 67 (b). Finally, the orthogonal hair sample is imaged by the designed system, shown in Figure 67 (c).

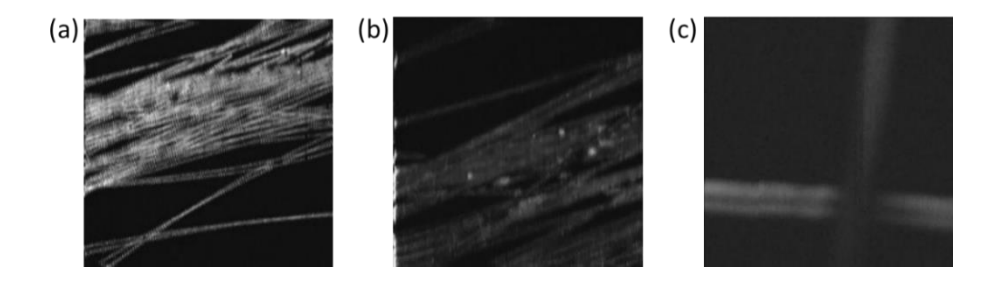


Figure 67 MOEMS and MRRs OR-PAM handheld system phantom images. (a) A large FOV carbon fiber phantom imaging result, the total FOV is 618x556μm. (b) Higher resolution carbon fiber imaging result. By reducing the driving voltage for both MEMS scanner and voice coil stage the total FOV is half of the first image. (c) Orthogonal hair phantom imaging. The FOV is 618x556μm.

6.9 MOEMS and MRRs OR-PAM Conclusion

In this chapter, we successfully demonstrated the customized MOEMS and MRRs based OR-PAM handheld system. The MEMS scanner and micro-rings senor significantly reduce the system size and keep the high-resolution photoacoustic images. However, the MEMS resonate frequency limits the inner axis scanning ability which is too fast for the ns pulse laser. To solve this problem, we used a single axis voice coil stage to achieve one direction scanning. In the future, with the new MEMS device which can provide both axis DC driving the system size can be more compact. By having this imaging system, it can be a great tool for biomedical imaging for both *ex vivo* and *in vivo* study.

CHAPTER 7: METALENS BASED ORPAM

7.1 System Introduction

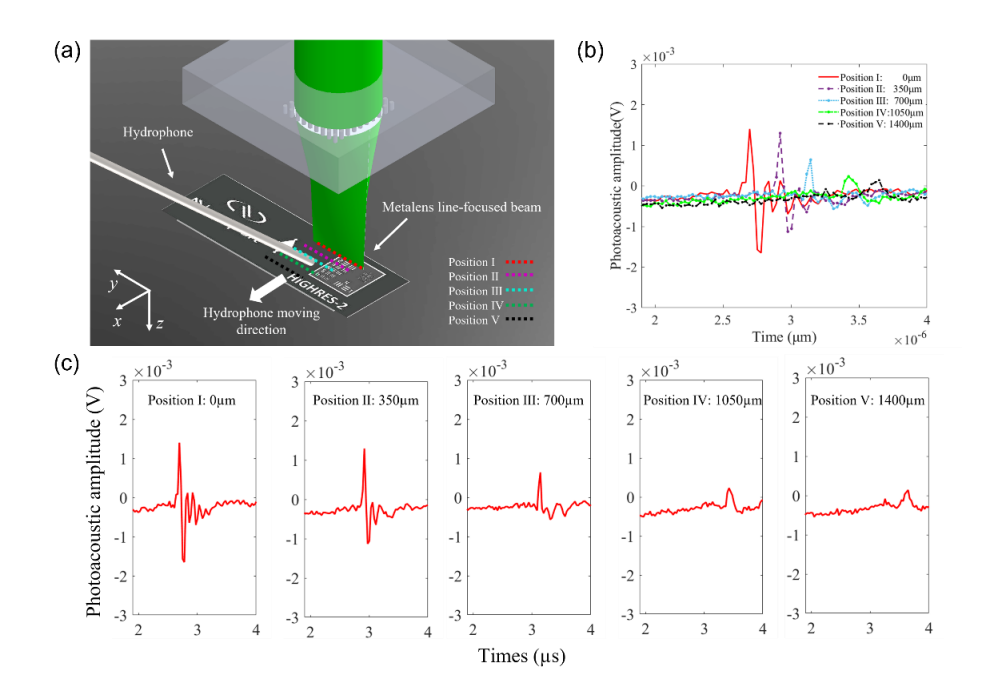
In the last chapter, we have demonstrated the MOEMS and MRRs based OR-PAM handheld system. The designed system size has been dramatically reduced compared to the traditional photoacoustic system. However, with the great development of the metalens study, this new nano technology lens can replace the traditional optical lens and make the designed system more compact.

For the photoacoustic microscope system, the image information is provided by the sample thermoacoustic effect which generates acoustic wave and detected by the ultrasonic sensor. For each scanning, the OR-PAM not only provides the high-resolution imaging result [108, 114, 115] but also contain the axial resolution information for 3D modeling due to the ultrasonic wave properties [116]. However, currently the OR-PAM systems are designed by using the combination of the traditional lenses to achieve beam focusing. To have a miniaturized or handheld imaging system, the key factor is to reduce the optics size such as using GRIN lens and MEMS scanner. Metalens is an emerging modality which has a more compact physical size and shows a great potential in miniaturized imaging system design. In this chapter, we are demonstrating a photoacoustic microscope system by using a line focused metalens at visible range for imaging.

7.2 System Schematic and Design

To demonstrate the designed metalens can be used to excite the acoustic signal, a simple photoacoustic experiment was setup in Figure 68 (a). A 532nm short pulse optical laser (SPOT-10-100-532, Elforlight Ltd, UK) was selected as excitation source. The free space collimated beam size is about 2mm which fully cover the designed metalens effective area. A Cr coated USAF target was placed inside the water tank and at the metalens focal plane. A hydrophone needle was

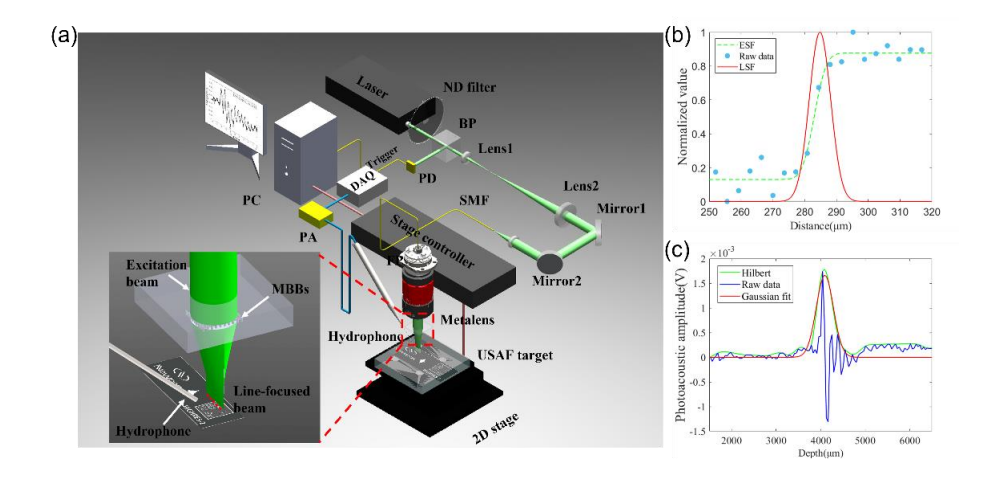
mounted on a 1D stage and pointed to the line-focused beam. The hydrophone position can be manually adjusted along the *x* axis during the experiment and the photoacoustic signal behavior tendencies were directly recoded by the oscilloscope, shown in Figure 68 (b). First, the hydrophone was mounted close to line-focused beam till the maximum photoacoustic signal was reached and the position was set as position I. During the experiment, the hydrophone was manually moved away from the line-focused beam by step size 350μm. In Figure 68 (c), at each position, the time point which the photoacoustic signal was detected by hydrophone was delayed. At the meanwhile the amplitude of the signal was decreased due to the angle between the hydrophone sensing surface was no longer perpendicular to the acoustic wave transmit direction. The minimum signal detection was reached when the hydrophone was 1400μm away from the starting position.



<u>Figure 68. Metalens photoacoustic signal excitation.</u> . (a) 3D model experiment setup. (b) Comparison of the metalens excited photoacoustic signals at different positions. (c) Different position, photoacoustic signal plots.

After the metalens excited photoacoustic signal characterization, a customized metalens based OR-PAM system was designed and the schematic is shown in Figure 69 (a). A 532nm short

pulse optical laser (SPOT-10-100-532, Elforlight Ltd, UK) was selected as excitation source. The free space laser beam first passes through the ND filter (NDC-25C-4M, Thorlabs, US) to adjust the laser energy. Then a 09/10 beamsplitter (BS037, Thorlabs, US) was used to split the laser beam, where the less energy beam arm was fed into the photodetector (DET10A2, Thorlabs, US) for triggering, and the majority of the laser was expanded by the lens pair Lens 1 (AC-127-025-A, Thorlabs, US) and Lens 2 (AC-254-125-A, Thorlabs, US). After that by using the fiber coupler (F-915T, Newport, US) the expanded laser beam was coupled into the SMF via Lens 3 (AC-127-030-A, Thorlabs, US). The SMF was connected with fiber port L4 (PAF-X-11-PC-A, Thorlabs, US) to collimate the beam and expanded by a fixed magnification beam expander (GBE02-A, Thorlabs, US) to fully cover the metalens effective area. A Cr coated USAF target (R3L1S4N, Thorlabs, US) was place inside the water tank at the metalens focal distance as a target. To achieve the 2D image scanning, the water tank was mounted on the voice-coil linear translation stage (V-102, PI, German). For photoacoustic signals collection, a hydrophone needle (HNC-1500, ONDA, US) was mounted on a 3D manual stage and the needle tip was placed close to the line-focused beam inside the water tank. Then, the photoacoustic signals were amplified by a preamplifier (AH-2010, ONDA, US) and fed into the high-speed digitizer (AtS9350, Alazar Tech Inc, Pointe-Claire, QC, Canada) with sampling rate of 500MS/s resolution. The data were saved to the lab computer further signal processing and image reconstruction. The computer was used to synchronize the pulse laser, scanning stage movement and data acquisition. In this Letter, we demonstrate the metalens based photoacoustic microscope system which using a line-focused excitation source with single ultrasonic sensor for collection to achieve 2D scanning. Ideally, the 2D photoacoustic signals acquisition should be collected by a single axis scanning with the ultrasonic sensor array which may significantly reduce the scanning time. However, in here, we only use single hydrophone needle to prove the principle of metalens based photoacoustic microscope imaging system.



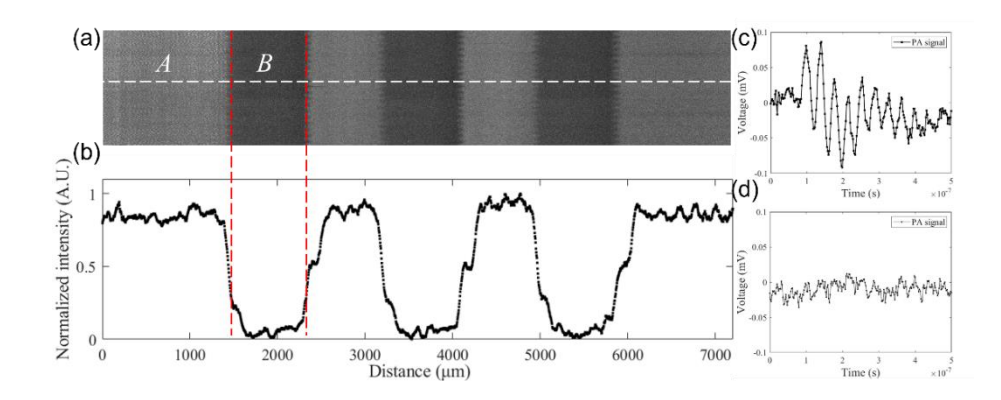
<u>Figure 69 Schematic of metalens photoacoustic microscope and system characterization.</u> (a) Schematic of the image system. BP, beamsplitter; PD, photodetector; SMF, single mode fiber; PA, preamplifier. (b) Measurement of lateral resolution at metalens focal distance. (c) Measurement of axial resolution at metalens focal distance.

As we mentioned the metalens characterization previously, the line-focused beam sized is about 10.2μm, to measure the system lateral resolution at metalens focal plane, we conducted experiment by detecting the photoacoustic signal of a sharp edge of a Cr coated USAF target. The scanning step size was 3.5 μm and a 1D scanning photoacoustic amplitude signal is shown in Figure 69 (b). The edge spread function (ESF) was fitted by MATLAB from the raw data. A line spread function was calculated by taking the spatial derivative of the ESF. The lateral resolution was determined by the FWHM of the LSF which is about 10μm. The axial resolution of the system was measured by the photoacoustic A-line signal shown in Figure 69 (c). The Hilbert curve fitting (envelop detection) was applied to the A-line signal, and then, the envelope upper curve was fitted by a Gaussian curve. Finally, the axial resolution was about 420μm by the FWHM of the fitting curve which satisfy the metalens designed Rayleigh length.

7.3 Metalens Based OR-PAM Phantom Imaging

To show the potential imaging ability of the metalens based OR-PAM over a large area, we

have set up an experiment for imaging the USAF target Group -1 element 1. The reconstructed 2D image result is shown in Figure 70 (a). The total scanning FOV is 7.2x0.9mm which achieved by the 2D voice-coil linear stage. A line intensity plot from the Figure 70 (a) (white dash line) is shown in Figure 70 (b) which demonstrate a good contrast result. In Figure 70 (c) it shows the photoacoustic signal during scanning the area A which is the Cr coated features in Figure 70 (a). And in Figure 70 (d) it shows no photoacoustic signal detected during scanning the area B which is the glass substrate in Figure 70 (a).



<u>Figure 70 USAF target image result for metalens based OR-PAM.</u> (a) The reconstructed 2D photoacoustic image. (b) The line intensity plot alng the white dash line in (a). (c) Photoacoustic signal for Cr. (d) Photoacoustic signal for glass substrate.

7.4 Metalens Based OR-PAM Conclusion

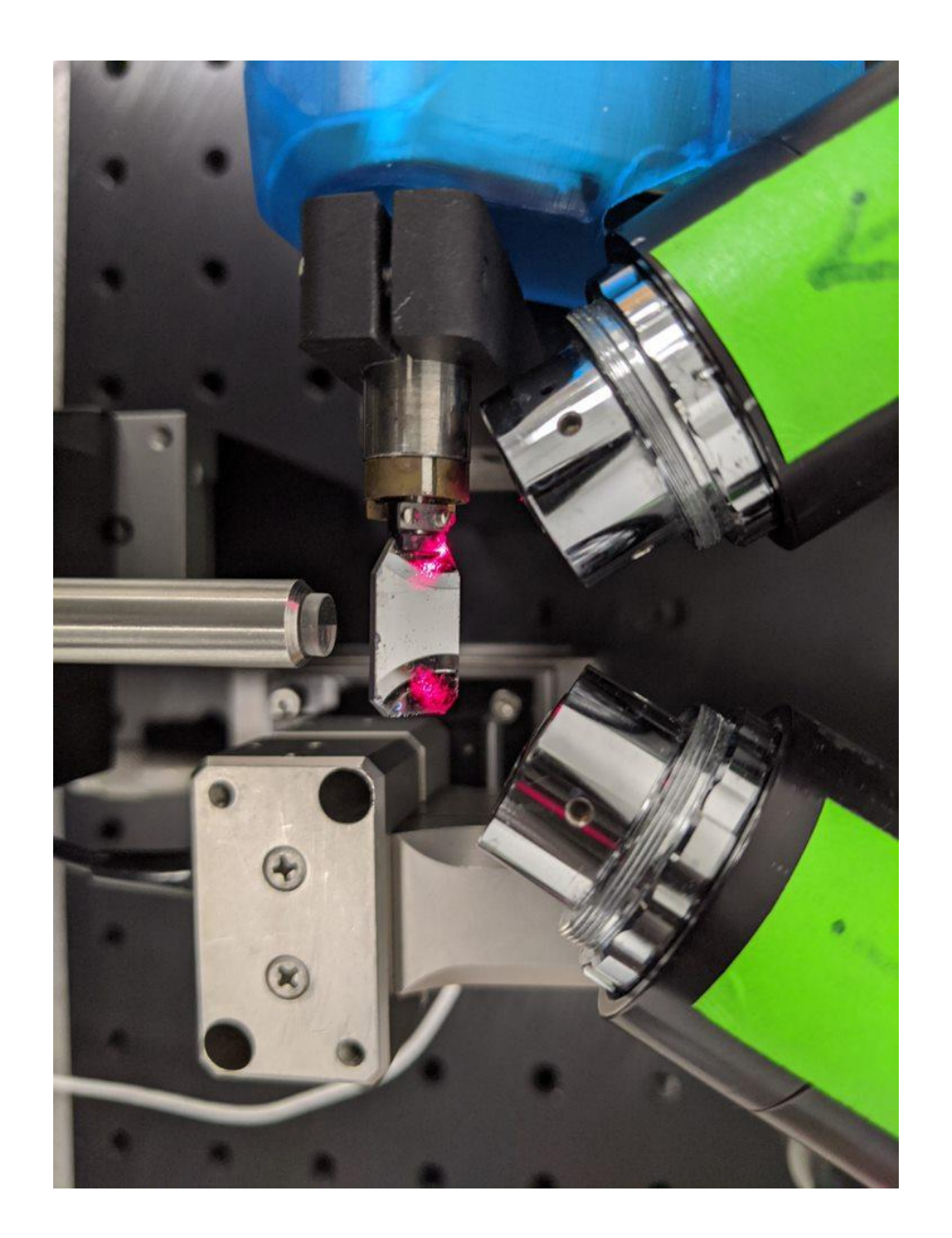
To our knowledge, this is the first time that the metalens has demonstrated a good performance in photoacoustic microscope system. This provides a great potential for miniaturized PAM probe design for future work. Also, in this chapter, we show that the application of the metalens can be extended from CW laser to short pulse laser system. The optical properties of the designed metalens have a similar behavior compares to the CW laser source and a pulse laser source. From the data acquisition side, the image scanning time could be largely reduced if the ultrasonic sensor array has been integrated into the system, so that for each 1D scanning, the 3D PA signal reconstructed images can be achieved.

CHAPTER 8: FUTURE WORK

8.1 Advanced Metalens Based Dual Axis Confocal Microscope

In this dissertation, we have demonstrated the nanofabrication metalens can achieve the light focusing effect. Due to the metalens size and fabrication process, it shows a great advantage for miniaturized imaging design.

Compared to the traditional single axis confocal, the dual axis confocal microscope not only provide the same imaging resolution but also a compact size which the excitation and collection light path are independent to each other [117, 118]. The working principle of the dual axis is simple which the excitation and collection light path are placed in a certain angle and focused on same focal point shown in Figure 71. Because the light path is designed independently, a single 2D MEMS scanner or galvo scanner can be placed before the focal point and achieve imaging scanning. Not like the single axis scanner confocal microscope which requires a scanning lens and tube lens before the objective lens, the dual axis confocal does not require any complicated optics design.



<u>Figure 71 Photo of the dual axis confocal microscope.</u> The excitation and collection light path are placed in a angle and focused on the same focal point.

By having this great advantage, here we purpose the dual axis metalens design which the 2 independent metalens will be fabricated on the same substrate and refract the beam into the same point for imaging. The schematic of the design is shown in Figure 72.

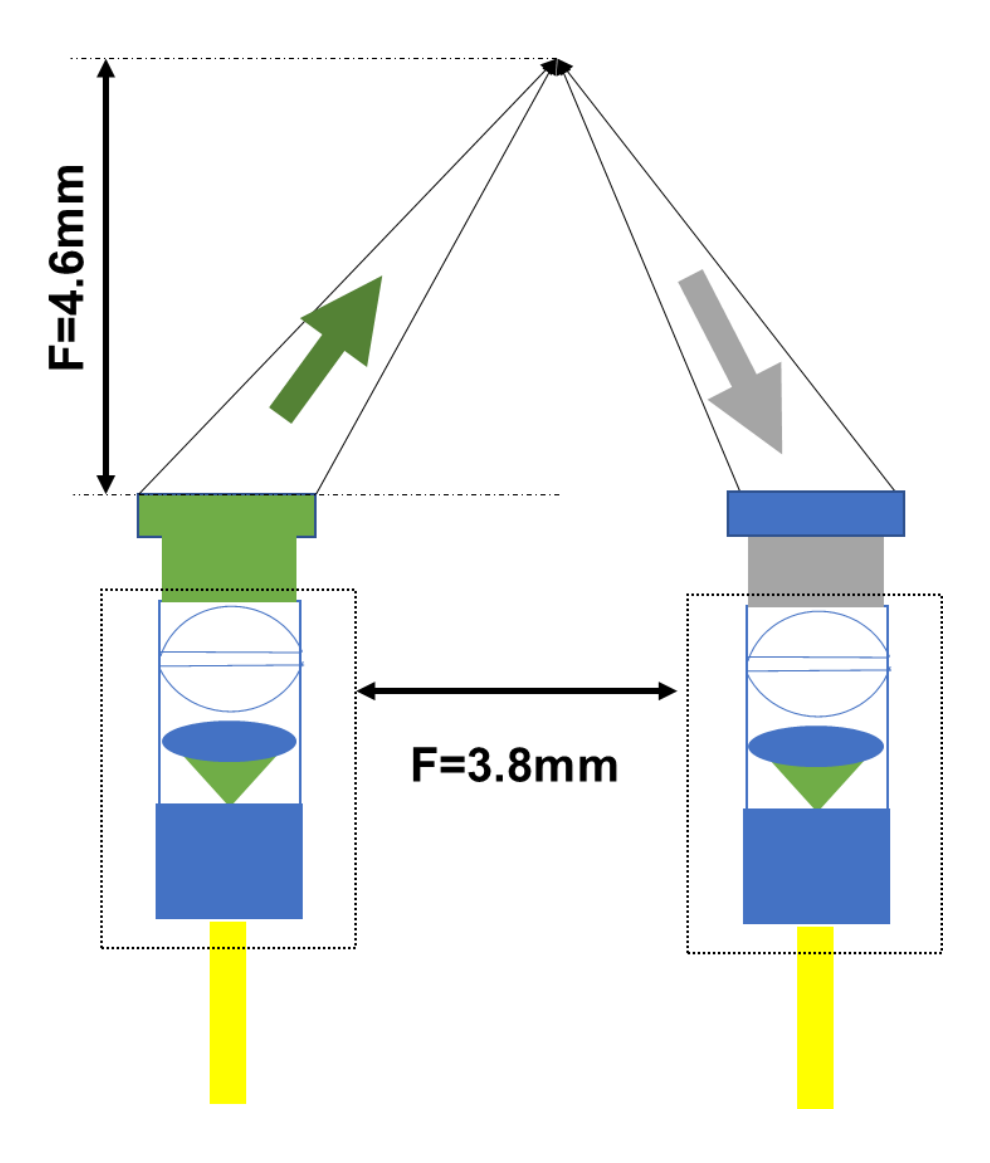
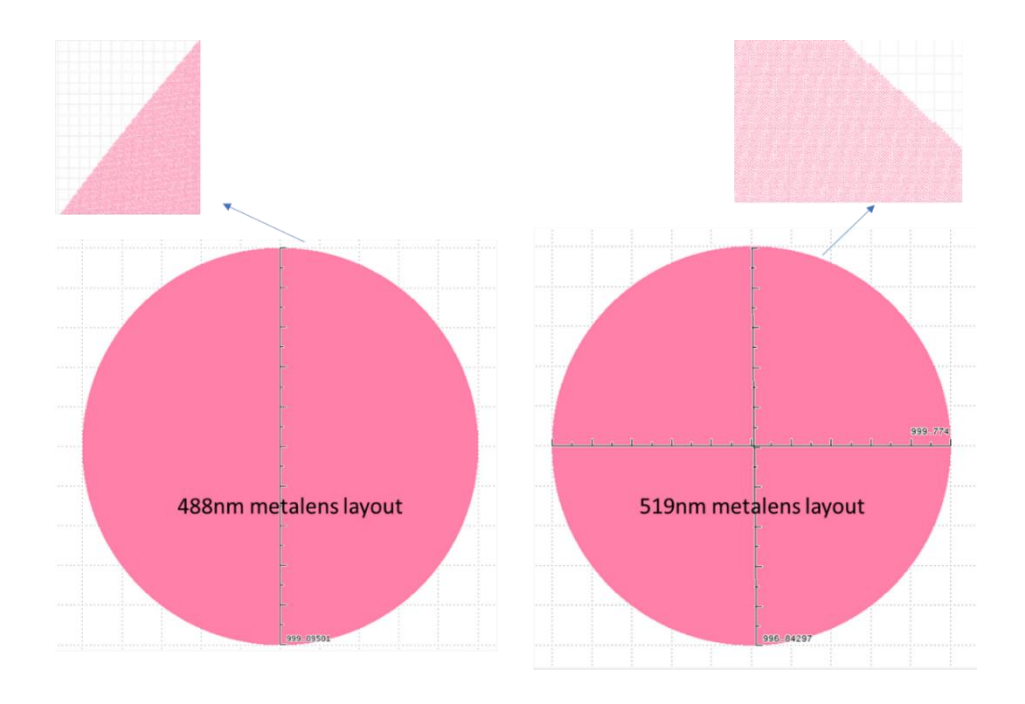


Figure 72 Dual axis metalens based confocal microscope schematic.

There are two commercial collimators placed paralleled and 3.8mm away from each other. The excitation laser beam is focused by the first metalens at its designed wavelength and the focal point is 4.6mm away from the metalens surface. For the collection side, another metalens designed at the fluorescence wavelength collimated the light and sends it back to the collimator.

The CAD drawing for the designed dual axis metalens at 488nm and 519nm working wavelengths is shown in Figure 73.



<u>Figure 73 The CAD drawing of the designed dual axis metalens.</u> On the left, the working wavelength is 488nm and on the right the working wavelength is 519nm.

8.2 MOEMS Based Multiphoton Microscope System

The multiphoton microscopy (MPM) has been widely used today for biomedical study to detect the nonlinear optical signals such as tissue imaging and cell imaging [119-121]. The MPM imaging method has been identified as the best non-invasive imaging system not only it provides a high optical resolution image but also for generates the deep tissue structure imaging. In general, the MPM is also considered as two-photon microscopy imaging which can provide two-photon excitation fluorescence (TPEF) and second harmonic generation (SHG) [121].

The traditional MPM system requires a complicated optics design which provides the best excitation beam quality and high collection efficiency (high NA objective lens). To achieve this, many designed systems have a bulky size and expensive optics components. In here, we purpose the idea for a MOEMS based miniaturized MPM handheld system.

One of the key factors of the MPM system is the fiber based femtosecond (fs) laser. In Figure 74, we are showing the designed fs laser engine at 1550nm.

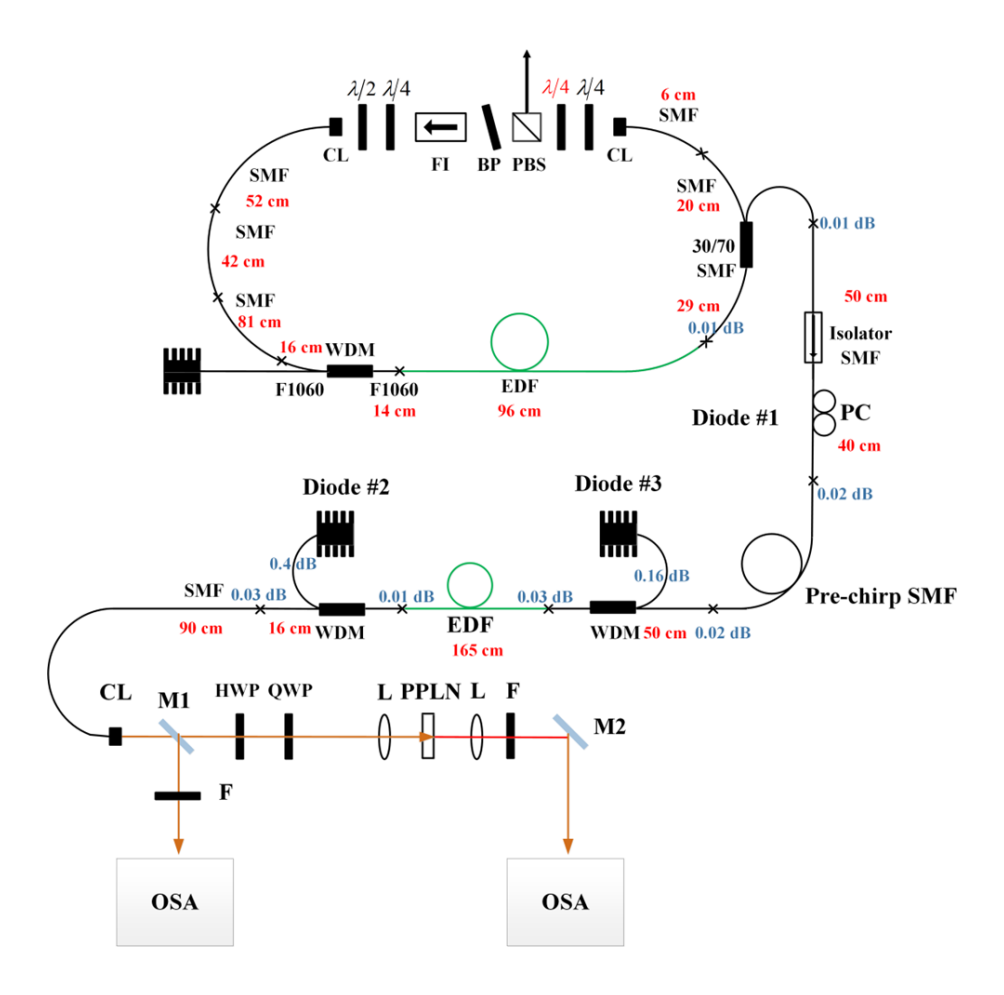


Figure 74 Femtosecond laser schematic design.

The fiber-based fs laser includes two parts, oscillator, and forward pump. For the oscillator, we use the 980nm laser diode (Thorlabs, NJ, USA) to generate the light source. To let the fs laser, have a 1550nm center wavelength output, the SMF is connected to the erbium doped fiber (EDF). The equation to calculate the output laser repetition rate is shown below:

Equation 10 Fs laser repetition rate calculation

$$Repetition \ rate = \frac{c}{nL} = \frac{3 \times 10^8}{1.5 \times L_{fiber} + 1 \times L_{air}}$$

Where the c is the speed of light, n is the refractive index and L is the free space distance. Also, to balance the fs pulse width and energy, the net dispersion range D_T needs to be calculated which relates to the length of the SMF and EDF. For the designed oscillator, the length of each fiber component is shown below:

Table 4 Net dispersion of the designed oscillator.

Fiber type	GVD at 1550nm (ps^2/m)	Length (m)
EDF	+0.057	0.96
SMF	-0.023	2.35
F1060	-0.006	0.35

The total D_T of the designed oscillator is about $+0.004\pm0.002ps^2$, and the laser threshold current is 52mA. The real setup photo is show in Figure 75.

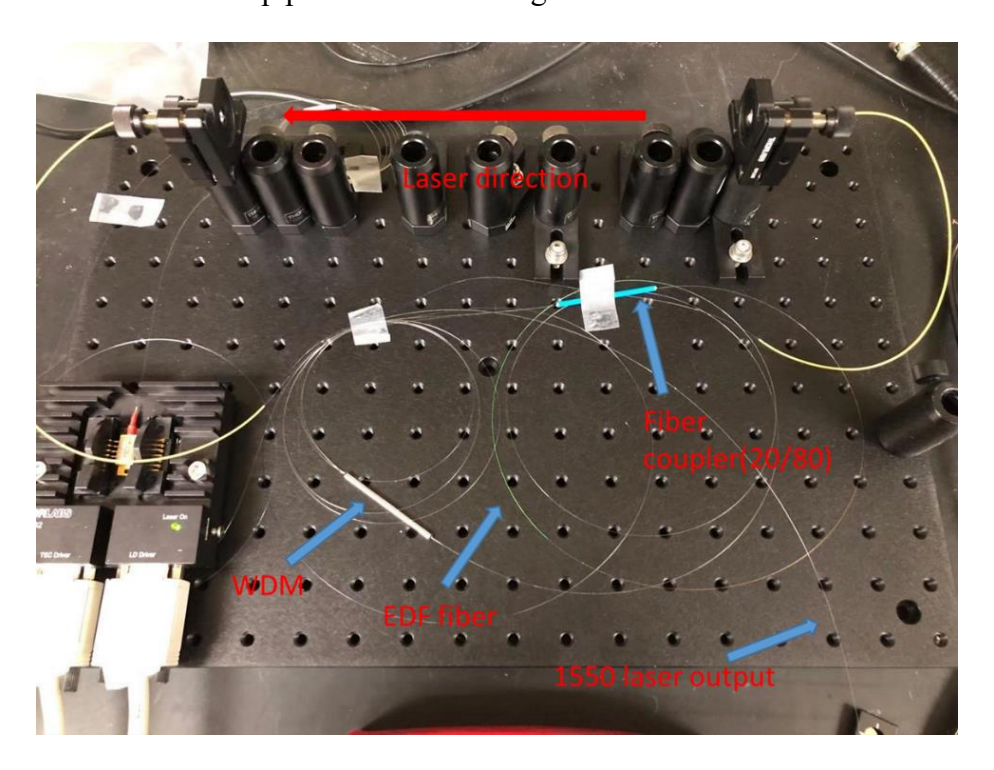


Figure 75 The photo of the 1550nm fs oscillator.

To increase the output power of the fs laser, the output of the oscillator laser beam at 1550nm wavelength needs to be amplified by two forward pumps shown is Figure 76.

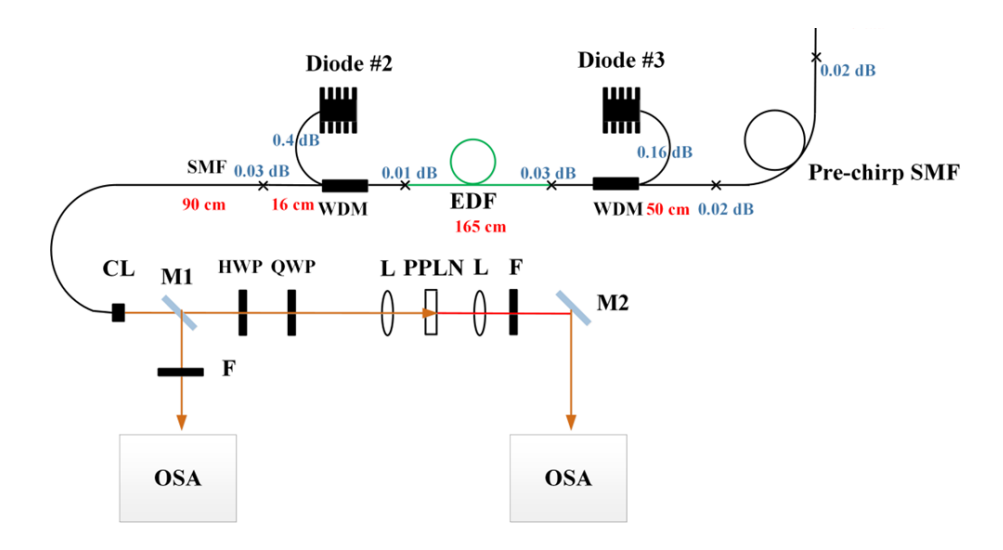


Figure 76 Amplifier forward pump for fs laser.

After the fiber-based fs laser designed, the MOEMS based MPM handheld system schematic is shown in Figure 77.

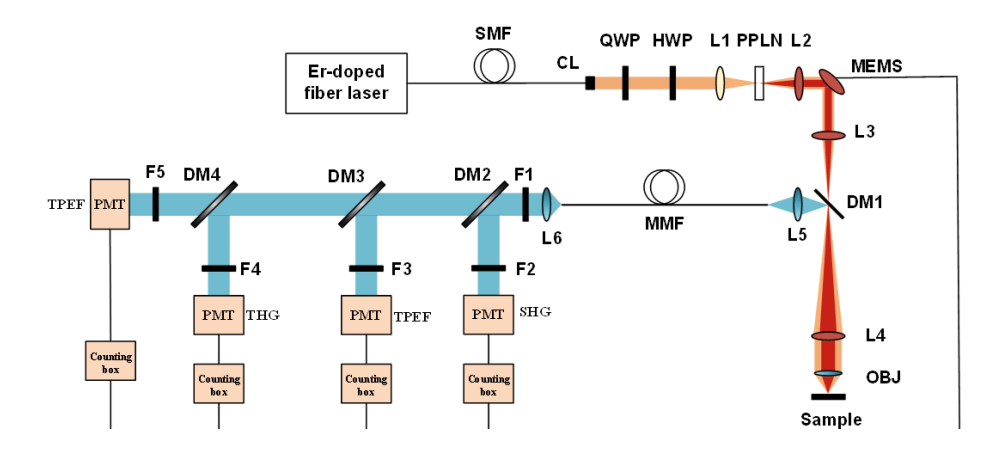


Figure 77 MOEMS based MPM handheld system schematic.

The final designed system will include a MEMS scanner to achieve 2D scanning. A dichroic mirror is place between the scan lens L3 and L4 to split excitation and emission light. There are 4 fluorescence collection channels to reconstruct different emission wavelength 2D images.

BIBLIOGRAPHY

- [1] S. Sun, Q. He, S. Xiao, Q. Xu, X. Li, and L. Zhou, "Gradient-index meta-surfaces as a bridge linking propagating waves and surface waves," *Nature materials*, vol. 11, no. 5, pp. 426-431, 2012.
- [2] N. Yu and F. Capasso, "Flat optics with designer metasurfaces," *Nature materials*, vol. 13, no. 2, pp. 139-150, 2014.
- [3] A. V. Kildishev, A. Boltasseva, and V. M. Shalaev, "Planar photonics with metasurfaces," *Science*, vol. 339, no. 6125, 2013.
- [4] S. B. Glybovski, S. A. Tretyakov, P. A. Belov, Y. S. Kivshar, and C. R. Simovski, "Metasurfaces: From microwaves to visible," *Physics reports*, vol. 634, pp. 1-72, 2016.
- [5] S. Jahani and Z. Jacob, "All-dielectric metamaterials," *Nature nanotechnology,* vol. 11, no. 1, pp. 23-36, 2016.
- [6] W. T. Chen *et al.*, "High-efficiency broadband meta-hologram with polarization-controlled dual images," *Nano letters*, vol. 14, no. 1, pp. 225-230, 2014.
- [7] M. W. Knight *et al.*, "Aluminum Plasmonic Nanoantennas," *Nano Letters*, vol. 12, no. 11, pp. 6000-6004, 2012/11/14 2012.
- [8] A. Arbabi, Y. Horie, M. Bagheri, and A. Faraon, "Dielectric metasurfaces for complete control of phase and polarization with subwavelength spatial resolution and high transmission," *Nature nanotechnology*, vol. 10, no. 11, pp. 937-943, 2015.
- [9] P. Lalanne, S. Astilean, P. Chavel, E. Cambril, and H. Launois, "Design and fabrication of blazed binary diffractive elements with sampling periods smaller than the structural cutoff," *JOSA A*, vol. 16, no. 5, pp. 1143-1156, 1999.
- [10] S. Vo *et al.*, "Sub-wavelength grating lenses with a twist," *IEEE Photonics Technology Letters*, vol. 26, no. 13, pp. 1375-1378, 2014.
- [11] S.-L. Chen, Z. Xie, T. Ling, L. J. Guo, X. Wei, and X. Wang, "Miniaturized all-optical photoacoustic microscopy based on microelectromechanical systems mirror scanning," *Optics letters*, vol. 37, no. 20, pp. 4263-4265, 2012.
- [12] N. Yu and F. Capasso, "Flat optics with designer metasurfaces," *Nature Materials*, Review Article vol. 13, p. 139, 01/23/online 2014.
- [13] A. V. Kildishev, A. Boltasseva, and V. M. Shalaev, "Planar Photonics with Metasurfaces," *Science*, vol. 339, no. 6125, p. 1232009, 2013.
- [14] S. Jahani and Z. Jacob, "All-dielectric metamaterials," *Nature Nanotechnology, Review Article vol.* 11, p. 23, 01/07/online 2016.

- [15] W. T. Chen *et al.*, "High-Efficiency Broadband Meta-Hologram with Polarization-Controlled Dual Images," *Nano Letters*, vol. 14, no. 1, pp. 225-230, 2014/01/08 2014.
- [16] A. Arbabi, Y. Horie, M. Bagheri, and A. Faraon, "Dielectric metasurfaces for complete control of phase and polarization with subwavelength spatial resolution and high transmission," *Nature Nanotechnology*, vol. 10, p. 937, 08/31/online 2015.
- [17] P. Lalanne, S. Astilean, P. Chavel, E. Cambril, and H. Launois, "Design and fabrication of blazed binary diffractive elements with sampling periods smaller than the structural cutoff," *Journal of the Optical Society of America A*, vol. 16, no. 5, pp. 1143-1156, 1999/05/01 1999.
- [18] D. J. Hare *et al.*, "The effect of paraformaldehyde fixation and sucrose cryoprotection on metal concentration in murine neurological tissue," *Journal of Analytical Atomic Spectrometry*, vol. 29, no. 3, pp. 565-570, 2014.
- [19] M. Khorasaninejad and F. Capasso, "Metalenses: Versatile multifunctional photonic components," *Science*, vol. 358, no. 6367, p. eaam8100, 2017.
- [20] L. Novotny and N. van Hulst, "Antennas for light," *Nature Photonics*, Review Article vol. 5, p. 83, 02/01/online 2011.
- [21] L. Yin *et al.*, "Subwavelength Focusing and Guiding of Surface Plasmons," *Nano Letters*, vol. 5, no. 7, pp. 1399-1402, 2005/07/01 2005.
- [22] Z. Liu, J. M. Steele, W. Srituravanich, Y. Pikus, C. Sun, and X. Zhang, "Focusing Surface Plasmons with a Plasmonic Lens," *Nano Letters*, vol. 5, no. 9, pp. 1726-1729, 2005/09/01 2005.
- [23] A. Arbabi, Y. Horie, A. J. Ball, M. Bagheri, and A. Faraon, "Subwavelength-thick lenses with high numerical apertures and large efficiency based on high-contrast transmitarrays," *Nature Communications*, Article vol. 6, p. 7069, 05/07/online 2015.
- [24] M. Khorasaninejad *et al.*, "Polarization-Insensitive Metalenses at Visible Wavelengths," *Nano Letters*, vol. 16, no. 11, pp. 7229-7234, 2016/11/09 2016.
- [25] C. Lianwei, Z. Yan, W. Mengxue, and H. Minghui, "Remote-mode microsphere nanoimaging: new boundaries for optical microscopes," *Opto-Electronic Advances*, vol. 1, no. 1, p. 170001, 2018/01/25 2018.
- [26] Q. Feng, M. Pu, C. Hu, and X. Luo, "Engineering the dispersion of metamaterial surface for broadband infrared absorption," *Optics Letters*, vol. 37, no. 11, pp. 2133-2135, 2012/06/01 2012.
- [27] M. Pu *et al.*, "Design principles for infrared wide-angle perfect absorber based on plasmonic structure," *Optics Express*, vol. 19, no. 18, pp. 17413-17420, 2011/08/29 2011.
- [28] X. Li et al., "Multicolor 3D meta-holography by broadband plasmonic modulation,"

- Science Advances, vol. 2, no. 11, p. e1601102, 2016.
- [29] Z.-L. Deng, S. Zhang, and G. P. Wang, "A facile grating approach towards broadband, wide-angle and high-efficiency holographic metasurfaces," *Nanoscale*, 10.1039/C5NR07181J vol. 8, no. 3, pp. 1588-1594, 2016.
- [30] Z.-L. Deng and G. Li, "Metasurface optical holography," *Materials Today Physics*, vol. 3, pp. 16-32, 2017/12/01/ 2017.
- [31] X. Zhang *et al.*, "Ultrahigh-capacity dynamic holographic displays via anisotropic nanoholes," *Nanoscale*, 10.1039/C6NR07854K vol. 9, no. 4, pp. 1409-1415, 2017.
- [32] A. Arbabi, E. Arbabi, S. M. Kamali, Y. Horie, S. Han, and A. Faraon, "Miniature optical planar camera based on a wide-angle metasurface doublet corrected for monochromatic aberrations," *Nature Communications*, Article vol. 7, p. 13682, 11/28/online 2016.
- [33] B. Groever, W. T. Chen, and F. Capasso, "Meta-Lens Doublet in the Visible Region," *Nano Letters*, vol. 17, no. 8, pp. 4902-4907, 2017/08/09 2017.
- [34] R. Kingslake, *A history of the photographic lens*. Boston: Academic Press, 1989, pp. xi, 334 p.
- [35] M. Jang *et al.*, "Wavefront shaping with disorder-engineered metasurfaces," *Nature Photonics*, vol. 12, no. 2, pp. 84-90, 2018/02/01 2018.
- [36] Y. Guo, X. Ma, M. Pu, X. Li, Z. Zhao, and X. Luo, "High-Efficiency and Wide-Angle Beam Steering Based on Catenary Optical Fields in Ultrathin Metalens," *Advanced Optical Materials*, vol. 6, no. 19, p. 1800592, 2018/10/01 2018.
- [37] J. Xu, M. Cua, E. H. Zhou, Y. Horie, A. Faraon, and C. Yang, "Wide-angular-range and high-resolution beam steering by a metasurface-coupled phased array," *Optics Letters*, vol. 43, no. 21, pp. 5255-5258, 2018/11/01 2018.
- [38] W. D. Eldred, C. Zucker, H. J. Karten, and S. Yazulla, "Comparison of fixation and penetration enhancement techniques for use in ultrastructural immunocytochemistry," *Journal of Histochemistry & Cytochemistry*, vol. 31, no. 2, pp. 285-292, 1983.
- [39] I. W. McLean and P. K. NAKANE, "Periodate-lysine-paraformaldehyde fixative a new fixative for immunoelectron microscopy," *Journal of Histochemistry & Cytochemistry*, vol. 22, no. 12, pp. 1077-1083, 1974.
- [40] Y. Matsuda *et al.*, "Comparison of fixation methods for preservation of morphology, RNAs, and proteins from paraffin-embedded human cancer cell-implanted mouse models," *Journal of Histochemistry & Cytochemistry*, vol. 59, no. 1, pp. 68-75, 2011.
- [41] R. D. Cardiff, C. H. Miller, and R. J. Munn, "Manual hematoxylin and eosin staining of mouse tissue sections," *Cold Spring Harbor Protocols*, vol. 2014, no. 6, p. pdb. prot073411, 2014.

- [42] J. P. Hinton *et al.*, "A method to reuse archived H&E stained histology slides for a multiplex protein biomarker analysis," *Methods and Protocols*, vol. 2, no. 4, p. 86, 2019.
- [43] D. Tellez *et al.*, "Whole-slide mitosis detection in H&E breast histology using PHH3 as a reference to train distilled stain-invariant convolutional networks," *IEEE transactions on medical imaging*, vol. 37, no. 9, pp. 2126-2136, 2018.
- [44] D. Coling and B. Kachar, "Theory and application of fluorescence microscopy," *Current Protocols in Neuroscience*, no. 1, pp. 2.1. 1-2.1. 11, 1997.
- [45] T. Houseal, C. Bustamante, R. Stump, and M. Maestre, "Real-time imaging of single DNA molecules with fluorescence microscopy," *Biophysical journal*, vol. 56, no. 3, pp. 507-516, 1989.
- [46] J. Cao *et al.*, "Recent progress in NIR-II contrast agent for biological imaging," *Frontiers in bioengineering and biotechnology*, vol. 7, p. 487, 2020.
- [47] H. Zhou *et al.*, "Upconversion NIR-II fluorophores for mitochondria-targeted cancer imaging and photothermal therapy," *Nature communications*, vol. 11, no. 1, pp. 1-14, 2020.
- [48] G. Hong *et al.*, "Multifunctional in vivo vascular imaging using near-infrared II fluorescence," *Nature medicine*, vol. 18, no. 12, pp. 1841-1846, 2012.
- [49] G. Hong *et al.*, "Through-skull fluorescence imaging of the brain in a new near-infrared window," *Nature photonics*, vol. 8, no. 9, pp. 723-730, 2014.
- [50] S. Zhu *et al.*, "3D NIR-II molecular imaging distinguishes targeted organs with high-performance NIR-II bioconjugates," *Advanced Materials*, vol. 30, no. 13, p. 1705799, 2018.
- [51] S. Zhu, R. Tian, A. L. Antaris, X. Chen, and H. Dai, "Near-infrared-II molecular dyes for cancer imaging and surgery," *Advanced Materials*, vol. 31, no. 24, p. 1900321, 2019.
- [52] J. V. Frangioni, "In vivo near-infrared fluorescence imaging," *Current opinion in chemical biology*, vol. 7, no. 5, pp. 626-634, 2003.
- [53] M. Friebel, J. Helfmann, U. J. Netz, and M. C. Meinke, "Influence of oxygen saturation on the optical scattering properties of human red blood cells in the spectral range 250 to 2000 nm," *Journal of biomedical optics*, vol. 14, no. 3, p. 034001, 2009.
- [54] K. Welsher *et al.*, "A route to brightly fluorescent carbon nanotubes for near-infrared imaging in mice," *Nature nanotechnology*, vol. 4, no. 11, pp. 773-780, 2009.
- [55] D. Naczynski *et al.*, "Rare-earth-doped biological composites as in vivo shortwave infrared reporters," *Nature communications*, vol. 4, no. 1, pp. 1-10, 2013.
- [56] Z. Starosolski, R. Bhavane, K. B. Ghaghada, S. A. Vasudevan, A. Kaay, and A. Annapragada, "Indocyanine green fluorescence in second near-infrared (NIR-II) window," *Plos one*, vol. 12, no. 11, p. e0187563, 2017.

- [57] S. Zhu, B. C. Yung, S. Chandra, G. Niu, A. L. Antaris, and X. Chen, "Near-infrared-II (NIR-II) bioimaging via off-peak NIR-I fluorescence emission," *Theranostics*, vol. 8, no. 15, p. 4141, 2018.
- [58] H. Wan *et al.*, "A bright organic NIR-II nanofluorophore for three-dimensional imaging into biological tissues," *Nature communications*, vol. 9, no. 1, pp. 1-9, 2018.
- [59] J. Cao *et al.*, "Recent progress in NIR-II contrast agent for biological imaging," *Frontiers in bioengineering and biotechnology*, p. 487, 2020.
- [60] B. Zhu, S. Kwon, J. C. Rasmussen, M. Litorja, and E. M. Sevick-Muraca, "Comparison of NIR versus SWIR fluorescence image device performance using working standards calibrated with SI units," *IEEE Transactions on Medical Imaging*, vol. 39, no. 4, pp. 944-951, 2019.
- [61] J. A. Carr *et al.*, "Shortwave infrared fluorescence imaging with the clinically approved near-infrared dye indocyanine green," *Proceedings of the National Academy of Sciences*, vol. 115, no. 17, pp. 4465-4470, 2018.
- [62] R. K. Jain, "Antiangiogenesis strategies revisited: from starving tumors to alleviating hypoxia," *Cancer cell*, vol. 26, no. 5, pp. 605-622, 2014.
- [63] T.-L. Liu *et al.*, "Observing the cell in its native state: Imaging subcellular dynamics in multicellular organisms," *Science*, vol. 360, no. 6386, p. eaaq1392, 2018.
- [64] A. T. Wassie, Y. Zhao, and E. S. Boyden, "Expansion microscopy: principles and uses in biological research," *Nature methods*, vol. 16, no. 1, pp. 33-41, 2019.
- [65] L. Mascheroni, K. M. Scherer, J. D. Manton, E. Ward, O. Dibben, and C. F. Kaminski, "Combining sample expansion and light sheet microscopy for the volumetric imaging of virus-infected cells with super-resolution," *Biomedical Optics Express*, vol. 11, no. 9, pp. 5032-5044, 2020.
- [66] J. Huisken, J. Swoger, F. Del Bene, J. Wittbrodt, and E. H. Stelzer, "Optical sectioning deep inside live embryos by selective plane illumination microscopy," *Science*, vol. 305, no. 5686, pp. 1007-1009, 2004.
- [67] H.-U. Dodt *et al.*, "Ultramicroscopy: three-dimensional visualization of neuronal networks in the whole mouse brain," *Nature methods*, vol. 4, no. 4, pp. 331-336, 2007.
- [68] K. Chung *et al.*, "Structural and molecular interrogation of intact biological systems," *Nature*, vol. 497, no. 7449, pp. 332-337, 2013.
- [69] A. K. Glaser *et al.*, "Light-sheet microscopy for slide-free non-destructive pathology of large clinical specimens," *Nature biomedical engineering*, vol. 1, no. 7, pp. 1-10, 2017.
- [70] A. K. Glaser *et al.*, "Multi-immersion open-top light-sheet microscope for high-throughput imaging of cleared tissues," *Nature communications*, vol. 10, no. 1, pp. 1-8, 2019.

- [71] A. Bashkatov, E. Genina, V. Kochubey, and V. Tuchin, "Optical properties of human skin, subcutaneous and mucous tissues in the wavelength range from 400 to 2000 nm," *Journal of Physics D: Applied Physics*, vol. 38, no. 15, p. 2543, 2005.
- [72] K. Welsher, S. P. Sherlock, and H. Dai, "Deep-tissue anatomical imaging of mice using carbon nanotube fluorophores in the second near-infrared window," *Proceedings of the National Academy of Sciences*, vol. 108, no. 22, pp. 8943-8948, 2011.
- [73] O. T. Bruns *et al.*, "Next-generation in vivo optical imaging with short-wave infrared quantum dots," *Nature biomedical engineering*, vol. 1, no. 4, pp. 1-11, 2017.
- [74] M. Zhang *et al.*, "Bright quantum dots emitting at~ 1,600 nm in the NIR-IIb window for deep tissue fluorescence imaging," *Proceedings of the National Academy of Sciences*, vol. 115, no. 26, pp. 6590-6595, 2018.
- [75] F. Wang *et al.*, "Light-sheet microscopy in the near-infrared II window," *Nature methods*, vol. 16, no. 6, pp. 545-552, 2019.
- [76] M. Minsky, "Microscopy apparatus US patent 3013467," USP Office, Ed. US, vol. 658, 1961.
- [77] M. Minsky, "Memoir on inventing the confocal scanning microscope," *Scanning*, vol. 10, no. 4, pp. 128-138, 1988.
- [78] W. Amos and J. White, "How the confocal laser scanning microscope entered biological research," *Biology of the Cell*, vol. 95, no. 6, pp. 335-342, 2003.
- [79] D. Hamilton and T. Wilson, "Scanning optical microscopy by objective lens scanning," *Journal of Physics E: Scientific Instruments*, vol. 19, no. 1, p. 52, 1986.
- [80] M. H. El-Dakdouki *et al.*, "Development of multifunctional hyaluronan-coated nanoparticles for imaging and drug delivery to cancer cells," *Biomacromolecules*, vol. 13, no. 4, pp. 1144-1151, 2012.
- [81] M. Tani, M. Akamatsu, Y. Yasuda, and H. Toshiyoshi, "A two-axis piezoelectric tilting micromirror with a newly developed PZT-meandering actuator," in 2007 IEEE 20th International Conference on Micro Electro Mechanical Systems (MEMS), 2007, pp. 699-702: IEEE.
- [82] M. Tani, M. Akamatsu, Y. Yasuda, H. Fujita, and H. Toshiyoshi, "A 2D-optical scanner actuated by PZT film deposited by arc discharged reactive ion-plating (ADRIP) method," in *Proc. IEEE-LEOS Conf. Optical MEMS 2004*, 2004, pp. 188-189.
- [83] M. Tani, M. Akamatsu, Y. Yasuda, H. Fujita, and H. Toshiyoshi, "A combination of fast resonant mode and slow static deflection of SOI-PZT actuators for MEMS image projection display," in *IEEE/LEOS International Conference on Optical MEMS and Their Applications Conference*, 2006., 2006, pp. 25-26: IEEE.

- [84] H. Hertz, "Ueber einen Einfluss des ultravioletten Lichtes auf die electrische Entladung," *Annalen der Physik*, vol. 267, no. 8, pp. 983-1000, 1887.
- [85] H. Iams and B. Salzberg, "The secondary emission phototube," *Proceedings of the Institute of Radio Engineers*, vol. 23, no. 1, pp. 55-64, 1935.
- [86] R. H. Hadfield and G. Johansson, *Superconducting devices in quantum optics*. Springer, 2016.
- [87] H.-S. Zhong *et al.*, "Quantum computational advantage using photons," *Science*, vol. 370, no. 6523, pp. 1460-1463, 2020.
- [88] J. O'Brien, "Silicon Photonic Quantum Computing," in *APS March Meeting Abstracts*, 2018, vol. 2018, p. B05. 005.
- [89] R. H. Hadfield *et al.*, "Single photon source characterization with a superconducting single photon detector," *Optics Express*, vol. 13, no. 26, pp. 10846-10853, 2005.
- [90] G. Reithmaier *et al.*, "On-chip generation, routing and detection of quantum light," *arXiv* preprint arXiv:1408.2275, 2014.
- [91] J. W. Silverstone *et al.*, "On-chip quantum interference between silicon photon-pair sources," *Nature Photonics*, vol. 8, no. 2, pp. 104-108, 2014.
- [92] A. McCarthy *et al.*, "Kilometer-range, high resolution depth imaging via 1560 nm wavelength single-photon detection," *Optics express*, vol. 21, no. 7, pp. 8904-8915, 2013.
- [93] G. G. Taylor *et al.*, "Photon counting LIDAR at 2.3 µm wavelength with superconducting nanowires," *Optics express*, vol. 27, no. 26, pp. 38147-38158, 2019.
- [94] A. Kadin and M. Johnson, "Nonequilibrium photon-induced hotspot: A new mechanism for photodetection in ultrathin metallic films," *Applied Physics Letters*, vol. 69, no. 25, pp. 3938-3940, 1996.
- [95] G. Gol'Tsman *et al.*, "Picosecond superconducting single-photon optical detector," *Applied physics letters*, vol. 79, no. 6, pp. 705-707, 2001.
- [96] C. M. Natarajan, M. G. Tanner, and R. H. Hadfield, "Superconducting nanowire single-photon detectors: physics and applications," *Superconductor science and technology*, vol. 25, no. 6, p. 063001, 2012.
- [97] A. D. Semenov, G. N. Gol'tsman, and A. A. Korneev, "Quantum detection by current carrying superconducting film," *Physica C: Superconductivity*, vol. 351, no. 4, pp. 349-356, 2001.
- [98] J. K. Yang, A. J. Kerman, E. A. Dauler, V. Anant, K. M. Rosfjord, and K. K. Berggren, "Modeling the electrical and thermal response of superconducting nanowire single-photon detectors," *IEEE transactions on applied superconductivity,* vol. 17, no. 2, pp. 581-585,

2007.

- [99] R. Devi, V. Bansal, and D. Kumar, "Design and Simulation of Electrothermally Activated Bidirectional Microtweezer Using PMMA for Biomedical Applications."
- [100] R. Hadfield, A. J. Miller, S. W. Nam, R. L. Kautz, and R. E. Schwall, "Low-frequency phase locking in high-inductance superconducting nanowires," *Applied Physics Letters*, vol. 87, no. 20, p. 203505, 2005.
- [101] A. J. Kerman *et al.*, "Kinetic-inductance-limited reset time of superconducting nanowire photon counters," *Applied physics letters*, vol. 88, no. 11, p. 111116, 2006.
- [102] D. L. Rosene, N. J. Roy, and B. J. Davis, "A cryoprotection method that facilitates cutting frozen sections of whole monkey brains for histological and histochemical processing without freezing artifact," *Journal of Histochemistry & Cytochemistry*, vol. 34, no. 10, pp. 1301-1315, 1986.
- [103] R. Gibb and B. Kolb, "A method for vibratome sectioning of Golgi–Cox stained whole rat brain," *Journal of neuroscience methods*, vol. 79, no. 1, pp. 1-4, 1998.
- [104] Y. Wang *et al.*, "Fiber-laser-based photoacoustic microscopy and melanoma cell detection," *Journal of biomedical optics*, vol. 16, no. 1, p. 011014, 2011.
- [105] S. Hu and L. V. Wang, "Neurovascular photoacoustic tomography," *Frontiers in neuroenergetics*, p. 10, 2010.
- [106] Y. Zhou, W. Xing, K. I. Maslov, L. A. Cornelius, and L. V. Wang, "Handheld photoacoustic microscopy to detect melanoma depth in vivo," *Optics letters*, vol. 39, no. 16, pp. 4731-4734, 2014.
- [107] C. Zhang, L. V. Wang, Y.-J. Cheng, J. Chen, and S. A. Wickline, "Label-free photoacoustic microscopy of myocardial sheet architecture," *Journal of biomedical optics*, vol. 17, no. 6, p. 060506, 2012.
- [108] M. Fernández-Suárez and A. Y. Ting, "Fluorescent probes for super-resolution imaging in living cells," *Nature reviews Molecular cell biology*, vol. 9, no. 12, pp. 929-943, 2008.
- [109] H. Li, B. Dong, Z. Zhang, H. F. Zhang, and C. Sun, "A transparent broadband ultrasonic detector based on an optical micro-ring resonator for photoacoustic microscopy," *Scientific reports*, vol. 4, no. 1, pp. 1-8, 2014.
- [110] S.-L. Chen, L. J. Guo, and X. Wang, "All-optical photoacoustic microscopy," *Photoacoustics*, vol. 3, no. 4, pp. 143-150, 2015.
- [111] T. Ling, S.-L. Chen, and L. J. Guo, "Fabrication and characterization of high Q polymer micro-ring resonator and its application as a sensitive ultrasonic detector," *Optics express*, vol. 19, no. 2, pp. 861-869, 2011.

- [112] T. Ling, S.-L. Chen, and L. J. Guo, "High-sensitivity and wide-directivity ultrasound detection using high Q polymer microring resonators," *Applied Physics Letters*, vol. 98, no. 20, p. 204103, 2011.
- [113] H. Li *et al.*, "Disposable ultrasound-sensing chronic cranial window by soft nanoimprinting lithography," *Nature communications*, vol. 10, no. 1, pp. 1-9, 2019.
- [114] E. Betzig *et al.*, "Imaging intracellular fluorescent proteins at nanometer resolution," *science*, vol. 313, no. 5793, pp. 1642-1645, 2006.
- [115] M. G. Gustafsson, "Nonlinear structured-illumination microscopy: wide-field fluorescence imaging with theoretically unlimited resolution," *Proceedings of the National Academy of Sciences*, vol. 102, no. 37, pp. 13081-13086, 2005.
- [116] H. F. Zhang, K. Maslov, G. Stoica, and L. V. Wang, "Functional photoacoustic microscopy for high-resolution and noninvasive in vivo imaging," *Nature biotechnology*, vol. 24, no. 7, pp. 848-851, 2006.
- [117] T. D. Wang, M. J. Mandella, C. H. Contag, and G. S. Kino, "Dual-axis confocal microscope for high-resolution in vivo imaging," *Optics letters*, vol. 28, no. 6, pp. 414-416, 2003.
- [118] L. Wei, C. Yin, and J. T. Liu, "Dual-axis confocal microscopy for point-of-care pathology," *IEEE Journal of Selected Topics in Quantum Electronics*, vol. 25, no. 1, pp. 1-10, 2018.
- [119] W. Denk, J. H. Strickler, and W. W. Webb, "Two-photon laser scanning fluorescence microscopy," *Science*, vol. 248, no. 4951, pp. 73-76, 1990.
- [120] P. J. Campagnola, A. Lewis, and L. M. Loew, "High-resolution nonlinear optical imaging of live cells by second harmonic generation," *Biophysical journal*, vol. 77, no. 6, pp. 3341-3349, 1999.
- [121] W. R. Zipfel, R. M. Williams, and W. W. Webb, "Nonlinear magic: multiphoton microscopy in the biosciences," *Nature biotechnology*, vol. 21, no. 11, pp. 1369-1377, 2003.